WAVEGUIDING OF ELECTROMAGNETIC WAVES AND INVESTIGATION OF NEGATIVE PHASE VELOCITY IN PHOTONIC CRYSTALS AND METAMATERIALS

A THESIS
SUBMITTED TO THE DEPARTMENT OF ELECTRICAL AND ELECTRONICS ENGINEERING
AND THE GRADUATE SCHOOL OF ENGINEERING AND SCIENCE
OF BILKENT UNIVERSITY
IN PARTIAL FULLFILMENT OF THE REQUIREMENTS
FOR THE DEGREE OF
DOCTOR OF PHILOSOPHY

By
İlyas Evrim Çolak
August 2012

I certify that I have read this thesis and that in my opinion it is fully adequate, in scope and in quality, as a thesis for the degree of Doctor of Philosophy.

Prof. Dr. Ekmel Özbay (Supervisor)

I certify that I have read this thesis and that in my opinion it is fully adequate, in scope and in quality, as a thesis for the degree of Doctor of Philosophy.

Prof. Dr. Orhan Aytür

I certify that I have read this thesis and that in my opinion it is fully adequate, in scope and in quality, as a thesis for the degree of Doctor of Philosophy.

Assoc. Prof. Dr. Ceyhun Bulutay

I certify that I have read this thesis and that in my opinion it is fully adequate, in scope and in quality, as a thesis for the degree of Doctor of Philosophy.

Assoc. Prof. Dr. Vakur B. Ertürk

I certify that I have read this thesis and that in my opinion it is fully adequate, in scope and in quality, as a thesis for the degree of Doctor of Philosophy.

Assoc. Prof. Dr. Hamza Kurt

Approved for the Graduate School of Engineering and Science:

Prof. Dr. Levent Onural

Director of Graduate School of Engineering and Science

ABSTRACT

WAVEGUIDING OF ELECTROMAGNETIC WAVES AND INVESTIGATION OF NEGATIVE PHASE VELOCITY IN PHOTONIC CRYSTALS AND METAMATERIALS

İlyas Evrim Çolak
Ph.D. in Electrical and Electronics Engineering
Supervisor: Prof. Dr. Ekmel Özbay

August 2012

Electromagnetic wave propagation is characterized in periodic dielectric and metallic structures: Photonic Crystals (PCs) and Metamaterials, respectively. The applications of these structures are demonstrated in the Microwave regime. In the first application, Graded Index (GRIN) PC is used to focus the incoming waves into a small spot. Speaking in terms of PC period *a*, for an incident beam with Full Width Half Maximum of 9.20*a* the power of the focusing behavior is quantified by looking at the spot size conversion ratio, which is around 3.9. PCs can act as an efficient input coupler for the PC Waveguide (PCW). The GRIN PC has been experimentally shown to yield a coupling efficiency of 5 *dB* over the single PCW at 18 GHz. This method can be applied to provide a solution for the input coupling losses between PC structures and other lightwave circuits. PCs can also be used to achieve dual-bandpass and bandstop spatial filtering by proper adjustments of the lattice parameters and the frequency range. For the plane-wave excitation, a wideband spatial filtering is shown to exist due to the specific Fabry-Perot type resonances, which are nearly independent on the angle of incidence. The effect of the finite angular

distribution of the Gaussian-beam excitation is also demonstrated. The spatial filtering in the incidence and observation angle domains has been discussed both numerically and experimentally for the non-plane-wave excitations under the light of calculated iso-frequency contours. In addition to bandstop characteristics, the dispersion relation of the PCs can be modified with the proper arrangement, namely by employment of the dimer layer. This surface layer supports the surface waves and serves like a waveguide for the electromagnetic waves. At higher frequencies above the lightline, surface waves radiate into air in the form of backward leaky waves and frequency dependent steering is reported from 0° to 70° for the outgoing beam. The leaky wave behavior and backward radiation is similar to that is seen in Left-Handed (LH) Metamaterials. Metallic fishnet layers are used to demonstrate negative refractive index (NRI) in conjunction with the left-handed behavior in this class of metamaterial. A wedge structure formed by fishnet layers is used to measure the NRI which was also verified by the retrieval analysis. The limits of homogenization are discussed. The dependence of the LH properties on the fishnet parameters is investigated parametrically. For example, the NRI changes from -1.8 to -1.3 as the interseperation distance of the layers varies from a_s=λ/10.5 (2mm) to a_s=λ/4.2 (4mm) at magnetic resonance frequency around 14.3 GHz (ω_m). It is also shown that the fishnet layers behave as an LC resonator as well as a TEM waveguide and a 1D transmission line at ω_m.

Keywords: Photonic Crystals (PCs), Graded Index PCs, Focusing, Waveguides, Spatial Filtering, Backward Leaky Waves, Metamaterials, Negative Refractive Index.

ÖZET

ELEKTROMANYETİK DALGALARIN KILAVUZLANMASI VE FOTONİK KRİSTALLER VE METAMALZEMELERDE EKSİ DEĞERLİ FAZ HIZININ İNCELENMESİ

İlyas Evrim Çolak
Elektrik ve Elektronik Mühendisliği Bölümü Doktora
Tez Yöneticisi: Prof. Dr. Ekmel Özbay
Ağustos, 2012

Dielektrik ve metalik yapılar olan Fotonik Kristaller (FK) ve Metamalzemelerde elektromanyetik dalgaların yayılımı incelenmiştir. Mikrodalga frekanslarında bu yapıların uygulamaları gösterilmiştir. Bahsedilecek çalışmaların ilkinde, Dereceli kırınım indisine (Dİ) sahip FK'in gelen dalgaların tek bir noktaya odaklanmasında kullanılabileceği gösterilmiştir. FK periyodu a olmak üzere, Rezonans Genişliği (Full Width Half Maximum, FWHM) $9.2a$ olacak şekilde gelen dalga için Dİ FK'in sağladığı nokta büyüklüğü çevirim oranı 3.9 olarak ölçülmüştür. Dİ FK yapısının yine FK dalgakılavuzları için olarak verimli bir giriş eşleyicisi olarak iş göreceği görülmüştür. Dİ FK'in, dalgakılavuzunun 18GHz'deki eşleşme verimliliğini $5dB$'nin üzerinde arttırdığı deneysel olarak gözlemlenmiştir. Bu yöntem, ışığı ileten devrelerle FK arasında giriş eşlemesinde yaşanan kayıpları azaltmaya yarayabilir. FK, frekans ve örgü değişkenlerinin uygun şekilde ayarlanmasıyla ikili kuşak geçirgen ya da kuşak durduran uzamsal süzgeç olarak da kullanılabilir. Düzlem dalga uyarımları için, geliş açısından bağımsız olarak Fabry-Perot rezonansından kaynaklanan geniş bir uzamsal filtrelemenin

gerçelliği gösterilmiştir. Gauss Işını uyarımında gelen dalganın açısal dağılımının etkisi incelenmiştir. Eş frekans eğrilerinin yorumlanmasıyla, düzlem olmayan dalga uyarımları için geliş ve gözlem alanlarında uzamsal süzme sayısal ve kuramsal olarak açıklanmıştır. Kuşak durdurma özelliği yanında uygun yapıların yani çiftli yüzey yapısının kullanımıyla FK'in saçılım özellikleri ayarlanabilir. Bu yüzey tabakası, yüzey dalgalarını destekleyerek elektromanyetik dalgalar için bir dalga kılavuzu vazifesi görür. Işık çizgisinin üstüne denk gelen frekanslarda yüzey dalgalarının geriye doğru sızan dalgalar şeklinde ışımasıyla çıkış açısının 0° ile 70° değerleri aralığında frekansa bağlı yönlendirme yapılabilmektedir. Sızan dalga ve geriye doğru ışıma davranışları sol elli davranışa (SOD) sahip Metamalzemeler ile benzerlik göstermektedir. Metal balık ağı (MBA) yapılarında gerçekleşen eksi kırınım (EK) bu tür metamalzemelerde görülen SOD özelikleri ışığında incelenmiştir. MBA desenli levhalardan oluşturulan bir kamada ölçülen EK, çıkarım analizinden elde edilen sonuçlar ile karşılaştırılmıştır. Metamalzemede tektürleşmenin sınırları incelenmiştir. MBA değişkenleri ile SOD arasındaki ilişki, manyetik rezonans frekansı olan 14.3 GHz (ω_m) incelenmiş ve örneğin levhalar arası mesafe a_s=λ/10.5'ten (2mm) a_s=λ/4.2'ye (4mm) artarken EK indisinin -1.8'ten -1.3'e düştüğü görülmüştür. MBA yapılarının LC (indüktör ve sığa) rezonatör davranışı yanında TEM dalgakılavuzu özelliği taşıdığı ve ω_m'da bir boyutlu iletim hattı olarak çalıştığı ortaya konmuştur.

Anahtar Kelimeler: Fotonik Kristal, Derecelendirilmiş Kırılma İndisine Haiz Fotonik Kristaller, Odaklama, Dalgakılavuzu, Uzamsal Süzgeç, Geriye Sızmalı Dalgalar, Metamalzemeler, Eksi Kırılma İndisi

Acknowledgements

I would like to start by expressing my deepest gratitude and respect to Prof. Dr. Ekmel Ozbay. I have always felt his support and guidance. Moreover, It has been my acquisition as well as my joy to witness and visualize how a path to walk is created in his practice. The experience is one's own but there also co-exists the supporting power. In this sense, I am also grateful Dr. Gonca Özbay for her support: It is in the NANOTAM environment that my scientific nutshell could keep floating from the beginning of my PhD work towards the completion of this thesis.

I would like to thank to the members of my thesis committee, Prof. Dr. Orhan Aytür, Assoc. Prof. Dr. Ceyhun Bulutay, Assoc. Prof. Dr. Vakur B. Ertürk, and Assoc. Prof. Dr. Hamza Kurt for their guidance.

I am also grateful to Dr. Andriy E. Serebryannikov for his efforts and for the fruitful discussions. During this work, including our collaboration as well, the support of Miroslav Stefan, Andrushka and Tanya Serebryannikov has always been sensed.

I would like to express my pleasure to have collaborated with Prof. Filippo Capolino, Asst. Prof. Koray Aydın, Assoc. Prof. Kaan Güven, Dr. Zhaofeng Li, Dr. Kamil Boratay Alıcı, Dr. Hümeyra Çağlayan, Dr. İrfan Bulu, Dr. Serkan Bütün, Dr. Mutlu Gökkavas M. Deniz Çalışkan, Dr. Bayram Bütün (bbtn), Dr. Turgut Tut (ttut).

I also would like to thank to my colleagues, Neval Cinel, Damla Ateş, Semih Çakmakyapan, Ahmet Emin Akosman, Mehmet Mutlu.

It is my happiness to have worked with Atilla Özgür Çakmak (together with Fatma Çakmak). I am privileged to collaborate with him as he has always demonstrated how to carry out research. And, coming up with all those memories is a pleasure for me.

I also would like to thank to Gamze Seğmenoğlu, Nursel Aşıcı for making the affairs smoother and simpler for us and Mehmet Özgür for the technical support they provided in NANOTAM.

Last but not the least, I would like to acknowledge the support provided by the HIZAL CNC personnel in manufacturing the experimental tools used in this thesis work. I am grateful to Prof. Dr. Mirzahan Hızal for his help and guidance.

Anne Baba, siz olmasaydınız ben bu dünyada yoktum

Mum Dad, if not for you, I could not achieve my existence on Earth

Contents

List of Figures

List of Tables

Chapter 1

Introduction

Integrated photonic circuits offer a means to transmit digital information in electronics systems. This approach brings along the need for the manipulation of the electromagnetic wave propagation. Photonic Crystals (PC), metamaterials and surface plasmons attract attention due to the opportunities they provide with controlling the propagation as well as the radiation of the electromagnetic waves.

The PCs are multidimensional periodic dielectric structures with their spatial periodicity at the same length scale as the sub-wavelength of light. If the operating frequency of the incident light is within the prohibited frequency region, so called as the photonic band gap (PBG), then PC may act as a mirror reflecting the entire incoming wave [1]. The periodic nature of the crystal along with the high-index contrast dielectric materials governs some of the remarkable properties of PCs, such as self-collimation and super-prism [2-6]. The pure periodicity of PCs can be broken by introducing spatial perturbations in terms of

point or line type defects. As a result, artificially created modes can be localized in a small area or be guided through waveguides with sharp bends [7-12].

As for metamaterials, to start with the name itself, the phrase “Meta” which means “beyond” in Greek is used to express materials beyond those found in nature. Considering the natural materials that have been discovered up to date, the propagation of the electromagnetic waves obeys the right hand rule where the dot product of the phase velocity and the Poynting vector yield a positive value. Veselago had contemplated a Left Handed (LH) system in his seminal work, in which the phase and group velocities are in opposite directions [13]. He also formulated that such a LH medium possesses an effective Negative Refractive Index (NRI) when both of the effective constitutive parameters are less than zero. The feasibility of such an artificial material was reopened to discussion in [14] and [15]. The use of the Split Ring Resonators (SRRs) provides the magnetic resonance which is accompanied with a negative permeability over a certain frequency range [16], whereas a negative permittivity is observed by the use of wires [17]. By combining these two geometries the first experimental verification of a NRI is given in [18]. With the gained ability to adjust the permittivity and permeability values to a desired value enables interesting applications such as superlens [19], magnifying hyperlens [20], cloaking device [21]. Other possible applications cover inverse Doppler shift, Cerenkov radiation and many more.

In this work, main focus will be on PCs and metamaterials. After the introduction given in Chapter 1, the studies carried out on PCs will be summarized in Chapter 2 which covers sections 2.1 to 2.5. Then, in Chapter 3, the fishnet metamaterial structure will be examined.

After a brief summary of the Bloch modes which describe the field solutions in the PCs, from section 2.2 to section 2.5, applications of the PCs are demonstrated. In section 2.2, the focusing effect of the graded index photonic crystal (GRIN PC) is examined. It is seen that with the spatial modulation of the

regular PC into GRIN formation enables better spot size conversion ratio. In this form, GRIN is promising in terms of replacing bulky lenses in the optical systems.

In section 2.3, GRIN PC is shown to enhance the coupling efficiency of light into a waveguide. The coupling efficiency is tested in the microwave frequencies with the existence of the GRIN PC and without the GRIN PC. The FDTD simulations are shown to be in agreement with the measurements.

In section 2.4, it is shown that employing a square-lattice PC, the spatial bandstop and dual-bandpass filtering effects can be realized for the incident angle domain. At a proper frequency, a unidirectional transmission is observed. The iso-frequency contours are used to explain the transmission selectivity depending on the incident angle.

In section 2.5, a PC with a surface defect layer made of dimers is studied in the microwave regime. Three different regimes of the radiation are demonstrated. It is seen that for three different frequency intervals the PC with dimer layer behaves as a bandgap structure, a surface layer waveguide and a radiative structure enabling frequency dependent steering, respectively. The relation of the backward leaky waves and the dispersion characteristics of the dimer structure are studied.

In chapter 3, we have worked with both individual fishnet layers as well as a wedge-shaped fishnet structure. The validity of the homogenization and the prism effects are parametrically investigated with the wedge experiments in the microwave domain. The origins of the LH behavior in our design is explained by referring to the different debates on-going: one approach in interpreting the left handed behavior and the extraordinary transmission has been done referring to the artificial TEM waveguide modes of the subwavelength apertures. Other interpretation refers to the LC resonance in fishnet layers. Besides, two dimensional scan measurements obtained by employing the wedge structure are provided to compare the demonstrated NRI value with those apparent in the 2D

scan simulations. In addition, the retrieval analysis enables the extraction of effective parameters by using the S21 and S11 information. Applying the retrieval analysis to the pair of simulation and experimental results which is obtained by working with the fishnet layers, a second pair of NRI is obtained. This second pair of NRI is compared with the NRI pair found from the 2D scan experiments and simulation results which is obtained by working with the wedge-shaped fishnet structure.

Finally, chapter 4 summarizes the achievements in the thesis with a perspective on the recent trend of the research topics examined in the thesis.

Chapter 2

Photonic Crystals

2.1 Bloch Modes

Photonic Crystals are similar to Metamaterials since the periodic modulation of permittivity and/or permeability exist in both structures. This modulation period is much smaller than the operation wavelength in metamaterials. On the other hand, the modulation period is close to or larger than the operation wavelength in PCs. As a result, the electromagnetic properties of the medium cannot be described in terms of the effective medium parameters. Thus, homogenization is not possible for PCs, which makes them differ from Metamaterials.

The source-free Maxwell Equations i.e., Eqn. (2.1) and Eqn. (2.2) together with the constitutive relations given in Eqn. (2.3) and Eqn (2.4),

$$\nabla \times \vec{E} = -\frac{\partial \vec{B}}{\partial t} \qquad (2.1)$$

$$\nabla \times \vec{H} = \frac{\partial \vec{D}}{\partial t} \qquad (2.2)$$

$$\nabla \cdot \vec{D} = 0 \qquad (2.3) \qquad\qquad \nabla \cdot \vec{B} = 0 \qquad (2.4)$$

Since we are considering a linear and isotropic medium, we can write

$$\vec{D}(\vec{r},t) = \varepsilon_0 \varepsilon(\vec{r},t)\vec{E}(\vec{r},t) \qquad (2.5)$$

The permittivity can be written as $\varepsilon(\vec{r},t) = \varepsilon(\vec{r})$ since the medium is lossless and linear. For the case of PCs, the permittivity distribution is periodic, i.e.,

$$\varepsilon(\vec{r}) = \varepsilon(\vec{r} + \vec{a}_i) \qquad \text{(i=1, 2, 3)} \qquad (2.6)$$

where $\vec{a}_i$ is basis lattice vectors. As a result of this periodic permittivity distribution, Bloch modes are present as the electromagnetic response. Looking for monochromatic solutions which are in the following form,

$$\vec{E}(r,t) = \vec{E}(r)\exp(-i\varpi t) \text{ and } \vec{H}(r,t) = \vec{H}(r)\exp(-i\varpi t) \qquad (2.7)$$

and applying the $\nabla\times$ operator to Eqn. (2.1) and Eqn. (2.2), we obtain the following equations,

$$\Omega_E \vec{E}(r) = \frac{1}{\varepsilon(r)}\nabla\times\{\nabla\times\vec{E}(r)\} = \frac{\varpi^2}{c^2}\vec{E}(r) \qquad (2.8)$$

$$\Omega_H \vec{H}(r) = \nabla\times\{\frac{1}{\varepsilon(r)}\nabla\times\vec{H}(r)\} = \frac{\varpi^2}{c^2}\vec{H}(r) \qquad (2.9)$$

Here, $\Omega_E = \frac{1}{\varepsilon(r)}\nabla\times\{\nabla\times$ and $\Omega_H = \nabla\times\{\frac{1}{\varepsilon(r)}\nabla\times$ are the operators. ϖ is the eigen frequency and $\vec{E}(r)$ and $\vec{H}(r)$ are the eigen modes. Since the permittivity term $\varepsilon(\vec{r})$ is periodic as given in Eqn. (2.6), Bloch Theorem can be applied to the expressions given in Eqn. (2.7) yielding to the Bloch solutions or modes in the form:

$$\vec{E}(\vec{r}) = \vec{E}_{kn}(\vec{r}) = \vec{u}_{kn}(\vec{r})\exp(i\vec{k}\cdot\vec{r}) \qquad (2.10)$$
$$\vec{H}(\vec{r}) = \vec{H}_{kn}(\vec{r}) = \vec{v}_{kn}(\vec{r})\exp(i\vec{k}\cdot\vec{r})$$

where $\vec{k}$ is the wave vector and *n* is the band index. In Eqn. (2.10), $\vec{u}_{kn}(\vec{r})$ and $\vec{v}_{kn}(\vec{r})$ are again periodic with the same periodicity *a* of the PC i.e.,

$$\vec{u}_{kn}(\vec{r}) = \vec{u}_{kn}(\vec{r} + \vec{a}_i) \qquad (2.11)$$
$$\vec{v}_{kn}(\vec{r}) = \vec{v}_{kn}(\vec{r} + \vec{a}_i)$$

which renders a periodic modulation on the plane wave field solutions in Eqn. (2.10).

2.2 The Focusing Effect of Graded Index Photonic Crystals

2.2.1 INTRODUCTION

In addition to guiding and confining the light, focusing it to a small spot size is an imperative procedure in photonics. The bulky lenses with curved surfaces have to be replaced with more compact ones. PCs also possess potential for this kind of application. Plano-concave lenses that are obtained with PCs that have a negative effective index and left-handed electromagnetic properties have been proposed to focus the light [22-27]. There have been various other studies addressing the different applications of PCs that certain types of structural modifications are introduced. The self-collimation, focusing, mirage and super-bending effects were explored previously with the graded PCs [28-31]. The beaming effect from a corrugated concave surface of PCs was studied in Ref. [32], in which the pattern of the emitted beam demonstrated the focusing effect. In this section, we consider index based confinement using a graded index (GRIN) PC by modulating the lattice spacing of the crystal. The average index amount (the dielectric filling factor) is larger at the center of the PC than the sides, in which the incident wave with a planar wave-front converges towards

the central region. The surfaces of the GRIN PC are flat and the complete structure is very compact. We theoretically show and experimentally prove that only a few columns of PCs are capable of strongly focusing spatially wide beams to a narrow area. The appeal of GRIN PC encourages us by using it as an interface device that can act as a coupler by enhancing the coupling efficiency of wide input beams to narrow PC waveguides. However, this aspect of the GRIN PC will be pursued in another study.

There can be other ways of achieving graded index variation rather than modulating the lattice spacing. The radii of the rods or the refractive index of the dielectric rod are the parameters to be engineered in order to have an index gradient along certain directions. The changes in the rod radii require precise and small increments. Furthermore, it limits the range of the index gradient that can be achieved. Similarly, the index changes of the rods require different materials to be used. As a result, when a comparison is made among the choices, we can state that the selected method that uses the lattice spacing seems to be more practical than the others. Therefore, in this study we modulate the lattice spacing in order to implement GRIN PC.

The advances in fabrication technology allow for the fabrication of them in the optical frequency regime. At the same time, the scalability of the Maxwell's equations makes it possible to scale the wavelength to any spectral region. Since targeting the microwave frequencies lifts some of the technological and practical burdens, the experimental work is performed at the microwave regime.

2.2.2 THE GRIN

The structure under study is composed of aluminum dielectric rods in an air background. The refractive index is taken to be n=3.13 and the radius of the rod is $r = 0.22a$, where a is the lattice constant. The unmodified PC structure has a

square-lattice crystal but the lattice spacing along the *y*-direction is altered. The GRIN PC geometry under study is shown in Fig. 2.2.1(a). It is a two-dimensional PC, in which the polarization is taken to be TM (electric field is parallel to the rods). The TE polarization is not considered in the study. The lattice spacing along the *y*-direction is changed, in turn keeping the spacing in the *x*-direction constant at *a*. Half of the GRIN PC that is surrounded by the dashed lines in Fig. 2.2.1(a) is enlarged and is shown in Fig. 2.2.1(b). The other half of the GRIN PC is the exact replica of this enlarged portion. The spatial increment $(\Delta y_{i+1} - \Delta y_i)$ occurs at every row of the dielectric rods where the subscript i takes the values from zero to six. The distances between each set of rows are labeled as $2\Delta y_i$. The rows closest to the central part have $2\Delta y_0 = 0.75a$ and the incremental step is taken to be $0.15a$. This means that $2\Delta y_1 = 1.3a$, $2\Delta y_2 = 1.6a$, etc. The reason behind this selection will be explained later. The width of the GRIN PC is $26.54a$ and the length of it is varied in order to study the focusing mechanism with respect to the column numbers. In the figure, there are N=8 columns that make the length become $(N-1)a$.

2.2.3 THE RESULTS AND DISCUSSION

The finite-difference time-domain (FDTD) method is carried out to observe the field propagation throughout the computational domain, which is terminated by the perfectly matched layer absorbing boundary condition [33]. The input source is a spatially broad modulated Gaussian pulse with a center frequency at a/λ=0.38. This center frequency is within the waveguide modes of a regular PCW that is obtained by removing one row of rods. In this study, only a GRIN PC structure is investigated, but the integration of GRIN PC with PCWs will be studied in another work.

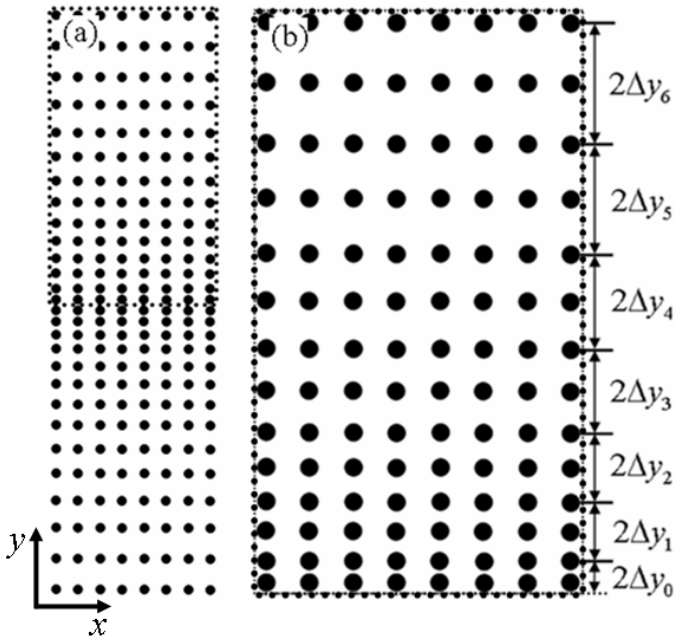

Figure 2.2.1 (a) The schematic representation of the graded index photonic crystals. The lattice spacing is increased along the *y*-direction and is kept constant at *a* along the *x*-direction. The details of the increments can be found in the text. (b) Half of the structure surrounded by the rectangular area with the dashed line is enlarged at the right hand side in the figure.

In order to decide the value of the incremental step value, four cases (0.05*a*, 0.10*a*, 0.15*a* and 0.20*a*) are selected and a comparison is made among them. Figure 2.2.2 shows the steady-state electric field map of these cases when a spatially broad Gaussian pulse is sent to different GRIN PC. As we can see in Fig. 2.2.2(a) and (b), small increments of 0.05*a* and 0.10*a* have less focusing power. As a result, the beam is partly focused. When we increase the increment step from 0.10*a* to 0.150*a*, the field becomes strongly focused at the focal point and the beam pattern shows small and periodic oscillations. There is not much change in the field's focusing behavior if the increment step is increased from 0.15*a* to 0.20*a*. As a result, $2(\Delta y_{i+1} - \Delta y_i) = 2(0.15)a$ is selected by considering the need to have a compact structure.

The focusing behavior of the designed GRIN PC with respect to the number of columns *N* is studied next. In this part, the number of the columns is

increased and the nature of the spatially broad incident beam is analyzed. The FWHM value of the beam at the focal point of the GRIN PC is recorded. The incident beams has an FWHM value of 9.20*a*. We can clearly see in Fig. 2.2.3(a) that one layer hardly shows the respective focusing behavior. As the layer number increases to two, the focusing effect of GRIN PC becomes more apparent. The FWHM values show little change after the layer number exceeds three. The decrement in the FWHM value means that the maximum peak of the field at the focal point increases and is also a measure of the focusing power. From the figure, we can claim that one may not need a very large PC structure in order to focus a wide beam to a small area. The power of the focusing behavior can be quantified by looking at the spot size conversion ratio, which is around 3.9. By sending even spatially broader pulses to GRIN PC in turn produces tightly focused beams. As a result, the spot size conversion ratio increases. For example, when the input pulse has a FWHM value of 17.5*a*, then the spot size conversion ratio becomes 7.4. We should note here that the finite size of the GRIN PC along the *y*-direction restricts the sending of spatially very wide pulses. The photonic devices that produce a small spot size ratio play a crucial role, especially for interconnect devices. Figure 2.2.3(b) shows the amplitude profile of the beam for three cases. The broadest profile with the solid line represents the input pulse without GRIN PC. The dashed and dotted lines indicate that the beam profiles at the exit side of the GRIN PC with N=4 and N=6, respectively. The strong focusing effect and small changes in the FWHM values of the beams after focusing occurs can be observed from the figure.

The magnitude of the steady-state electric field of the GRIN PC structure with four columns is monitored with the FDTD method. The result is shown in Fig. 2.2.4(a). The spatially wide input beam can be seen at the input side of the GRIN PC. The input beam reduces its spatial width considerably after traveling though a few columns of the dielectric rods and focuses to the central part of the

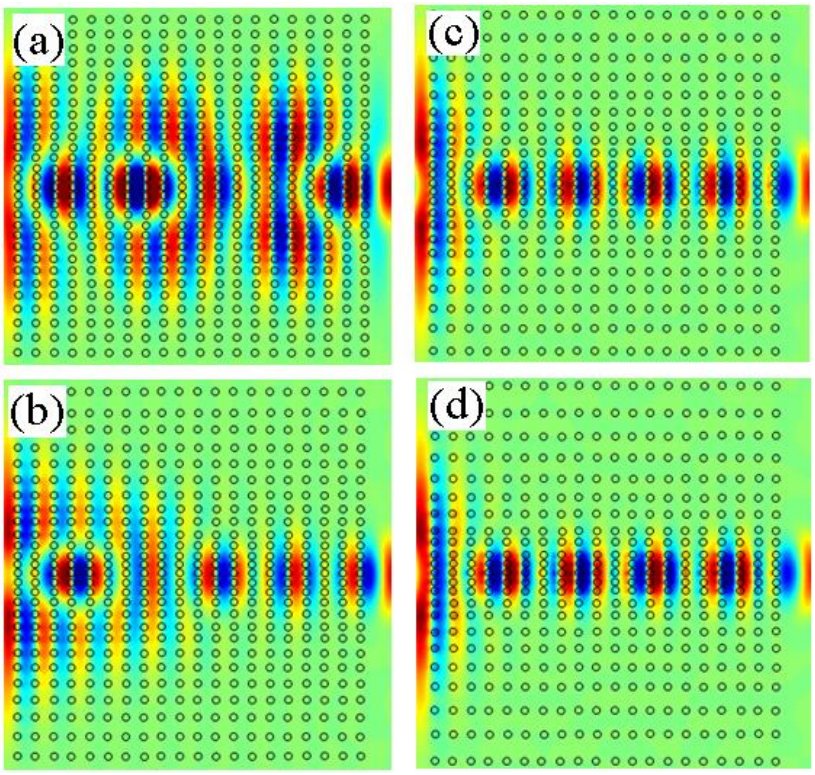

Figure 2.2.2. The electric field pattern of the incident Gaussian beam at the center frequency of a/λ =0.38 for four cases of increments. $\Delta y_{i+1} - \Delta y_i$ =0.05a for (a) and it is 0.10a, 0.15a and 0.20a for (b), (c) and (d), respectively.

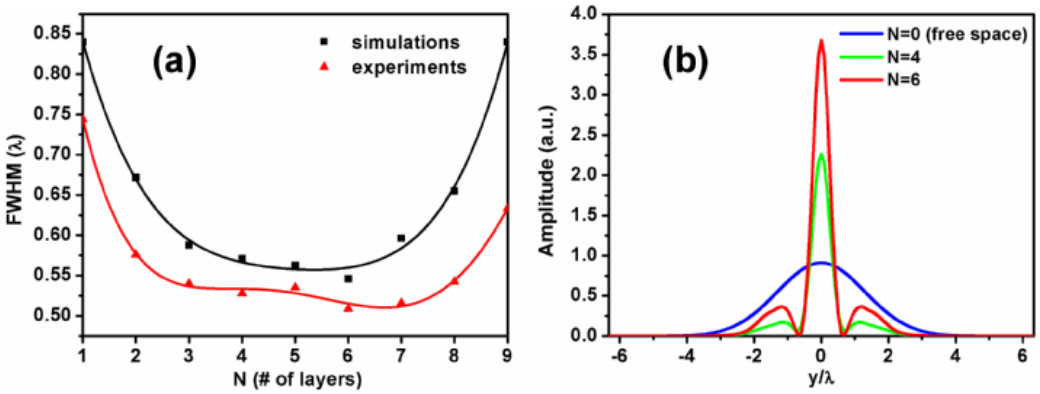

Figure 2.2.3 (a) The FWHM values for different number of GRIN layers. Simulation and experiment results have been fitted to curves. (b) Field profiles at the output side of the GRIN structure for N=4 layers (green line) and N=6 layers (red line). The free space profile (blue line) has also been added for comparison. The relative amplitudes of free space case and other cases in Fig. 2.2.3(b) are in scale.

structure. It remains confined within this central area. The experimental characterization of the designed GRIN PC, which is composed of aluminum rods with a=7 mm, is performed at 18 GHz by using a network analyzer as well as horn and monopole antennae. The horn antenna illuminates the structure at a distance of 70 mm and one monopole antenna at the output of the GRIN PC is used to capture the field scanning area. Figure 2.2.4(b) shows the measured intensity distribution at the exit side of the GRIN PC. The intensity is confined spatially to a narrow region. The measurement is in good agreement with the FDTD calculation. The cross sectional profiles of the *E*-fields at the focal point, 6 mm away from the photonic crystal surface, is also presented on the right hand sides in the figure.

A flat surface GRIN PC lens is obtained by modulating the lattice spacing of the PC. The curved surfaces of the conventional convex lenses behave in a similar way but their size is bulky and smooth curved surfaces are required, which places stringent requirements on the fabrication procedure. Our approach is free from curved surfaces, the structure is compact and it can be integrated easily with other photonic devices. Due to the high index contrast between the dielectric rods and the air background, the index gradient that is obtained by modulating the lattice spacing is also quite large compared to the traditional approaches. The presented results prove the importance of the engineering of the individual constituents of the PCs.

2.2.4 CONCLUSION

In conclusion, we performed the lattice space modulation of PCs in order to obtain graded index structures. The focusing behavior of the designed device

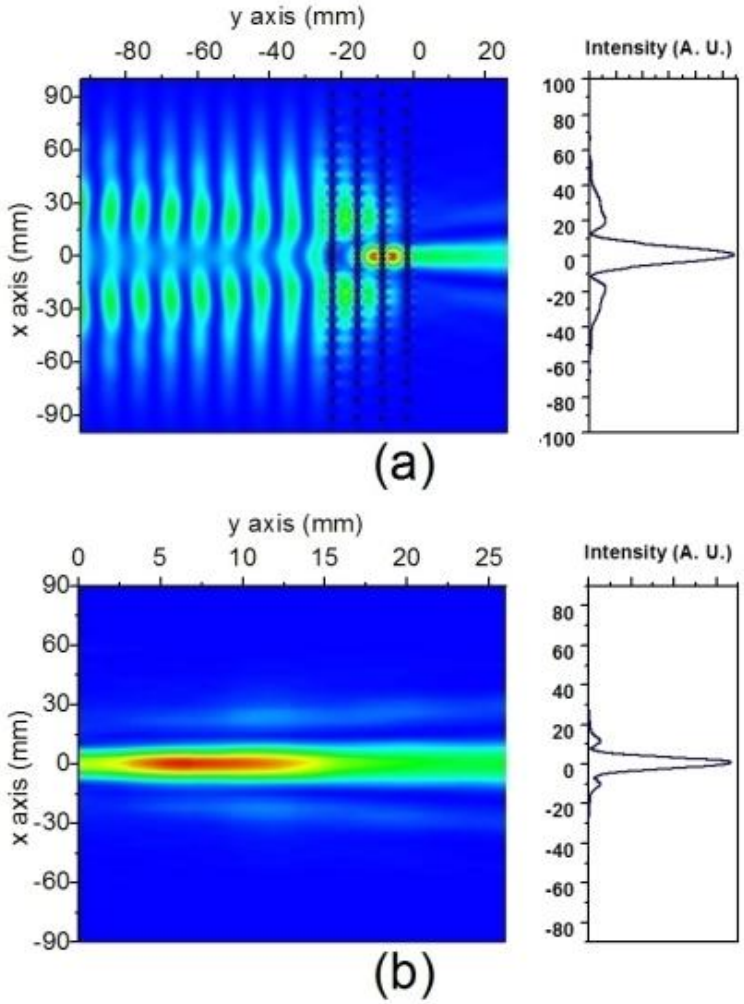

Figure 2.2.4. The focusing effect of the GRIN structure illuminated with a wide incident Gaussian beam at 18 GHz. (a) The electric field pattern obtained with FDTD for N=4 layers. The cross section profile of the E-field at the focal point, 6 mm away from the photonic crystal surface, is also presented on the right hand side. (b) The electric field pattern obtained experimentally by scanning the output side of the photonic crystal utilizing a monopole antenna. The cross section at the focal point is again given for convenience. The amplitudes in the images and the curves are normalized with the amplitude of the source for both the experimental and simulation results. Thus, the amplitudes in the corresponding plots are to be compared with each other.

was analyzed, both theoretically and experimentally and indicated that a small number of columns are sufficient to focus a spatially wide beam to a narrow region. The theoretical result obtained with the FDTD method agrees well with the result of the experiment that was performed at the microwave region. We

have proven that structural modification in PCs yields important features to manipulate the spatial profile of spatially wide incident beams

2.3 High Efficiency of Graded Index Photonic Crystal as an Input Coupler

2.3.1 INTRODUCTION

The developments of science in recent years have allowed photonic crystals to take their place among various applicable research areas rather than just being mentioned as an obscure physics topic [34,35]. The periodic arrangements of the PC structure offer superior performance over their conventional dielectric counterparts in optics. As a consequence, PC based devices have come to be fully appreciated due to their key features on controlling the flow of electromagnetic (EM) waves. A Photonic Crystal Waveguide (PCW) is an excellent example that has long been both theoretically and experimentally investigated [12,36,37]. PCWs are created by introducing line defects. These line defects guide the light with considerably reduced losses over sharp bends by strongly confining the propagating modes with the help of the Bragg reflection mechanisms. Thus, their wide usage in the field brought up the challenge of efficiently coupling light into PCWs. The mismatch between the modes of the external lightwave circuits and the PCW was accepted as the main reason for the poor coupling figures. Hence, several ways of tackling this problem were proposed. Adiabatically tapered fibers and dielectric waveguides were suggested as a solution to this obstacle [38,39]. The employment of gratings [40] and J-couplers, founded on the principles of parabolic mirrors, were adapted to overcome the difficulties [41,42]. Yet, the main attraction was directed towards

the utilization of the tapered PCWs that facilitate adiabatic mode conversion [43-52]. The supporting theoretical studies show promise for considerably high coupling efficiencies when we make use of these tapered PCWs [53,54]. Nonetheless, tapered PCWs have simultaneously led to serious drawbacks. Many of the approaches have depended on the complicated manufacturing steps. The slow reshaping process of the incident beam has required relatively long periods of the PCW to be sacrificed at both ends.

Efforts have been initiated to search for alternative methods that can compete and even replace the existing schemes. In that respect, the self collimation abilities of the PCs has received much attention [5,6,55,56]. The graded index (GRIN) version of the PC is a distinguished candidate in the literature for realizing the self focusing phenomena. A theoretical work was devoted to understand the critical design stages of the GRIN PCs [31]. Following that article, the GRIN PCs were integrated with PCWs to yield high coupling factors [57]. A GRIN PC that was composed of air holes was discussed in ref. 57, in which the index variation was achieved by properly adjusting the radius of the holes. Numerical analysis was carried out in order to emphasize the enhanced coupling figures. However, an experimental demonstration was not put forward. Therefore, the main objective of this study has been to experimentally verify the improved coupling that was attained with the assistance of the GRIN PC in the microwave regime. In the remaining part of this section, the experimental and simulation results are provided. Even though the finalized design of the GRIN structure and its theoretical examinations were the main scope of another work [58], a quick overview of the functionalized GRIN PC and the PCW is presented first. The experiments were accompanied by the numerical outcomes. Finally, the concluding remarks are laid out together with the performance issues concerning the coupling efficiency.

2.3.2 PCW

The scalability of the Maxwell's equations enables us to make analogies between the optical and microwave domain. An accurately scaled PCW, operating at the microwave frequencies, is a 2D representation of its optical equivalent. Figure 2.3.1(a) depicts the top view of the PCW that comprises sufficiently long (much longer than the operational wavelength) alumina rods with a dielectric constant of ε=9.61. The PCW is on the *x*-*z* plane and has a lattice constant of a=7 mm. The square lattice PCW stretches out 11 and 29 periods along the *x* and *z* directions, respectively. A row of rods starting from the 15^{th} rod on the *z*-axis was removed to create the line defect. Figure 2.3.1(b) illustrates the dispersion graph of the PCW for the TM polarization (E_y parallel to the rods) in the Γ-X direction. The defect band is highlighted with a red line while the rest of the blue bands all stay outside the band gap. The defect band supports a wide range of modes, including 18 GHz, which is designated as our working frequency and is restricted by the GRIN PC. The restriction is that the PCW must sustain the propagating mode while the GRIN PC allows high transmission. Simulations have been performed using a commercial FDTD tool called RSoft. Figure 2.3.1(c) shows the intensity distribution of the electric field. A single frequency (18 GHz), wide Gaussian beam with a FWHM of 3λ (λ being the operational wavelength) was launched from a distance towards the PCW. Only a small portion of the input beam was observed to be coupled to the waveguide due to the mode mismatches. This is analogous to what is happening at the optical frequencies as in the case of the butt coupling of different waveguide widths. A dielectric waveguide mode often also suffers from high coupling losses at the PCW interfaces. Moreover, as it can also be pointed out in Fig. 2.3.1(c), a portion of the incident beam was not localized within the line defect, since 18 GHz is close to the air band (Fig. 2.3.1(b)). Thus, the portion of the incident light hitting the PCW side walls in turn leaks out through the

structure. Consequently, the wave cannot be said to be confined to the waveguide, but rather tends to spread out. The adjacent figure corresponds to the intensity profile at the exit side of the PCW. The slice was taken at a distance of 5 mm (all of the distances are in mm). The combination of the diffraction mechanisms and the weak confinement of the wave hinder the overall performance and hence do not permit the high transmission. The next step was the realization of the experimental setup. A conventional horn antenna with the same FWHM value was utilized to send the incident beam to the PCW from 70 mm away. A monopole antenna was used to collect the beams at the output side while the network analyzer kept record of the measured intensities. The shortcomings of our experimental setup compelled us to scan only the output section of the PCW. Fig. 2.3.1(d) is the measured intensity distribution at the exit side of the PCW. The intensity profile suggests that the diffraction mechanisms and the coupling losses have once again governed the transmission experiment, which is consistent with the numerical scenario.

2.3.3 GRIN PC

The GRIN PC structure is designed by properly arranging the shifts in the longitudinal direction while keeping the lattice spacing constant along the *x*-axis. It is portrayed in Fig. 2.3.2(a). The variation is sustained such that the density of the rods is denser at the center of the GRIN PC. The EM wave prefers to travel at higher refractive index regions and as a result, a self focusing phenomenon is conveniently observed. The GRIN PC has translational symmetry over the *x*-axis. The symmetry axis divides the GRIN PC in such a way that it has 14 rods in both of the divided segments. The separation between two rods is determined by two variables, the constant factor of $b_0=0.5a$ and $\Delta b=0.15a$, which is altered at every two lattices. A 7 layered GRIN PC is

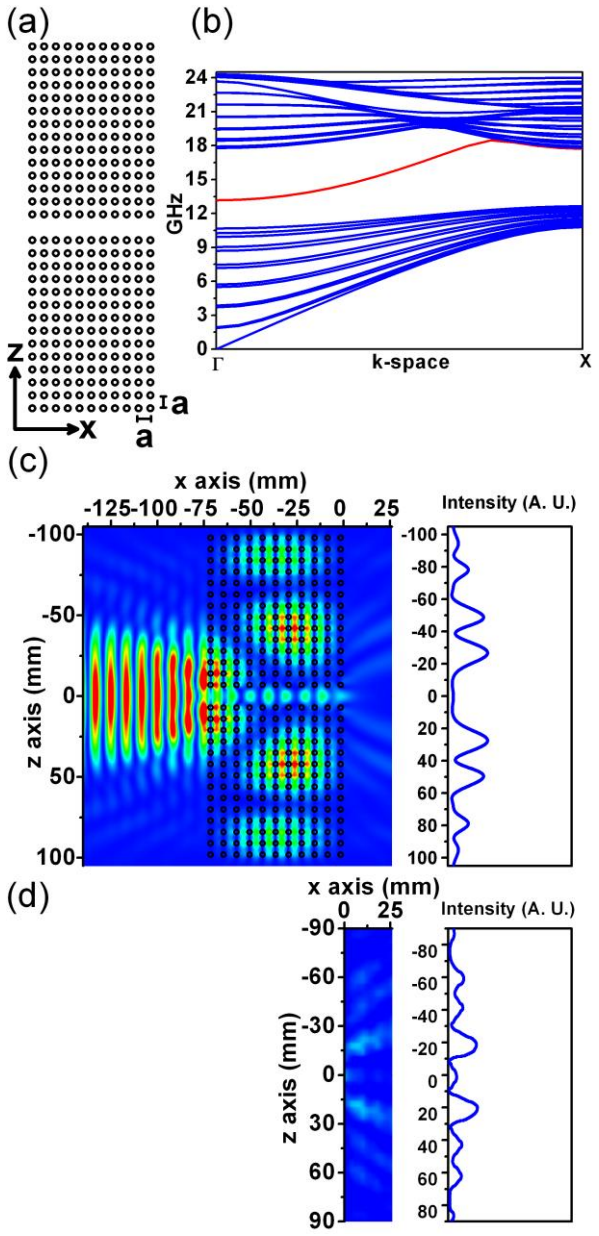

Figure 2.3.1. (a) Top view of the PCW structure. Alumina rods with ε=9.61, standing in the air (n=1), lattice constant, a=7 mm. (b) Dispersion diagram of the PCW structure along the Γ-X direction for TM polarization. The defect band is illustrated with the red line. (c) Simulation and, (d) experimental results of the intensity distributions of the electric field (E_y) at 18 GHz, A slice of the intensity distribution at the output side is also given at the right hand side of the main figure. The amplitudes in the images and the curves are normalized with the amplitude of the source for both the experimental and simulation results. Thus, the amplitudes of the corresponding plots are to be compared with each other.

considered for our particular case, but it was already shown that even a 4 layered GRIN PC would be enough to exhibit comparable self focusing effects [58]. First, the simulations were run to acquire the intensity distributions of the electric field when the GRIN PC was excited with a wide Gaussian beam. The numerical results predict that the shape of the wavefronts of the incoming wave is modified once the beam enters the GRIN PC. The accompanying intensity profile in Fig. 2.3.2(b) displays that a narrowed beam was generated as the product. A similar experimental setup was used to scan the output side of the GRIN PC. The experimental results reveal a very good agreement with the numerical conclusions. The measurements are shown in Fig. 2.3.2(c) and they imply that the GRIN PC acts like a lens with a certain focal length. The focal point is approximately found to be 4 mm away from the surface of the GRIN PC.

2.3.4 GRIN PC + PCW

In the next stage, the GRIN PC is cooperated along with the PCW to increase the coupling efficiency. The wide beam was to be squeezed down prior to being fed to the PCW by taking advantage of the focusing effect of the GRIN PC. It was experimentally checked to ensure that the optimum lateral spacing *d* between the two configurations was 4 mm. Then, the PCW was positioned around the focal point of the GRIN PC to give rise to the highest transmission figures, as shown in Fig. 2.3.3(a). The FDTD results of Fig. 2.3.3(b) assure enhanced transmission figures and immensely reduced coupling losses. Regardless of the weak confinement of the PCW at 18 GHz, the spatially narrowed EM wave, due to the GRIN PC, propagates without significant broadening and reaches the exit side while keeping its form. The numerical results were once again confirmed by the experimental measurements. When the

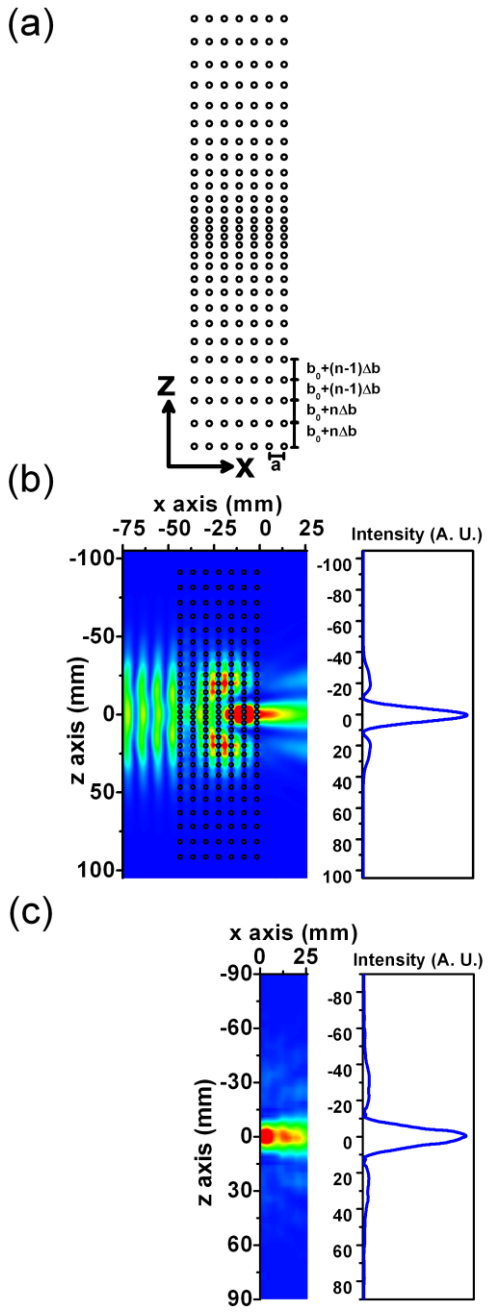

Figure 2.3.2. (a) Top view of the GRIN PC structure, composed of alumina rods, b_0=0.5*a* and Δb=0.15*a*. (b) Simulation and, (c) experimental results of the intensity distributions of the electric field (E_y) at 18 GHz, A slice of the intensity distribution at the output side is also given at the right hand side of the main figure. The amplitudes in the images and the curves are normalized with the amplitude of the source for both the experimental and simulation results. Thus, the amplitudes in the corresponding plots are to be compared with each other.

fields were probed at the exit interface of the PCW, it was observed that the profiles resembling the numerical outcomes were obtained experimentally, as in Fig. 2.3.3(c). It can be identified that this narrow mode does not have the capability to cover long distances after having departed the PCW. The diffractions are likely to destroy the shape of the outgoing wave. An output coupler might be needed to extract the waves from the PCW, but for our own purposes, we are contended with the validation of the improved coupling at the input side for the time being.

When the intensity profiles were collected only at the exit surface of the PCW, we witnessed the situations that are given in Fig. 2.3.4. Fig. 2.3.4(a) was drawn up solely based on the FDTD calculations, whereas Fig. 2.3.4(b) shows the experimental results. Both of the figures impressively demonstrate the effectiveness of using the GRIN PC as the input coupler. A wide incident beam with a FWHM of 3λ underwent a mode conversion ratio of 7.5 and arrived at the other side with a FWHM of 0.4λ. Similarly, the measurements offered a mode conversion ratio of 7.7. Given that the FWHM values are comparably smaller than the total window size of 10λ, integrals of the intensity profiles at the exit side should provide an estimation of the coupling efficiency for the GRIN PC. The Simpson's numerical integration technique was adapted for a range of $-5\lambda \leq z \leq 5\lambda$. Table I summarizes the coupling efficiencies of the simulations and experiments. The inclusion of the GRIN PC leads to 6.35 *dB* and 5 *dB* improvements in coupling mechanism numerically and experimentally, respectively.

2.3.5 CONCLUSION

In summary, the presented study is a proof of the utilization of the GRIN PC as an efficient input coupler for the PCW. As a result, the GRIN PC has been

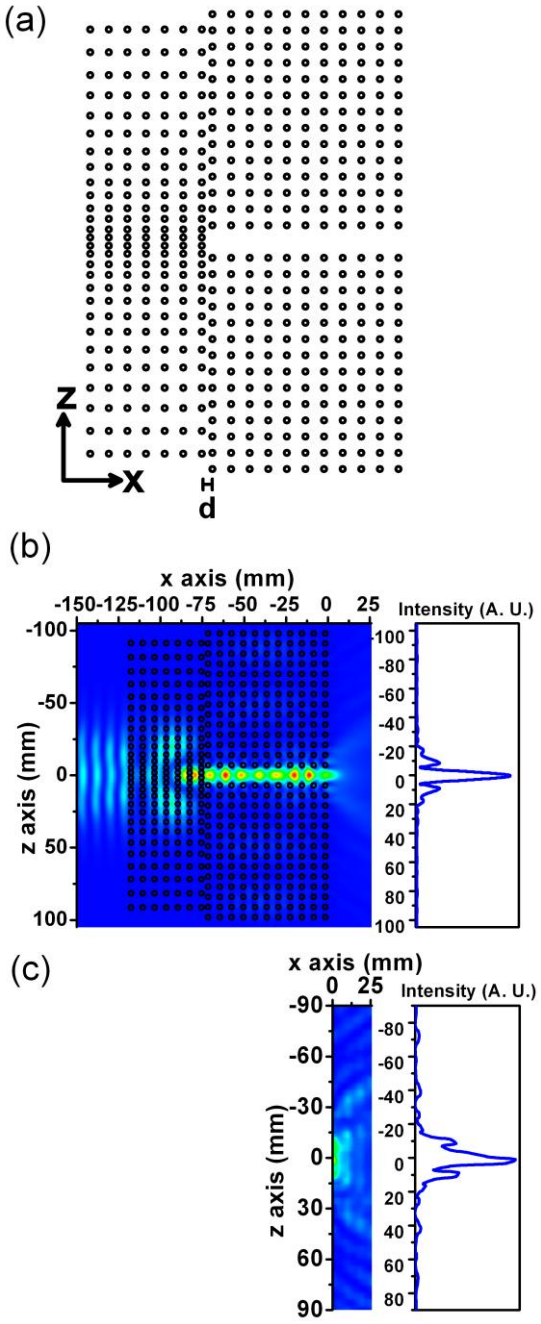

Figure 2.3.3. (a) Top view of the overall structure, d=4 mm. (b) Simulation and, (c) experimental results of the intensity distributions of the electric field (E_y) at 18 GHz, A slice of the intensity distribution at the output side is also given at the right hand side of the main figure. The amplitudes in the images and the curves are normalized with the amplitude of the source for both the experimental and simulation results. Thus, the corresponding plots are to be compared with each other

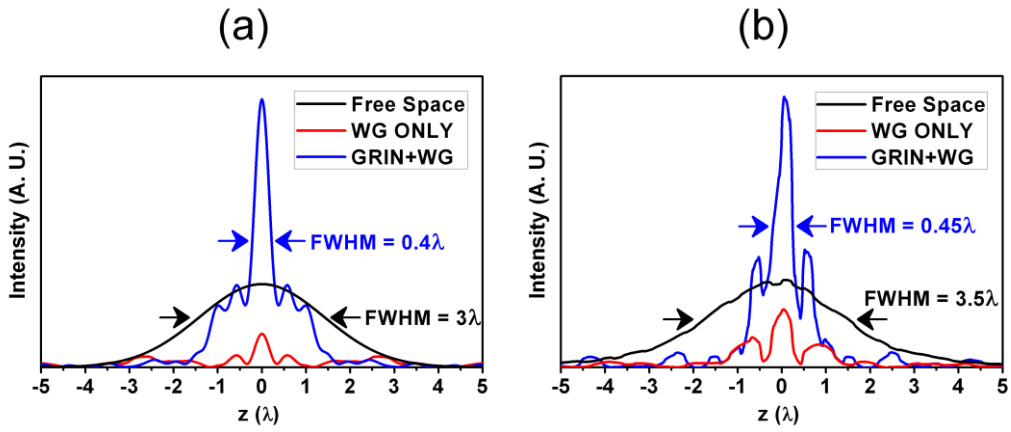

Figure 2.3.4. The intensity profiles at the output surface of the PCW: GRIN+PCW (solid blue line), PCW ONLY (solid red line). The free space intensity profile (solid black line) has also been given as a reference. (a) Numerical and, (b) experimental results. The relative amplitudes of free space case and other cases are in scale in both the simulation and the experimental results.

	Simulation	Experiment
$\frac{\int_{-5\lambda}^{5\lambda} \lvert E_y \rvert^2_{GRIN+PCW}}{\int_{-5\lambda}^{5\lambda} \lvert E_y \rvert^2_{PCW}}$	6.35 *dB*	5 *dB*

Table 2.3.1. The calculated numerical and experimental coupling efficiency of the system with the inclusion of the GRIN PC structure

experimentally shown to yield a coupling efficiency of 5 *dB* over the single PCW at 18 GHz. The successful experimental outcomes were backed up with detailed numerical analysis. Throughout the work summarized in this section, we attempted to make analogies between the microwave and optical domains as much as possible in order to address the complementary problem at the optical frequencies. PC manufacturing techniques have been well-founded in recent years. We believe that it is manageable to bring both the GRIN PC and the PCW to the optical domain. A horn antenna can be thought of as a representative of

the dielectric waveguides. Our proposed method can then be applied to attack the input coupling losses between PC structures and other lightwave circuits.

2.4 Spatial Filtering Using Dielectric Photonic Crystals at Beam-Type Excitations

2.4.1 Introduction

Spatial filters have been widely used for information processing and image enhancement in various ranges of electromagnetic spectrum. In particular, they were employed in the analysis of the spatial spectrum, the enhancement of the antenna directivity, radar data processing, aerial imaging and distinguishing the incoming radiations with respect to the source location. The known theoretical and experimental implementations of the spatial filters involve those based on anisotropic media [59], multilayer stacks that are combined with a prism [60], resonant grating systems [61], interference patterns [62], metallic grids over a ground plane [63], two-dimensional photonic crystals with [64] and without [65] defects, chirped PCs [66], as well as one-dimensional piecewise-homogeneous PCs [67] and graded-index PCs [68]. The coexisting spatial and frequency domain filtering has been studied in the context of controlling the laser radiation with the aid of the resonant grating based filters [69].

Smoothing or, in other words, “cleaning” the beams radiated by the high-power lasers is an important application of the low-pass spatial filters [67,69]. Filters of this type are considered to be comparably easier to realize since an anisotropic-like dispersion is not a prerequisite for the low-pass filters in contrast to the case of the high-pass and wide bandpass filters [59]. It has been shown in ref. 59 that wide adjacent ranges of transmittance, $T \leq 1$ and

reflectance, $R = 1$ can be obtained by using an anticutoff media, i.e., media with indefinite permittivity and permeability tensors. The simultaneous achievement of the high and nearly-constant transmittance within a wide range of the incident angle, ψ and a rather steep switching between the pass and stop bands constitute the general problems that are identified with the wide-band bandpass and bandstop filters.

In order to overcome these difficulties, an approach which has been offered for the plane-wave excitation [65], which is based on the use of the two-dimensional dielectric PCs possessing nearly-flat isofrequency contours (IFCs) and yielding diffraction for large ψ. In the case of a square-lattice PC, IFCs that are localized around M or X points of the Irreducible Brillouin zone are required for obtaining a bandpass spatial filter, whereas IFCs that are located simultaneously near either M and X points, or Γ and M points are needed for a bandstop spatial filter, specifically. It should be emphasized that the flatness of the IFCs is desirable for attaining high transmittance within an entire passband for the low-pass filtering, too. Therefore, a spatial filter based on a PC should be more advantageous than a performance that is based on the ultralow-index metallic wire medium [70].

In this work, we numerically and experimentally examine the spatial filtering mechanism, which is proposed in ref. 65. However, the study presented in this section discusses the realization of a PC based spatial filter operating under a beam-type excitation, instead of a hypothetical plane-wave illumination. The main goal is to demonstrate the principal features of the bandpass and bandstop spatial filters. First, we calculate the IFCs of the infinite PC. Secondly, the near-field results for a Gaussian-beam excitation are presented in order to demonstrate the collimation effects associated with the nature of the spatial filtering. Then, the far-field transmission results are investigated for a plane-wave excitation. They are exploited to determine the appropriate range of

frequency and PC lattice parameter variation for the purposes of a microwave experiment. Conventional horn antennas are employed in the microwave experiments. In turn, a wide Gaussian beam is introduced as an excitation source in the finite difference time domain (FDTD) simulations. The experimental results are presented and discussed together with the numerical outputs. The directional beaming at the output of the PC is investigated. The section is outlined by a short conclusion.

2.4.2 Theoretical background

Extensive numerical simulations have been carried out at plane-wave and Gaussian-beam excitations, in order to select a proper PC performance for experimental validation. Part of these results will be presented in the next section for the convenience. Based on the obtained results, we decided in favor of the PC that is composed of circular alumina rods with a permittivity $\varepsilon_r = 9.61$ and a diameter $d = 3.1\,\text{mm}$. The rods are arranged in a square lattice with a lattice constant, $a = 7\,\text{mm}$, so that $d/a = 0.4429$. The structure contains eight rod layers. The interfaces are assumed to be parallel to the Γ–X direction. The selected parameters are quite close to those in ref. 65. Accordingly, the basic dispersion and plane-wave transmission characteristics are expected to be similar to those in Figs. 2 and 4 from ref. 65.

We made use of the plane-wave expansion method while calculating the dispersion for the corresponding infinite PC. The dispersion curves are given in Fig. 2.4.1 for three typical values of a/λ. It is assumed that the input interface is parallel to k_x axis, while the PC is illuminated from the negative side of k_y axis. According to ref. 65, two nearly-flat IFCs must coexist at the same frequency in order to obtain a dual-bandpass or a bandstop spatial filter at $\operatorname{sgn}\psi = \text{const}$. The IFCs must be located in such a manner that the incident

plane-wave is coupled to a Floquet-Bloch (FB) wave of the PC only at large and small ψ. In other words, coupling to the FB waves at intermediate ψ values are avoided by positioning one of the IFCs near Γ point, while the other one is located near M point. Such two IFCs might appear due to either two different FB waves or the same FB wave, depending on the choice of the PC lattice parameters. In Fig. 2.4.1, the IFCs localized around Γ point belong to the 2nd lowest band of the PC. They are shrinking down as the frequency is increased. Conversely, the IFCs that reside in the 3rd lowest band are located in the vicinity of the M point. They expand outwards with the increasing frequency values. The IFC shape remains nearly the same, while the variations in frequency
lead only to the modification of the IFC width. The IFCs near M point leads to the appearance of the anticutoff-type pass band.

In the ideal case, the IFC flatness should be an indicator of the possibility of achieving the total transmission, $T = 1$, within a wide range of ψ–variation. In fact, if the operating frequency is chosen to be equal to that of an exotic Fabry-Perot resonance, one can stay in the close vicinity of this particular resonance in a broad span of ψ, in which the high transmission is sustained. This mechanism is distinguished from the classical ψ–dependent Fabry-Perot resonances, which are known to be the common feature for the cases of (approximately) isotropic dispersion, including some PC bands [71]. It is noteworthy that the same restriction of the nearly-flat shape of the IFCs is required for the spatial filtering as for imaging and collimation [72-74]. However, in contrast with the last two regimes, bandstop and bandpass spatial filtering is expected to be a result of a *partial* or, in other words, an *angle-dependent* collimation. Correspondingly, the location of the IFCs of the PC with respect to that in air should be different in case of spatial filtering. Indeed, the collimation should appear in this case at the plane-wave excitation only for the values of ψ, at which the incident wave is coupled to a FB wave. Otherwise, the total reflection should occur.

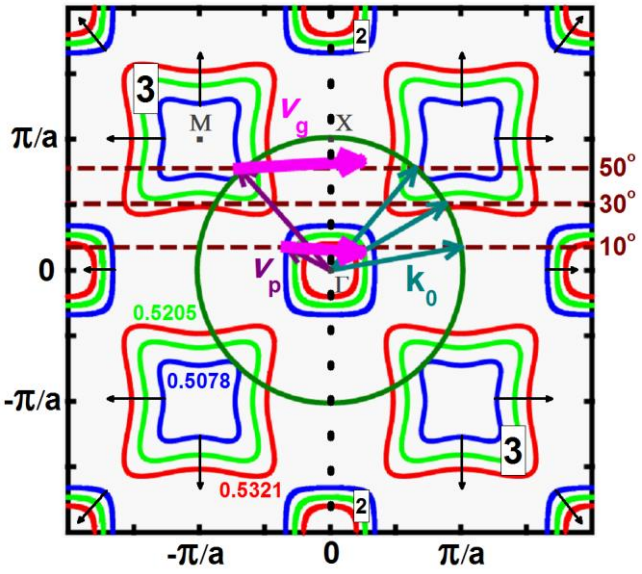

Figure 2.4.1. IFCs at $a/\lambda = 0.5078$ (blue contours), $a/\lambda = 0.5205$ (light green contours) and $a/\lambda = 0.5321$ (red contours). The boxed numbers on the IFCs signify the band numbers of the PC. Thin black arrows show the behavior of the IFCs as the frequency varies. The PC interface (dotted black line) is along Γ–X direction. Air band (dark green contour), the incident wave vectors (k_0, dark turquoise arrows), the phase velocities (v_p, purple arrows), the directions of the group velocities (v_g, thick pink arrows) and the construction lines (dashed wine-colored straight lines) at $\psi = 10^o$, $\psi = 30^o$ and $\psi = 50^o$ are shown for $a/\lambda = 0.5078$.

Specifically, the IFC for air may not be narrower than the PC IFCs, which are located near Γ point [65]. Then, the dual-band and bandstop ψ–ranges corresponding to these distinct frequency values are easily spotted in Fig. 2.4.1. The coupling mechanism has been explicitly examined for $a/\lambda = 0.5078$. The conservation of the tangential component of the incident wave vector at the PC interface (black dotted line along the Γ–X direction) dictates that the incident beam is coupled to a FB wave at $\psi = 10^o$ and $\psi = 50^o$ unlike the case at $\psi = 30^o$. This can be seen while inspecting the crossing points of the construction lines (dashed wine-colored lines). Furthermore, the refracted beams propagate nearly parallel to the surface normals (pink thick arrows) inside the PC as a result of the nearly-flat IFCs. The consequences of this collimation

effect are going to be discussed in the next section. To sum up, the dispersion curves offer a preliminary estimation of the overall behavior of the PC based spatial filtering and provide us the clues that comprise the coupling mechanisms for the particular incident angles as well as the fundamental significance of the nearly-flat IFCs.

In order to demonstrate the connection of a ψ–domain passband with the appearance of the collimation regime, near-field patterns were examined at a Gaussian-beam excitation. The Gaussian-wave has intentionally been chosen to be a wide beam with a width of $w = 15a$. Based on the near and far-field simulation results (not shown here), such a wide beam would enable us to make a fair analogy with the plane-wave illumination case. Figure 2.4.2 presents the near-field results corresponding to the large–ψ passband, which is associated with the IFCs located near M point. The field profiles are normalized individually with respect to the maximum electric field value at the particular frequency and incident angle. One can see in all of the four plots of Fig. 2.4.2 that the beam inside the PC propagates in the direction, which is nearly perpendicular to the interfaces and leaves the PC while being neither blurred nor substantially shifted.

It is seen in Fig. 2.4.2 that a large portion of the incident-beam energy can be transmitted through the PC, even at a rather large ψ, e.g. at $\psi = 60^{o}$. However, the level of the reflections within the passband vastly depends on ψ. The plane-wave passband is flat and shows $T = 1$ in the examples that are presented in ref. 65. Yet, this would not guarantee the total transmission at a beam-type excitation, because of the finite angular plane-wave spectrum of the latter. For a portion of the spectrum, coupling to the FB waves of the PC may take place, while for another one it may not. Furthermore, the effect of the PC interfaces can result in deviations from $T = 1$ even for the zero -order case, already for a

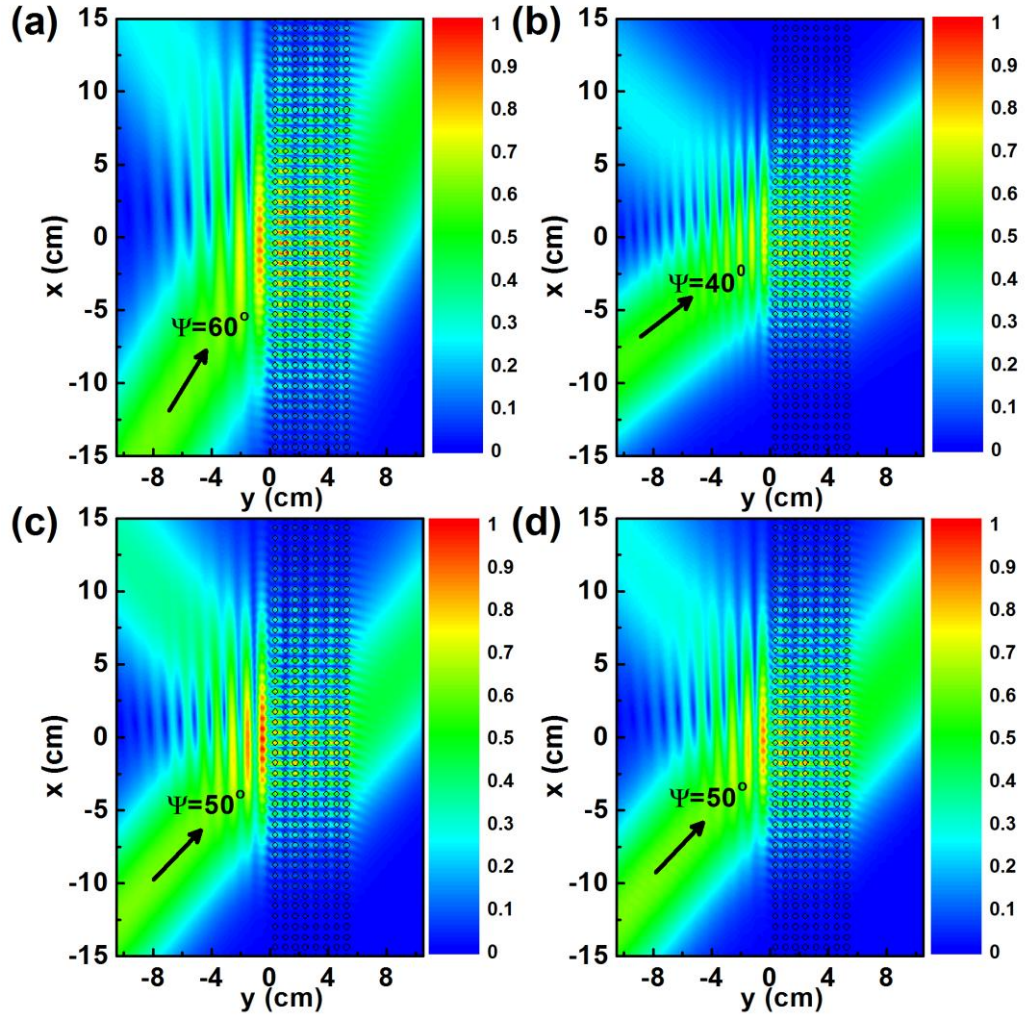

Figure 2.4.2. Electric field distributions at (a) $f = 21.763$ GHz, $a/\lambda = 0.5078$ and $\psi = 60^{o}$; (b) $f = 22.804$ GHz, $a/\lambda = 0.5321$ and $\psi = 40^{o}$; (c) $f = 22.804$ GHz, $a/\lambda = 0.5321$ and $\psi = 50^{o}$; (d) $f = 22.305$ GHz, $a/\lambda = 0.5205$ and $\psi = 50^{o}$.

plane-wave excitation. Thus, the cases that could be considered as the most appropriate ones for a plane-wave excitation are not necessarily the most suitable candidates for a non-plane-wave illumination.

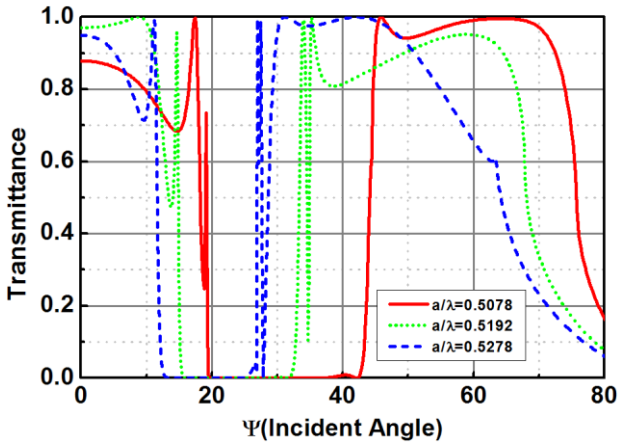

Figure 2.4.3. Zero-order transmittance vs ψ at $a/\lambda = 0.5078$ - solid red line, $a/\lambda = 0.5192$ - dotted green line, $a/\lambda = 0.5278$ - dashed blue line. The transmission due to the first-order diffraction is non-zero starting from $\psi = 75.8^{o}$, $\psi = 67^{o}$ and $\psi = 63.5^{o}$, respectively.

In spite of this, the transmission spectra at a plane-wave excitation can still be useful for a proper choice of the operating frequency, which should be equal or at least close to that of a Fabry-Perot-type resonance [75]. In this respect, the plane-wave transmission characteristics have been calculated by using an integral equation technique. The examples are depicted in Fig. 2.4.3 for the frequencies which lie in the same passband as in Fig. 2.4.2. The stopband is well pronounced in all three cases. One can notice that the passband arising between $\psi = 40^{o}$ and $\psi = 80^{o}$ for $a/\lambda = 0.5078$ (solid red line) is most appropriate for the purposes of bandpass filtering. In turn, the passband arising at $\psi < 16^{o}$ for $a/\lambda = 0.5192$ (dotted green line) seems most appropriate for the low-pass filtering. At least for the materials available at microwave frequencies, obtaining a PC performance, for which $T \approx 1$ simultaneously within the low–ψ and large–ψ ranges, is still a challenging task. Hence, the cases shown in Fig. 2.4.3 as well as other similar parameters can be considered as quite appropriate for the purposes of the study presented in this section. The near-edge peaks lead to

another problem to be solved. It should be noted that the passbands observed in Fig. 2.4.3 at small and large ψ correspond to the second and third lowest PC bands respectively, as it was already pointed out in the IFC diagrams [see Fig. 2.4.1]. Besides, the large–ψ passband is moving towards the smaller angles as the operating frequency is increased. The same feature is observed at the upper edge of the low–ψ passband. These features are consistent with the predictions based on the IFCs.

2.4.3 Experimental setup

The angular dependence of the transmission through the PC was measured for a wide range of ψ –variation. For this purpose, the experimental setup has been used, which contained Agilent two-port 8510C Network Analyzer and two conventional horn antennas with an operational frequency range from 18 GHz to 25 GHz [see Fig. 2.4.4]. The PC is assembled as an array of 8x100 alumina rods with a length of 15.4 cm. Even though there has accumulated a significant repertoire of the 3D PC studies in the extremely high frequency regimes over the last decade [76,77], the electrical length of the rods is longer than 10λ for every operational wavelength in our case, which safely allows our study to be considered as a 2D problem. The remaining parameters of the PC array are the same as mentioned above. A horn antenna, placed 25 cm away from the PC, was used as the source for TE polarization (electric field vector is parallel to the rod axes). The value of ψ has been varied from 0° to 77°. The measurements of the angular distribution of the transmission coefficient were carried out by employing another horn antenna as a receiver, which has scanned the semicircular path so that the receiver was kept 1m away from the center of the output interface of the PC, as shown in Fig. 2.4.4.

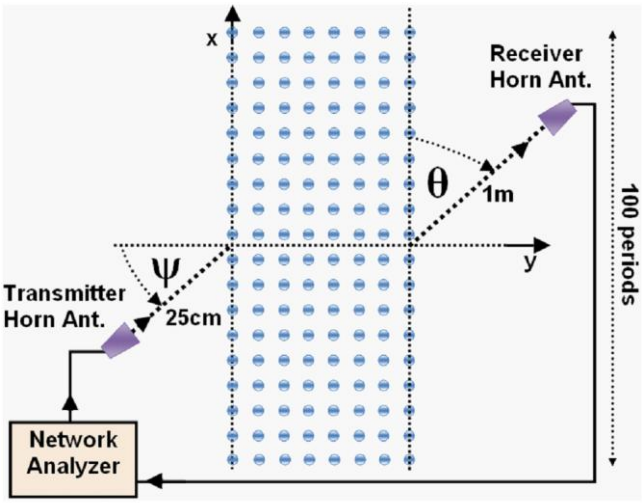

Figure 2.4.4. Schematic of the experimental setup.

The used antennas are standard reciprocal pyramidal horn antennas, which have a calculated directivity $D \approx 13.98$ *dB* and a half power beamwidth $HPBW \approx 18^{o}$ at $\lambda = 1.43$ cm ($f = 21$ GHz) for the H–plane (*x*–*y* plane in Fig. 2.4.4). The antenna directivity and thereby the radiation patterns differ within the frequency band of operation. The radiated fields of the horn antenna are expressed with rather complicated Fresnel Integrals [78]. In turn, the radius of curvature of the wavefronts at Gaussian-beam excitation in the simulations was evaluated to be $R = 18.38$ m at $\lambda = 1.43$ cm ($f = 21$ GHz) at the PC input interface. Such a high value ensures that the nearly-planar wavefronts do reach the PC interface at Gaussian-beam illumination. The Gaussian source that was employed in the simulations has been a bridge connecting the gap in between the hypothetical plane-wave illumination and the real life applications. On the other hand, the area of the horn aperture was 4.5x6.4 cm^2, so that the Fresnel number $F = A_{\max}^2 / L\lambda \approx 1.71$ at $\lambda = 1.43$ cm ($f = 21$ GHz), where $A_{\max} = 7.82$ cm at $L = 25$ cm for the transmitter antenna [79]. Hence, the input interface of the PC is located at the Fresnel zone of the transmitter antenna and the incident wavefronts keep the non-plane-wave features in the experiments.

The receiver antenna was of the same size as the transmitter one. A refocusing has not been applied to the transmitted field. The receiver antenna, which was situated 1 m apart, is close to the boundary its Fraunhofer zone. The experimental radiation patterns and the half power beamwidth attain values in the case without the PC, which are very close to the calculated free-space far-field results for the pyramidal horn antenna [78]. Likewise, the transmitter antenna could also be positioned 1 m away from the PC input interface in order to reshape the incident beam wavefronts, but this would in turn cause unwanted diffractions from the sides of the PC array. In fact, the PC acts as a large array antenna with a rather significant effective aperture size and contributes to the outgoing radiation at the output side [80,81]. Then, we are compelled to stay in the near-field for several meters of radial measurement distances. In summary, we are bound to put the horn antennas in the near-field regions on both sides of the PC at the operating frequencies throughout the measurements since some experimental difficulties (signal attenuation, wave broadening, parasitic diffractions and scattering losses) can appear for larger distances. In contrast to the Gaussian-beam excitation case, the incident beam arrives at the PC interface with non-planar wavefronts, which constitutes the main difference between the antenna and Gaussian-beam excitations. Nevertheless, in the next section, we are going to demonstrate that the basic principles of the spatial filtering are still achievable under these conditions.

2.4.4 Results and discussion

Results at several frequencies are presented simultaneously for the wide Gaussian-beam and the horn-antenna excitation, so that one can clearly see the effect of changing the type of the excitation. These results contain radiation patterns and transmission maps on the (θ, ψ)–plane, where θ is the observation

angle. The intensities are normalized with respect to the maximum attainable value at each frequency. Figure 2.4.5 presents the maps of transmission for the same frequency value as in Fig. 2.4.2(a) and in one of the case in Fig. 2.4.3. Two ψ –domain pass bands are observed, but their boundaries are now blurred due to the finite angular spectrum as opposed to the plane-wave results. Stop bands appear in both θ – and ψ –domains. There are no alternating minima and maxima within each passband, which further support that the spatial filtering mechanism is realized by staying in a rather close vicinity of the same Fabry-Perot type resonance.

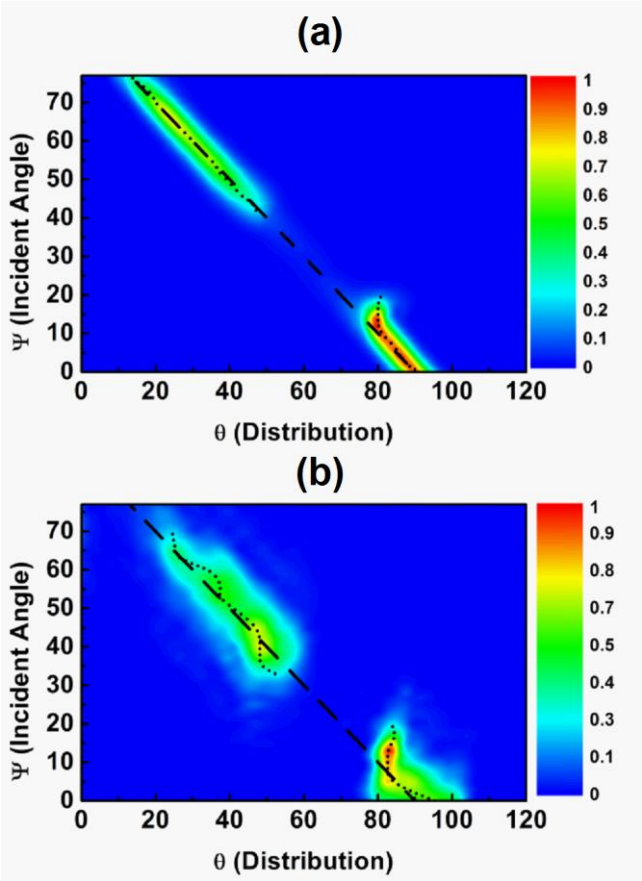

Figure 2.4.5. Transmittance on the (θ,ψ)–plane at $f = 21.763$ GHz ($a/\lambda = 0.5078$) for (a) Gaussian-beam excitation, FDTD simulations and (b) horn-antenna excitation, experiment.

The location of the stop bands in Fig. 2.4.5 can be quite well predicted using the plane-wave results. Nonetheless, the angular spectrum of the incident beam launched from the horn antenna is apparently wider, leading to broader $\theta-$ ranges of significant transmission at a fixed ψ. As a result, a substantial transmission happens to be detected in the experiments for the angle range, $35^{o} < \psi < 40^{o}$. The transmission within this particular range was either vanishing or insignificant at the Gaussian-beam and plane-wave illuminations. This might occur since the non-plane-wave features of the antenna illumination became more important, leading to the stronger contribution of the angular-spectrum components, which correspond to the stopband at the plane-wave excitation. Moreover, the upper boundary of the second passband is observed at a smaller ψ for the antenna case. Here, a bigger part of the angular spectrum should correspond to the values of ψ, at which the contribution of the zero order to the transmission in the plane-wave case is weaker.

In Fig. 2.4.5 and in all other similar figures, the dashed lines are expressed with the equation, $\theta = \pi/2 - \psi$, whereas the dotted lines designate the maximum value of the transmitted intensity at every ψ. When these two lines coincide, the collimation takes place. As a result, the dominant components in the angular spectrum of the incident wave (i.e., the plane-wave incident at angle ψ and its neighbors) propagate through the PC in the direction, which is perpendicular to its interfaces. Among the various causes of deviation of the dotted lines from the dashed ones, we should mention the non ideally flat IFCs and that a significant part of the wide angular spectrum can be out of resonance, so that different plane-wave components contribute to the transmission with different weights. The latter cause is especially important for the horn-antenna excitation. In spite of this, the collimation-like behavior is still evident in the second passband, in accordance with our earlier claims about Fig. 2.4.2.

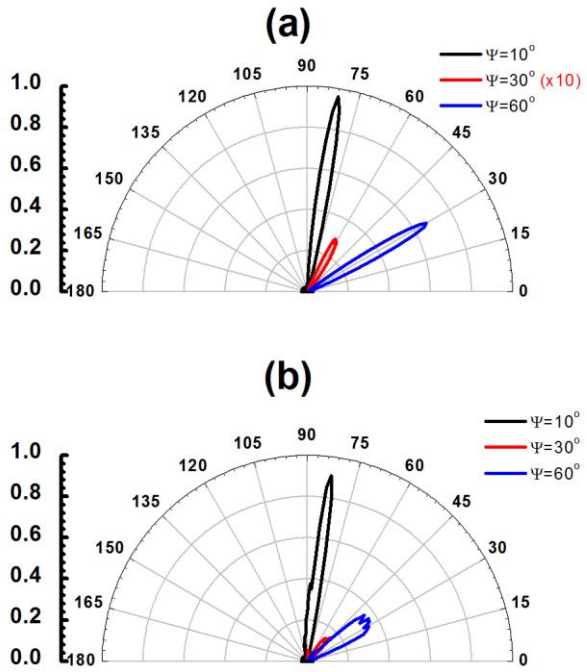

Figure 2.4.6. Radiation patterns for Fig. 2.4.5 at three typical values of ψ. The case of $\psi = 10^{o}$ is denoted with black color, the case of $\psi = 30^{o}$ (multiplied with a factor of 10 for the visualization purposes in (a)) is denoted with red color, the case of $\psi = 60^{o}$ is denoted with blue color: (a) Gaussian-beam excitation, FDTD simulations, (b) horn-antenna excitation, experiment.

However, when we inspect the dotted lines in Fig. 2.4.5 in the vicinity of $10^{o} < \psi < 20^{o}$, we notice the signatures of negative refraction [82,83]. In fact, the deviation of the dotted lines toward larger ψ at a fixed θ suggests negative refraction, which is in agreement with the dispersion features. The strong bending of the IFCs at the edge of the second lowest PC band, for which the IFCs are localized around Γ point, leads to a well pronounced negative refraction [see Fig. 2.4.1]. It is interesting that this effect is enhanced for the horn-antenna excitation owing to a wider angular spectrum of the incident wave. Moreover, a collection of the radiation patterns at $a/\lambda = 0.5078$, which correspond to the ψ–domain first pass band (smaller ψ), stop band (intermediate

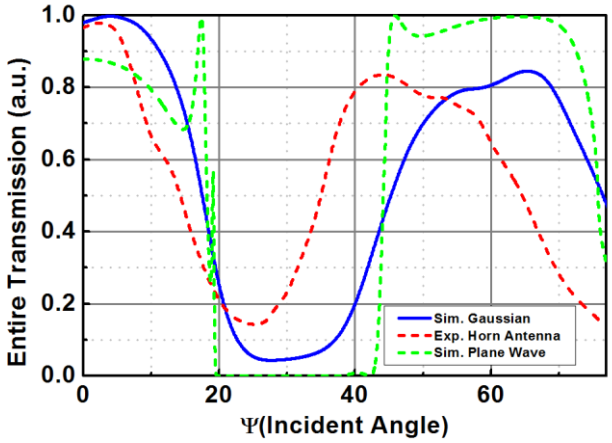

Figure 2.4.7. Entire transmittance for different illuminations at $f = 21.763$ GHz ($a/\lambda = 0.5078$) for Gaussian-beam excitation (solid blue line), horn-antenna excitation in the experiments (dashed red line) and plane-wave excitation (dashed green line).

ψ) and second pass band (larger ψ) in Fig. 2.4.5, are presented in Fig. 2.4.6. Radiation patterns simply consist of single slices that are extracted from the transmission maps at a desired incident angle.

Figure 2.4.7 portrays the entire transmittance T_Σ that is acquired by numerically integrating the transmitted intensity values over all observation angles in Figs. 2.4.5(a) (solid blue line) and 2.4.5(b) (dashed red line), respectively. For the comparison, the plane-wave excitation results from Fig. 2.4.3 are also plotted in Fig. 2.4.7 (dashed green line). Despite the broadening of the angular spectrum, the basic features of the spatial filtering, which were detected for the plane-wave excitation, still manifest for non-plane-wave excitations. In particular, two passbands of $T_\Sigma > 0.5$ (3 *dB* point) do occur.

The locations, the widths and the transmission levels of the passbands can be altered by adjusting the operating frequency. The IFCs in Fig. 2.4.1 remind us that an increment in the frequency results in simultaneously narrowing the first and widening the second passbands. In Fig. 2.4.8 an example of a transmission map is shown at a higher frequency, which corresponds to $a/\lambda = 0.5321$. Now,

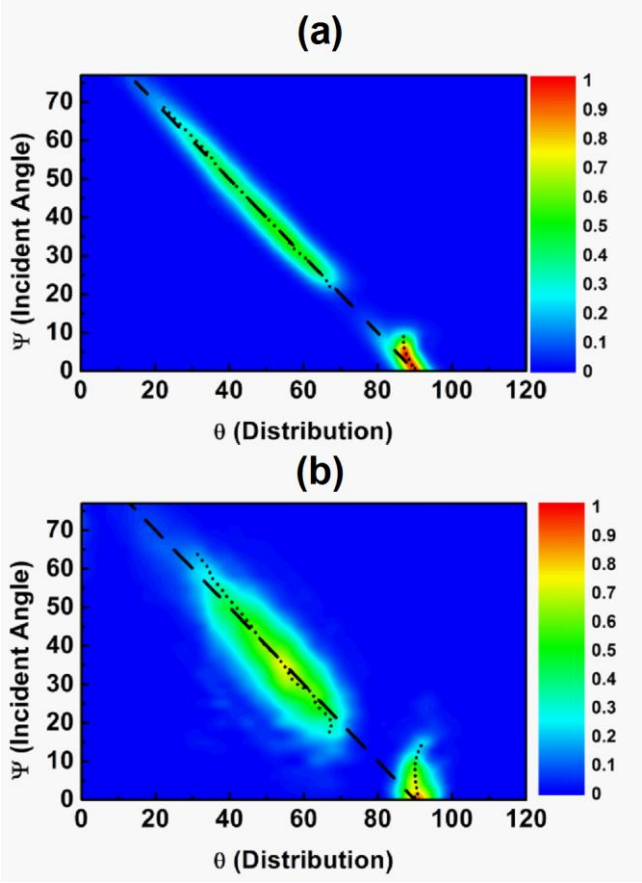

Figure 2.4.8. Transmittance on the (θ, ψ)–plane at $f = 22.804$ GHz ($a/\lambda = 0.5321$) for (a) Gaussian-beam excitation, FDTD simulations and (b) horn-antenna excitation, experiment.

the ψ–domain stopband is observed between the first and the second passbands only in the case of the Gaussian-beam illumination. At the same time, the θ–domain stopband is maintained for both cases of the non-plane-wave illumination. It should also be noted that the collimation of the incoming wave is reinforced in the second passband [compare Fig. 2.4.8(b) and Fig. 2.4.5(b)]. For the first passband, the signature of the negative refraction starts appearing in Fig. 2.4.8(b) already at $\psi \approx 0$. Figure 2.4.9 shows the radiation patterns for the three selected values of ψ. The slices are again particularly picked amongst the first passband (small ψ), stop band (intermediate ψ) and second pass band (large

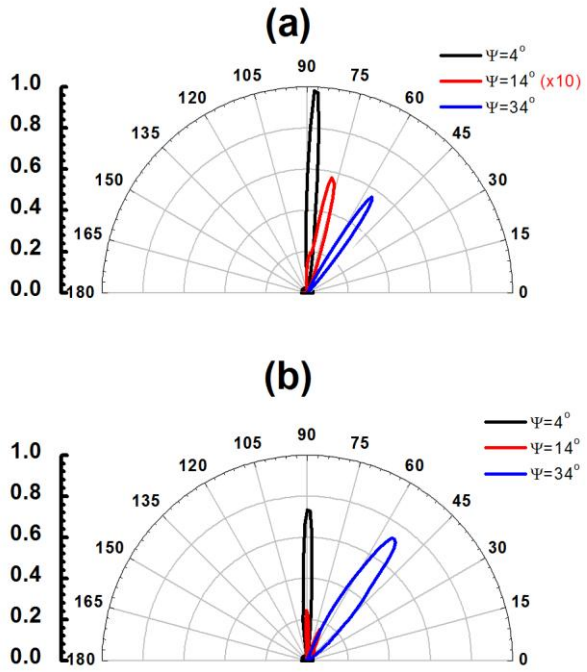

Figure 2.4.9. Radiation patterns for Fig. 2.4.8 at three typical values of ψ : $\psi = 4^{o}$ (denoted with black color), $\psi = 14^{o}$ (denoted with red color), $\psi = 34^{o}$ (denoted with blue color) (a) Gaussian-beam excitation, FDTD simulations, (b) horn-antenna excitation, experiment.

ψ) in Fig. 2.4.8(a). One can notice the deviation of the slice in Fig. 2.4.9(b) towards larger θ as compared to Fig. 2.4.9(a). This corresponds to the negative refraction arising at small ψ due to the contribution of the part of the angular spectrum that is associated with the plane-waves incident at larger angles.

Figure 2.4.10 presents the transmission map at a frequency value that is intermediate between those in Fig. 2.4.5 and Fig. 2.4.8. Here, it corresponds to $a/\lambda = 0.5192$, which is the same as in one of the cases in Fig. 2.4.3. The observed features are comparable to those in Figs. 2.4.5(b) and 2.4.8(b). The effect of spatial filtering is recognizable. However, now the lower boundary of the second ψ–domain passband and the upper boundary of the first passband nearly coincide. Thus, the stopband in ψ–domain tends to vanish. The radiation

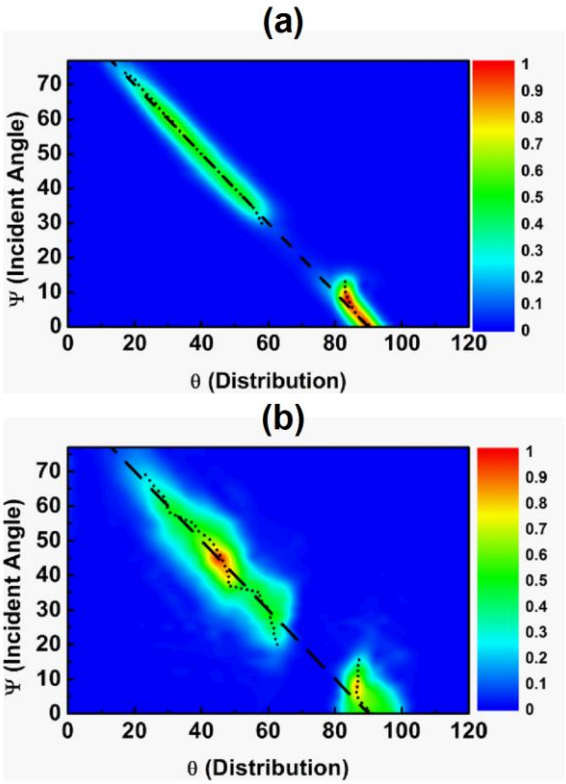

Figure 2.4.10. Transmittance on the (θ, ψ)–plane at $f = 22.252$ GHz ($a/\lambda = 0.5192$) for (a) Gaussian-beam excitation, FDTD simulations and (b) horn-antenna excitation, experiment.

patterns for the three selected values of ψ are presented in Fig. 2.4.11. The measured maximal values of T at $\psi = 10°$ and $\psi = 40°$ in Fig. 2.4.11(b) are close to each other. This is fairly the result of a special choice of ψ–values. The maximal values of T can vary with ψ rather strongly inside the first and second passbands (both for the cases that are shown and not shown), especially at the horn-antenna excitation. Furthermore, the first and the second passbands have different maximal values of T. These performance issues differ from the behavior of an ideal dual-bandpass filter. Yet, there are several effects which can lead to these discrepancies. First of all, one should mention the possibly different Fabry-Perot resonance frequencies for the two bands. The contribution

of the plane-wave components, which are out of resonance and the sensitivity of the transmittance values to a relatively weak variation in ψ in the vicinity of the resonance frequencies can be listed as additional reasons that are responsible for the deviations from an ideal filter performance. The diffractions at the PC interfaces also affect the transmission, while being dependent on the excitation type. These effects should be necessarily taken into account while designing and experimentally testing a spatial filter for an optimal performance. As it can be deduced from the relevant figures, a θ–domain stopband filtering is easier to succeed than a simultaneous stopband in the ψ – and θ–domains. Consequently, the frequency of operation should be downshifted if a wider ψ–domain stopband is aimed.

Lastly, the spatial filtering is accompanied with a directional beaming, which can be clearly inferred from the given radiation patterns. The directional beaming can already be obtained by utilizing the corrugations at the interface layers of the PCs by exploiting the surface waves [84-87]. Alternatively, the directional beaming has been studied in PC with self-collimation abilities [88].

Similarly, a collimation regime is observed together with a directional beaming in this study. The *HPBW* values stay lower than 20 degrees in the H–plane throughout the passbands for all cases, both in the simulations and experiments. This value is close to the calculated *HPBW* of the horn antennas in free-space (dashed purple-colored pattern in Fig. 2.4.11(b)). Moreover, the PCs are known to have the capability to further improve the directivity factors of the incorporated emission sources [89]. Likewise, an additional angular confinement of the emitted beam can be spotted in the measured radiation patterns. The used antennas have a $HPBW \approx 20^{o}$ at $a/\lambda = 0.5192$ for the free-space measurements (dashed green-colored pattern in Fig. 2.4.11(b)). Conversely, the spatial filtering mechanism promises a $HPBW \approx 11^{o}$ at $a/\lambda = 0.5192$ and $\psi = 40°$ in the second passband [see Fig. 2.4.11(b)]. The angular confinement of the beam is

even more improved at smaller observation angles, which corresponds to the first passband with negative refraction. The radiation patterns in Fig. 2.4.11(b) indicate that a $HPBW \approx 6^{o}$ can be achieved at $a/\lambda = 0.5192$ and $\psi = 10°$. Such narrow beams are attainable in the first passbands of the other studied cases, too [see Fig. 2.4.6(b) and Fig. 2.4.9(b)].

2.4.5 Conclusion

To summarize, dual-bandpass and bandstop spatial filters can be obtained in classical dielectric PCs by proper adjustments of the lattice parameters and the frequency range. The fundamental features of the spatial filtering have been demonstrated both theoretically and experimentally. The obtained results validate the possibility of utilizing the spatial filtering mechanism, which has recently been suggested for the plane-wave incidence, at non-plane-wave excitations like a wide Gaussian-beam and a Fresnel zone horn antenna. The extensive numerical and experimental studies have been performed for the former and the latter, respectively.

For the plane-wave excitation, the possibility of a wideband spatial filtering exists due to the specific Fabry-Perot type resonances, which are nearly independent on the angle of incidence. As a result, one can stay in the close vicinity of the same resonance, within a wide angle-domain passband while the frequency is fixed. In fact, the utilized mechanism can be interpreted in terms of the angle-dependent collimation, which appears in the PC with nearly-flat IFCs and provides a coupling of the incident wave to a FB wave in the PC within a limited range of the incidence angles. In case of a non-plane-wave excitation, the deviations from the plane-wave characteristics occur owing to the finite angular spectrum of the incoming waves. However, the basic features do remain. The near- field simulation results clearly put forward the existence of the

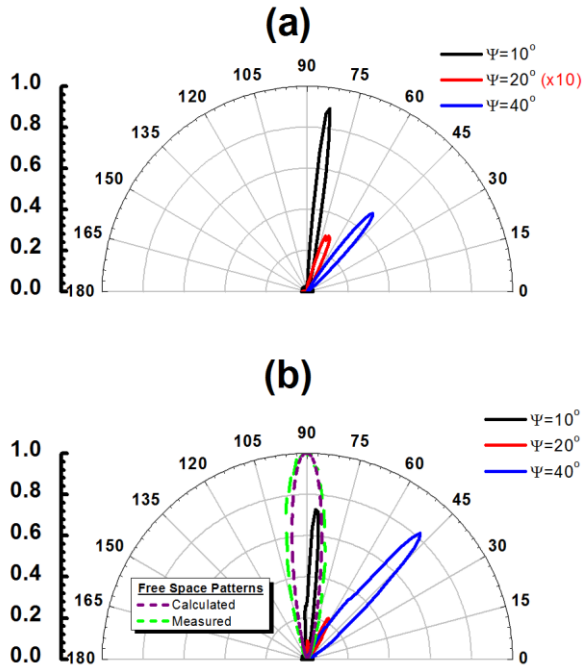

Figure 2.4.11. Radiation patterns for Fig. 2.4.10 at three typical values of ψ: $\psi = 10^{o}$ (denoted with black color), $\psi = 20^{o}$ (denoted with red color), $\psi = 40^{o}$ (denoted with blue color) (a) Gaussian-beam excitation, FDTD simulations, (b) horn-antenna excitation, experiment. The free-space radiation patterns of the horn antenna: calculated (dashed purple-colored pattern) and measured (dashed green-colored pattern) at $f = 22.252$ GHz ($a/\lambda = 0.5192$).

collimation regime at a Gaussian-beam excitation. The spatial filtering in the incidence and observation angle domains has been discussed in detail under the light of the numerical and experimental results obtained for the non-plane-wave excitations. The locations and the transmission levels of the passbands are examined as a function of frequency. The plane-wave transmission results and the dispersion results for the corresponding infinite PC usually provide the proper initial estimates for the passband locations at a non-plane-wave excitation. It is shown that the spatial filters can be engineered so that a stopband appears either simultaneously in the incident and observation angle domains, or only in the observation angle domain. Finally, the improvement of

the angular confinement of the outgoing beams is discussed with the aid of the measured radiation patterns.

Future works will include the design of the advanced single- and dual-bandpass spatial filters, as well as the theoretical studies attending the effect of the angular plane-wave spectrum and the curvature of the incident wavefronts, which have been beyond the main scope of the study presented in this section. The proposed spatial filtering mechanism is demonstrated to produce highly directional beams with improved angular confinement. It is expected that an experimental performance of the spatial filter with appropriate transmission and angular selectivity characteristics can be designed at the optical frequencies, too. Utilizing a defect-free PC should further ease the fabrication process. The adaptation of the proposed filter in the optical domain also relieves the restrictions on cooperating additional lenses and similar other optical devices for beam shaping and guiding, since the filtering mechanism is primarily handled by a single PC with a finite thickness. Eventually, it is anticipated that such a filter will have a wide range of applications in the optical communication systems as long as some form of an angular selectivity is needed.

2.5 Frequency dependent steering with backward leaky waves via photonic crystal interface

2.5.1 Introduction

Photonic Crystals [75,76,90,91] support Bloch surface waves [92]. In order to excite surface waves, a periodic surface defect layer may be placed at the exit of a PC waveguide [85-87]. These waves are analogous to Surface Plasmons (SP) that are generated on the surface of corrugated metal films [93-95]. Each

corrugation on the metal slab acts as a passive element of an array antenna, excited by its neighbors, which results in directional beaming. Similarly, in the case of a PC, surface waves are diffracted by the dielectric periodic surface scatterers, that are separated by intervals that are smaller than the free space wavelength [81,85-87,96]. In the aforementioned studies, however, the generation of a directional beam and its nature are investigated, rather than the steering of the directional beam. Other studies focused on the in-plane steering of the radiation angle without relying on surface waves [6,97,98]. Leaky wave antennas, which are basically radiative transmission lines, have been used to achieve beam steering in the endfire and backfire directions via forward and backward leaky waves [99]. An overview of the physics of leaky waves and their role in producing narrow-beam radiation, may be found in a pair of fundamental papers published by Tamir and Oliner in 1963 [100,101] and also in [102]. A frequency squint (i.e., the frequency dependence of the beaming angle) is typical of leaky wave radiators [102-105]. In certain leaky wave antennas the beaming angle was adjusted electronically by changing the applied control voltage [103,104] or mechanically by tuning the resonance frequency [105] at a single operation frequency. The use of interdigital capacitors along the transmission line [103, 106], the placement of dielectric rods in a waveguide [107], or working with a two dimensional array of copper wires [108] enables frequency dependent steering. In the work by Jackson et al. [109], a leaky wave explanation has been given for the problem of a plasmon wave on a corrugated silver surface, excited by a subwavelength aperture, that produces directive beaming of light. However, a beaming device relying on surface wave physics applicable at the optical wavelengths and that does not rely on plasmonic waves, has yet to be reported. The use of leaky surface waves on a PC which has frequency scalability property may serve this purpose.

In the section, we have studied the surface mode and the radiation mode of a 2 layer PC under a surface defect layer called as the “dimer-layer” (Fig. 2.5.1).

Previously, in addition to studies about the radiation behavior of sources placed inside PCs [110], the mechanism of directive radiation achieved via the surface of the PC has been already investigated [111]. The surface was regarded as a system of radiating sources whose resemblance with an array antenna was also shown. Here, the dimer-layer will be shown to support a backward guided bounded mode (surface wave) as well as a backward leaky mode. For the latter case, the PC structure behaves as a leaky wave antenna. Prior to our study presented here, the characteristics of surface waves propagating along a dimer-layer were investigated by Foteinopoulou et al. [112,113] and especially backward propagating waves constituted an important part of the investigation in [112]. In [113], a modified version of the Attenuated Total Reflection technique was used in order to experimentally display the backward wave propagation phenomenon. Waves radiated by an inclined horn antenna were coupled to the surface modes of the dimer-layer via a plexiglass prism. As an alternative approach, the exploitation of line sources placed inside the periodic configuration has been used to excite surface modes [114, 115]. We have adopted this latter approach in this study: a transverse monopole source is utilized to excite the surface and leaky modes in the dimer-layer. The dispersion diagram of the arrangement is obtained by employing the Rsoft Bandsolve Software which uses the Plane Wave Expansion (PWE) Method. Changes in the radiation angle of the beam as a function of frequency are confirmed experimentally. The measurement results are also supported by Finite Difference Time Domain (FDTD) Method simulations carried out with Rsoft Fullwave Software. Finally, the experiment concerning the half dimer-layer structure is used to explain the backward characteristics of the observed radiation.

2.5.2 Experiment and Analysis

Throughout this study, three configurations are experimentally investigated, for gaining physical insight into the formation of the narrow-angle radiation patterns: 2-Layer PC (PC2), 3-Layer PC (PC3) and 2-Layer PC with a dimer-layer (PCD), which are shown in Fig. 2.5.1. The PC and the dimer-layer are constructed with the same kind of alumina rods with a relative permittivity ε = 9.61 (refractive index n = 3.1). The rods have a diameter $2r$ = 3.2mm and a length of 15.4cm. The PC2 (Fig. 2.5.1(a)) is assembled as an array of 2x100 rods with a lattice spacing a = 9.6mm (r=a/6). The PC3 consists of 3x100 rods of the same kind placed with the same lattice spacing a (Fig. 2.5.1(b)). The dimer-layer placed on top of PC2 provides the PCD structure, which is the third one investigated in this work (Fig. 2.5.1(c)). Dimer rods are in contact to each other, in pairs, at the lattice corners with periodicity of a. Therefore, their center to center distance is $2r$=a/3. The monopole antenna is inserted at the mid–point, with respect to the x-direction, of the overall structure, half a lattice constant (a/2) away from the PC surface for each configuration. The monopole which has a low input reflection coefficient within the frequency band of 11-14.84 GHz (a/λ: 0.352-0.475) operates well as the excitation source. The excited transverse electric (TE) waves (along both the ±x directions) have an electric field component (E_y) parallel to the rods. As shown in Fig. 2.5.1(a), an Agilent two-port 5230A Programmable Network Analyzer (PNA) feeds the Agilent 8349B Microwave Microwave Amplifier, which drives the source antenna with a gain of 20dB. Angular distribution (AD) measurements of the transmission coefficient are carried out by employing a horn antenna as a receiver, scanning the semicircular path shown in Fig. 2.5.1(d), 1m away from the source.

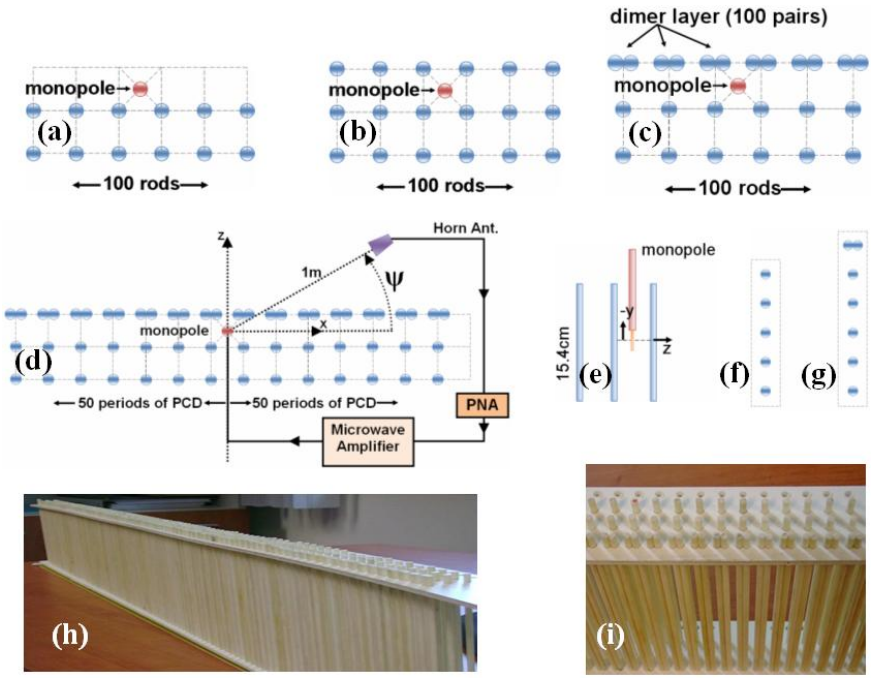

Figure 2.5.1. (a) PC2 structure, (b) PC3 structure, (c) PCD structure, (d) Experimental setup with the PCD, (e) side view of the monopole with the rods, (f) Single periodicity-cell of PC made of 5 layers (PC5), periodic along the *x*-direction (to be used in the simulations), (g) Single periodicity-cell consisting of the PC5 with a dimer on top, periodic along the *x*-direction, which is also used in the simulations, (h,i) images of the PCD that is constructed.

2.5.1.1 *Dispersion Diagram*

We first show in Fig. 2.5.2 the dispersion diagram of waves traveling along the *x*-direction for the two cases in Fig. 2.5.1(f) and 2.5.1(g), where the number of layers is the same as that considered in [112]. In particular, periodicity-cell for a PC (periodic along the *x*-direction) with 5 layers (PC5) stacked in the *z*-direction is shown in Fig. 2.5.1(f) and the structure, consisting of PC5 with a dimer-layer placed on the top is shown in Fig. 2.5.1(g). For the calculation of the band diagram, the unit cell is defined as periodic in both the *z*- and *x*-directions by the software used. The unit cell used in the simulations includes the structure shown either in Fig. 2.5.1(f) or Fig. 2.5.1(g) at the center. Besides, since we aim at simulating a structure periodic only in the *x*-direction, the periodicity of the unit cell along *z*-direction is modified as follows: Along the *z*-direction, 50

periods (*a*) of free space are left above and below the structure to be simulated (this free space region is not shown in Figs. 2.5.1(f) and 2.5.1(g)). Therefore the simulated periodic unit cell consists of a PC5 structure, with replicas separated by 100 periods (*a*) of empty space along the *z*-direction, which space is considered to be long enough to well approximate the finite number of layers of the actual structures along *z*-direction. The PC5 with the dimer-layer in Fig. 2.5.1(g) is simulated in the same manner. In the dispersion diagram, obtained by using the Rsoft Bandsolve softwave, k is the propagation wavenumber along the *x*-direction *and* a bandgap for $0.339<a/\lambda<0.468$ (10.59-14.62GHz) is observed for the PC5 structure (between the dashed curves in Fig. 2.5.2). For the PC5 with dimer-layer case instead, due to the presence of the dimer layer, a defect surface mode is introduced in the dispersion diagram similar to those provided in [112, 113]. The dotted curve for the surface mode in Fig. 2.5.2 has a negative slope. The figure shows the purely real part of the propagation constant of this mode below the light line. In the measurements, we will reduce the number of PC layers while in the interpretation of the experimental work, we are still going to rely on Fig. 2.5.2 since the fields radiated by the monopole would not significantly propagate through the bottom layers of the PC, in the frequency range investigated. That is, reduction of the number of layers in PC will have a minor effect on guiding and beaming of waves created within the bandgap of the PC.

2.5.2.2 *Radiation properties of a source embedded in the PCD*

The radiation characteristics of the three configurations (PC2, PC3 and PCD) excited by the monopole are simulated by using a 2D FDTD scheme of Rsoft Fullwave software and measured using the experimental setup with the same number of rods and layers like those used in Fig. 2.5.1. Both the simulated field strength and measured transmission coefficient results are collected at a distance of 1m from the center (where the source is located). The only difference is that

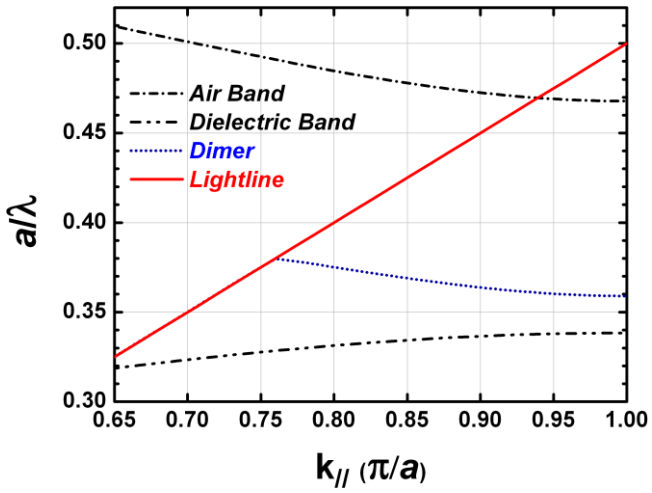

Figure 2.5.2. Dispersion diagram describing propagation along the *x*-direction. The surface mode in the dimer-layer (blue dot) resides inside the bandgap bounded by the air band (dash-dot) and the dielectric band (dashed with two dots) of the PC5 structure without dimer-layer.

in the simulation the structure has been approximated as infinitely long in the *y*-direction and excited by a line source.

Regarding the AD of the radiation from the monopole source which is measured in free space (i.e., without any PC), it is observed that the AD is not completely uniform in the angular range. Moreover, average value of the amplitudes in the AD decreases with increasing frequency. As a result, we have performed normalization to the measurement results with respect to source as follows: We have measured the AD of the transmission coefficient for the monopole in free space without any PC and then found the average value of the AD in the analyzed angular range (0°-180°) for each frequency. It is observed that, in the considered frequency range the variation in the average value of the AD of monopole in free space is highly correlated with the variation of the average AD of the measured transmission coefficient when the PC2, PC3 and PCD are used. Then, for the monopole which is measured in free space, we have found the least squares approximation (line fit) of the curve which represents the average value of the AD as a function of frequency. Finally for normalization, at

each frequency, values of AD of the transmission coefficient measured with a PC structure is divided by the value of the line fit at the same frequency. Normalization of the measurements with respect to the measurement of the monopole in free space carried out for PC2, PC3 and PCD. Whereas, for the line source simulated in free space, variation in the radiation is negligible in the angular and frequency range. As a result, no normalization is needed in the simulation results.

At each frequency of the simulations, the strength of the radiated signal is plotted in the Radiation Graph (RG) as a function of the observation angle (ψ) in Fig. 2.5.3(a), only for PCD. RG's of PC2 and PC3 are not given since they are not of main interest in this work. In Figure 2.5.3(b), the RG of the measured transmission coefficient is given. By polar-plotting a cross section at a fixed frequency (a/λ), the RG is used to extract the AD at that frequency. As a result, the values on the horizontal axis to which the peak values correspond, indicate the angular directions where the directive radiation occurs. The values in the RG are scaled such that the maximum value in the RG corresponds to 1 in both the simulations and the measurements to provide convenience in the radiation pattern comparison.

Three different cases will be of interest for us, whose distinction is made in terms of frequency ranges, based on what is observed in the dispersion diagram (Fig. 2.5.2) and in the RG of PCD (Fig. 2.5.3).

Case 1: The frequency range $\mathbf{0.339<a/\lambda<0.359}$ (10.59-11.22GHz) starts from the lower band edge and extends up to the lower-frequency tail of the dimer-layer mode shown in Fig. 2.5.2. These frequencies reside in the PC and PCD stopband and do not couple to the dimer-layer mode unless the frequency is too close to the minimum frequency of the dimer-layer mode. The AD plots of radiated field for the three configurations (PC2, PC3 and PCD) are drawn in Fig. 2.5.4 at the frequency a/λ=0.353. Although, for PCD, Figure 2.5.3 predicts no significant radiation for any angle at this frequency, Fig. 2.5.4 is given in order

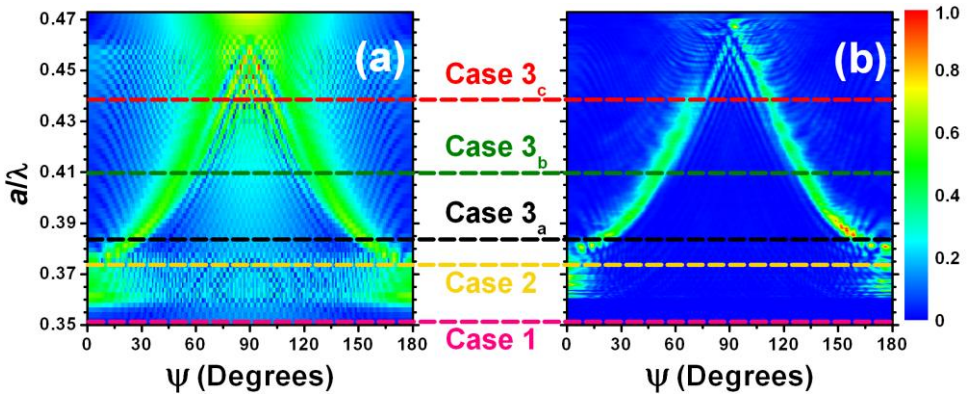

Figure 2.5.3. RG for the PCD obtained by FDTD simulation of the field strength (a) and by measurement of the transmission coefficient (b). Dashed lines represent the sample frequencies further investigated (magenta for Case 1, yellow for Case 2, black, green and red for Cases3a,b,c, respectively). For each case, a polar plot of the radiation pattern is provided. Comparing Fig. 2.5.3(a) to Fig 2.5.3(b), the discrepancies (i.e., non-symmetric appearance especially at high frequencies) in the measurement RG are attributed to the artifacts of the manufactured PCD and to the non ideal amplitude and frequency (i.e., non-uniform AD) characteristics of the monopole source.

to make a fair and consistent comparison between the investigated structures. Irregularities in the measurement results arise from the low power radiation levels. In all of the three configurations, radiation around $\psi=90^{o}$ is observed because either there are no rods in front of the source to prevent radiation (for PC2) or because of the poor filtering capability of a single layer of dielectric rods that is placed in front of the source (for PC3 and PCD). In Case 1, surface states are not excited so that propagation along the dimer-layer is negligible unless the frequency is close to the dimer-layer mode frequencies. Fig. 2.5.4(a) shows that at $a/\lambda=0.353$ a small radiation in the region $\psi=0°$ and $\psi=180°$ occurs for the PCD. This results from the minor surface propagation due to the weak excitation of the mode represented by the lower-frequency tail of the dimer-layer mode starting at $a/\lambda=0.359$ (Fig. 2.5.2). Moreover, in the PCD case the same minor surface propagation is the reason for the high frequency oscillations shown in Fig. 2.5.4(a). This issue is going to be clearer after the discussion of

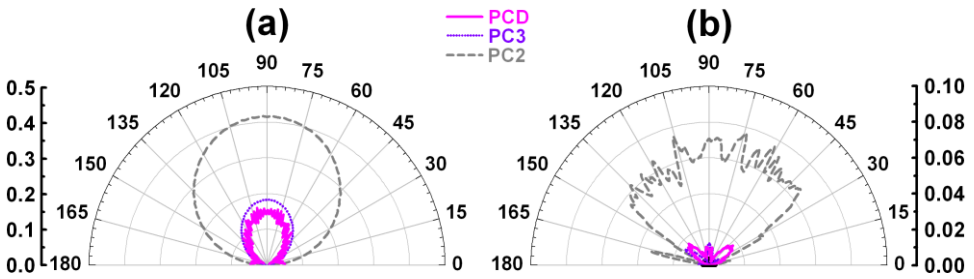

Figure 2.5.4. Normalized angular field distribution for Case 1 at a/λ=0.353. (a) Simulation results obtained from the RG in Fig. 2.5.3(a) (b) Measurement results obtained from the RG in Fig. 2.5.3(b).

surface modes and surface propagation in Case 2. These oscillations can not be recognized in the radiation pattern obtained by measurement given in Fig. 2.5.4(b), due to the very low signal strength.

Case 2 (the guided mode): The field excited by the source couples to the dimer-layer mode of the PCD, in the frequency region **0.359<*a*/λ<0.380** (11.22-11.88GHz). Below the light line (Fig. 2.5.2), the parallel wavenumber of the surface modes k along the x-direction, parallel to the surface of the dimer-layer, is larger than the free space wavenumber k_0. In this case, wave propagation along the dimer-layer is allowed and the power is propagating at grazing angle ($\psi=0^o$ and $\psi=180^o$) since in this case $k_0 \approx k$ (but still $k > k_0$), without significant radiation occurring off the dimer-layer surface. In this case, power is emitted also by the truncation-ends of the structure toward the $\pm x$ directions. Indeed, at an operation frequency of a/λ=0.373 (indicated by the yellow dashed line in Fig. 2.5.3(b)), the radiation main lobes are close to $\psi=0°$ and $\psi=180°$ (Fig. 2.5.5). Observation of the measured and simulated results implies the existence of guided waves along the surface due to surface mode which was observed in Fig. 2.5.2.

The oscillatory appearance in the radiation pattern is caused by the interference of the significant power coming out of the two edge-truncations because of the finite length (along x) of the PCD. In other words, the two ends of

the PCD, excited by the left and right traveling modes produced by the source, act like distinct radiating sources in addition to the direct source-field arising from the center. This situation was mentioned in discussion of Case 1 regarding the oscillations and lobes at grazing angle in the AD of PCD seen in Fig. 2.5.4(a). Since the operation frequency is still in the PC stop band, the angular field distributions relative to PC2 and PC3 do not exhibit any beaming produced by excitation of modes, which has been also similarly shown for Case 1.

Case 3 (the leaky mode): Frequencies higher than $\boldsymbol{a/\lambda=0.380}$ **(**11.88GHz) are the main focus of this study. At this frequency, the dimer mode crosses the light line (Fig. 2.5.2). Under this case, we make two propositions regarding the modes: **P1)** The wavenumber k possesses an imaginary part (i.e., k is not purely real) when the real part of $k < k_0$ (the region above the light line), as implied by the leaky wave theory [102]. **P2)** The curve representing the real part of the propagation constant of the mode in the dimer-layer still has negative slope above the light line. Hence, the mode has a negative group velocity ($v_g = d\omega/dk < 0$). A complex mode analysis will be carried out in a future study. Nevertheless, the following observations establish a strong base for our propositions concerning Case 3. Beyond $a/\lambda=0.380$, above the light line, k (we should say the real part of k) is smaller than k_0. The complex part of k is responsible for the radiation into the space above, on the right and left hand side of the PCD. Consequently, it is possible to attain two directive beams, at angles equal to ψ and $(180°-\psi)$, as shown in Fig. 2.5.6. Since k is decreasing when frequency increases, as a result of the situation mentioned in P2, the radiation angle approaches broadside, $\psi = 90°$, as the frequency increases beyond $a/\lambda=0.380$. This behavior can be observed in Fig. 2.5.3 and Fig. 2.5.6. The PCD structure transfers power into the space above in small increments contributed discretely from each dimer and the PCD behaves like a leaky wave antenna [116]. The evanescent wave (we recall that k has a complex value) attenuates while propagating toward the two lateral truncation-ends of the PCD. Since most

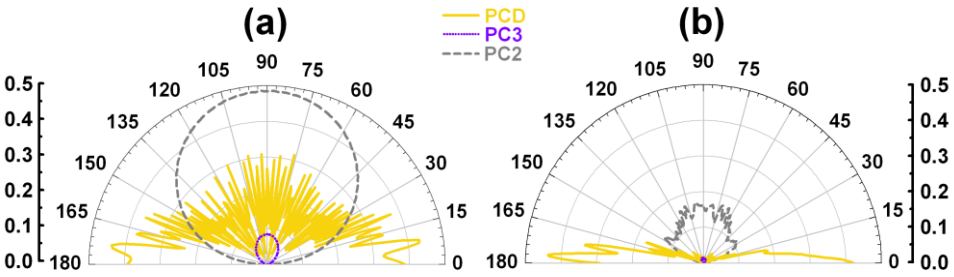

Figure 2.5.5. Normalized angular field distribution for Case 2 at a/λ=0.373. (a) Simulation results obtained from the RG in Fig. 2.5.3(a) (b) Measurement results obtained from the RG in Fig. 2.5.3(b).

of the surface power is radiated (leaked) into the space above, only a small portion reaches the two truncation-ends of the PCD. Therefore, the oscillations in the radiation pattern that were caused by the radiation of the two truncation-ends of PCD in Case 2 are now not present. In Fig. 2.5.6(a), the far field radiation patterns are simulated by employing the far field option of the Rsoft Fullwave software. The measurement results (Fig. 2.5.6(b)) obtained at a distance of 1m are compared to the far field simulation results. The radiation patterns tend to smooth out in the far field. Moreover, the far field patterns turn out to have narrower angular beamwidths. Nonetheless, measurements performed at a distance of 1m are sufficient to offer estimates of the far field antenna behavior. The far field condition (measurement distance > $2d^2/\lambda$) given in [78] suggests the measurements being carried out at a distance of at least 20m to obtain the approximate far field distribution. Here d=0.5m is the effective aperture of the antenna and λ=2.34cm is the wavelength corresponding to a/λ=0.41 which is an average value in the operation range. As a note, although the length of the PCD approximates 1m, the length of the effective aperture of the PCD which is responsible for the directive beam in a single quadrant covers only 0.5m, which is the length of the half section of the PCD structure. This issue will be clear when the PC with halved dimer-layer is studied in Section 2.3. The fact that for increasing frequency the beam scans toward the broadside

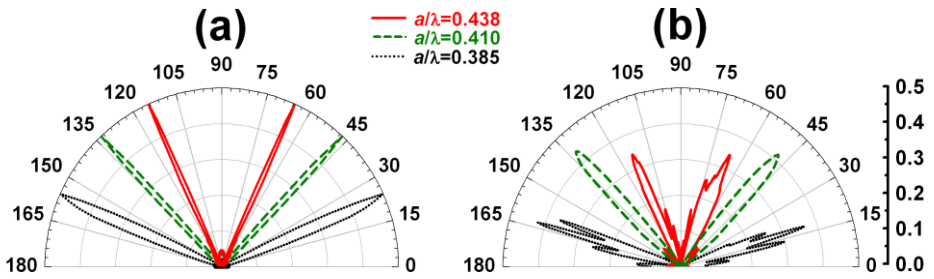

Figure 2.5.6. Angular field distribution for Case 3_{abc} (shown in Fig. 2.5.3) at frequencies a/λ=0.385 (black dotted line for Case 3_a), a/λ=0.410 (green dashed line for Case 3_b) and a/λ=0.438 (red solid line for Case 3_c). (a) Simulation results for the "far field" radiation pattern which are performed by Rsoft Fullwave software (previously, the simulation RG evaluated at 1m from the center was given in Fig. 2.5.3(a)). (b) Measurement results from the RG in Fig. 2.5.3(b). This shows that measurements performed at 1m provide an estimate of the far field radiation pattern.

direction ($\psi = 90°$) indicates that the leaky wave responsible for the directive radiation has a backward nature [102]. This is confirmed by the next experimental setup.

Calculated mode profiles of the electric field $|E_y|$ in the XZ plane are shown in Fig. 2.5.7 (with linear scale in arbitrary units) for the same input level of line source at two different frequencies. The excitation source is located between the dimer-layer and PC2, as depicted in Fig. 2.5.1(a) and here recognized by the strong field intensity at x=0mm, z=5mm. The mode profile in Fig. 2.5.7(a) confirms the presence of surface propagation at a/λ=0.373 that we have described in Case 2. Since there is not significant attenuation while propagating along the x-direction, most of the power reaches the two PCD truncation-ends. On the other hand, in Fig. 2.5.7(b), at a/λ=0.41 the guided (leaky) wave is attenuated while it propagates along the x-direction (we recall that in this case the real part of k is smaller than k_0) and only a very small amount of power reaches the two PCD truncation-ends. Because of their attenuation properties, leaky waves are not permitted to cover long distances, which shows the appropriateness of P1 in Case 3. In Fig. 2.5.7(c), the cross sections of the mode

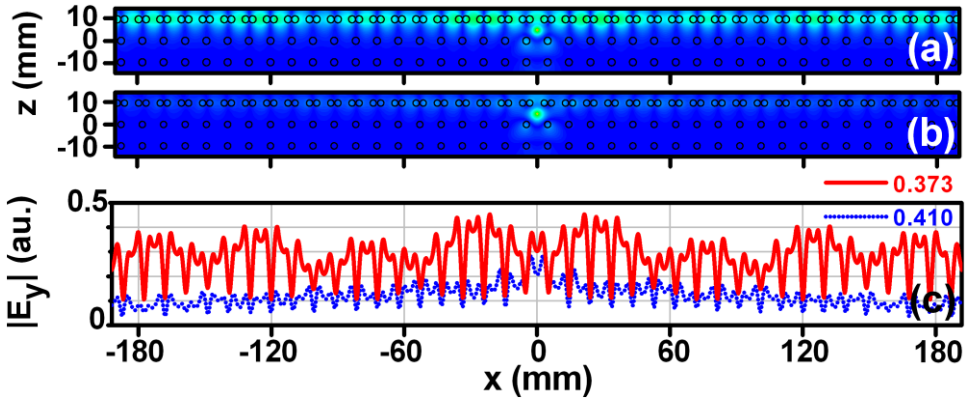

Figure 2.5.7. Calculated mode field profile for Case 2 and Case 3. (a) Case 2: the surface wave (guided) frequency is a/λ=0.373, (b) Case 3: the radiative (leaky wave) frequency is a/λ=0.41. (c) Cross sections of the mode profiles of Figs. 2.5.7(a) and 2.5.7(b), taken along x-direction passing through the center of the dimers are plotted in the same arbitrary units which is used in Fig. 2.5.3(a), Fig. 2.5.4(a) and Fig 2.5.5(a).

profiles are given, which are taken along x-direction passing through the center of the dimers to provide a quantitative comparison. It is seen that for a/λ=0.373, energy is transferred towards the ends whereas for a/λ=0.410 the signal is decreasing along the x-direction since energy is radiated into space above the dimer layer.

2.5.2.3 *Backward wave character and radiation property of the leaky mode excited in the dimer-layer*

We have already mentioned in our second proposition (**P2**) that Case 3 supports backward waves (with phase and group velocity traveling along opposite directions). This means that the radiative phenomena exhibit an interesting property. That is, the guided leaky wave with a negative phase velocity in the – (+) x direction (and positive group velocity, since power is emanated by the source in both the ± x directions) is responsible for the directional beaming in the 1st (2nd) quadrant of the polar plot. The dimer pairs on the left (right) hand side of the XZ plane act like elements of an array antenna and the cumulative interference provides the directive beaming in the range of

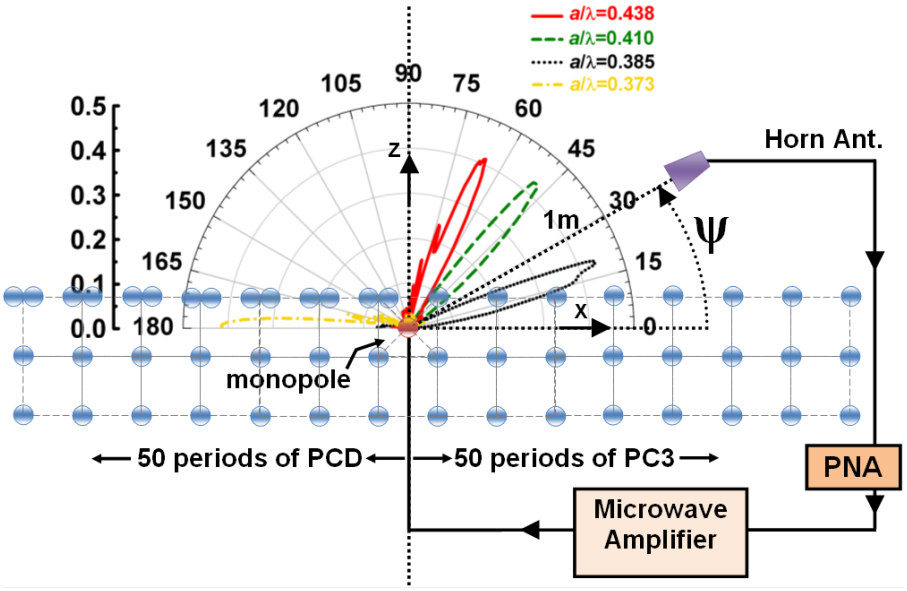

Figure 2.5.8. The experimental setup for PCHD and the normalized AD measurement. The angular field distribution is measured at a distance of 1m at frequencies of a/λ=0.373 (yellow dash-dotted line) which is the guiding frequency and at the beaming frequencies which are a/λ=0.385 (black dotted line), a/λ=0.410 (green dashed line), a/λ=0.438 (red solid line).

$0° < \psi < \sim 70°$ for the 1st ($180° > (180°-\psi) > \sim 110°$ in the 2nd) quadrant. This situation is typical of backward leaky wave radiation [102] and it has been used in several metamaterial-based leaky wave antennas operating in the microwave range [107]. The halved dimer-layer configuration in Fig. 2.5.8 is used to demonstrate backward nature of the field propagating along the $\pm x$ directions and to clearly show this we analyze the radiation by a halved dimer-layer configuration shown in Fig. 2.5.8.

The PC with a halved dimer-layer (PCHD) is very similar to the PCD except for the fact that dimer pairs for $x > 0$ are replaced by single rods. Therefore, the new configuration is the same with PC3 for $x > 0$. Surface and leaky waves are able to propagate only towards the $-x$ direction while PC3 will not allow propagation in the $+x$ direction. The experimental setup and the measured radiation patterns for a surface mode frequency (belonging to Case 2) and three separate frequencies (belonging to Case 3) are depicted together in Fig. 2.5.8.

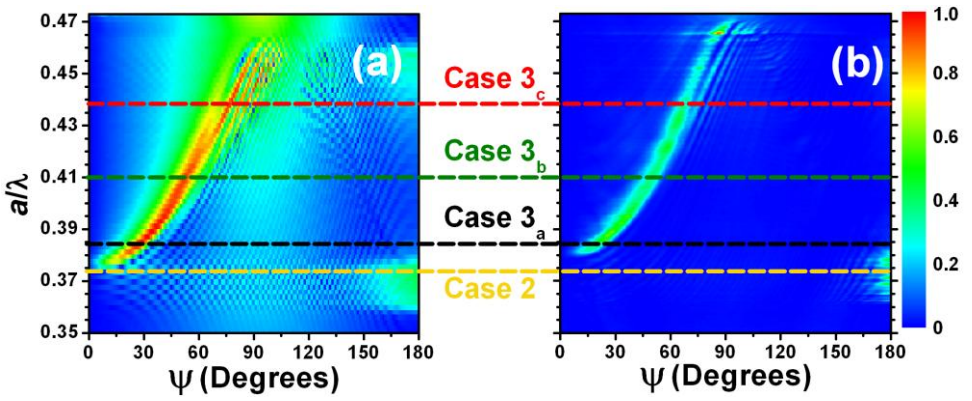

Figure 2.5.9. Radiation Graph for the Photonic Crystal with a halved dimer-layer. (a) Simulation of the field strength, (b) Experimental result for the transmission coefficient (yellow for Case 2, black, green and red for Case 3a,b,c). The cross sections that are indicated by black, green and red and yellow dashed lines are plotted in Fig. 2.5.8.

The corresponding RG for the PCHD is shown in Fig. 2.5.9. As it was stated for the PCD, no radiation is observed for **$0.294<a/\lambda<0.359$.** Accordingly, in the range **$0.359<a/\lambda<0.380$** the dimer-layer supports the surface mode. As a result, for **$a/\lambda=0.373$,** the radiation is observed only at $\psi = 180°$ whereas no significant field is measured near $\psi=0°$ or other angular directions. This is consistent with our earlier claims concerning Case 2. Maximum values of the RG's in Fig. 2.5.9 are normalized to 1, for comparison.

Finally, above the light line, at higher frequencies, we observe radiation only in the 1st quadrant while the leaky wave propagation takes place in $-x$ direction. We notice that as the frequency is increased, the radiation angle gets closer to 90° (broadside), which is the opposite of what happens to leaky wave working in the forward regime. These observations demonstrate the backward characteristics (i.e., opposite signs of phase and group velocities) of the radiation from the dimer-layer. They also confirm our prior understanding regarding the radiation phenomena for Case 3. It is also revealed that the effective aperture of PCHD (and PCD) is 0.5m (i.e., length of the dimer layer remaining at either side of the source) although the length of both structures is almost 1m.

2.5.3. Conclusion

By using a dielectric surface interface layer on top of a PC, guiding of surface waves and frequency dependent beaming with leaky waves is attained in the microwave regime. Since propagation at optical frequencies is subject to significant losses in the case of the metallic surface plasmons, dielectric PC may provide an alternative to obtain surface waves. Therefore, a dimer surface layer is utilized to support surface modes (i.e., guided modes confined in the top layer) on a PC for frequencies such that the propagation wavenumber lies below the light line. The results obtained by Rsoft Bandsolve Software which employs the Plane Wave Expansion method reveal the existence of the dimer-layer mode with a negative slope in the dispersion diagram implying the occurrence of phase and group velocities with opposite directions. Above the light line, this mode couples to the radiative spectrum. As a result, the photonic crystal with a dimer-layer (PCD) provides a symmetrical and directive radiation pattern with two radiation peaks at ψ and $(180°-\psi)$. The beaming angle ψ is adjustable as a function of frequency. In this manner, the PCD operates like a leaky wave antenna where each dimer contributes discretely to the radiated power. Although the experiments are carried out in the microwave regime, dielectric PC based structures offer scalability to optical frequencies. Angular distribution measurements are performed at a distance of 1m away from the source which is not far enough to satisfy the far field radiation condition. There is still a traceable correspondence between frequencies $0.38< a/\lambda < 0.44$ (11.88-13.75GHz) and measured radiation angles $0°< \psi < \sim 70°$ (simultaneously creating a symmetric beam in the 2^{nd} quadrant at an angle $180°-\psi$). At a larger measurement distance, in the far field, the symmetrical beaming angle is expected to extend beyond 70°, varying from 0° upto 90°. Another important aspect is that waves propagating along the dimer-layer cause radiation of

backward nature. We have assumed two propositions to relate this backward nature to the behavior of the part of the dispersion diagram, relative to the propagating mode, which would reside above the light line (we could determine only real propagation wavenumbers, below the light line): 1) Above the light line the surface mode has an imaginary part and it is responsible for the leaky behavior, 2) The slope of the (real part) of the propagation constant above the light line is still negative (i.e., implying negative group velocity). As a result, the radiation beam angle approaches from backfire to broadside when frequency increases (this is typical of backward leaky wave antennas used in the microwave regime). Experiments and simulations relative to the halved dimer-layer are then used to demonstrate the mentioned backward characteristics and to verify the above propositions. FDTD simulations performed by Rsoft Fullwave Software have accompanied experimental measurements and they are in good agreement, to conclusively support our propositions.

Chapter 3

Fishnet as a Metamaterial

3.1 The constitutive parameters

The source-free Maxwell Equations i.e., Eqn. (3.1) and Eqn. (3.2) together with the constitutive relations given in Eqn. (3.3) and Eqn (3.4),

$$\nabla \times \vec{E} = -\frac{\partial \vec{B}}{\partial t} \qquad (3.1)$$

$$\nabla \times \vec{H} = \frac{\partial \vec{D}}{\partial t} \qquad (3.2)$$

$$\vec{B} = \mu \vec{H} \qquad (3.3)$$

$$\vec{D} = \varepsilon \vec{E} \qquad (3.4)$$

reduce to Eqn. (3.5) and Eqn. (3.6) for the monochromatic time harmonic plane wave excitation:

$$\vec{k} \times \vec{E} = \sqrt{\frac{\mu}{\varepsilon}} \vec{H} \qquad (3.5)$$

$$\vec{k} \times \vec{H} = \sqrt{\frac{\varepsilon}{\mu}} \vec{E} \qquad (3.6)$$

For an isotropic medium, the wavevector can be expressed as

$$k^2 = \frac{\varpi^2}{c^2} \tag{3.7}$$

where the refractive index is obtained by the multiplication of relative permeability and relative permittivity, i.e., $n = \sqrt{\varepsilon_r \mu_r}$. These relations still hold when the sign of the constitutive parameters are both negative [13]. In the case of positive-valued constitutive parameters (μ and ε), a right-handed system is formed whereas when μ and ε are both negative-valued, the vector triplet obeys a left-handed representation. However, the instantaneous Poynting's vector (i.e., direction of the power flow) is not affected since the constitutive parameters have the same sign:

$$\vec{S} = \vec{E} \times \vec{H} \tag{3.8}$$

Thus, for positive μ and ε, the power flow and the direction of the phase vector are in the same direction and are away from the source generating the field. On the other hand, with negative-valued μ and ε, while the Poynting's vector still points away from the source, i.e., the power flows away from the source, the wave vector need not be in the same direction, that is, the phase propagation yields negative phase velocity. The propagating modes can naturally be seen in the materials which correspond to the first quadrant (i.e., $\mu > 0, \varepsilon > 0$), so called the Right Handed Medium. They can be observed for the Left Handed Medium which is expressed by the third quadrant of the $\mu - \varepsilon$ space (i.e., $\mu < 0, \varepsilon < 0$), as well (See Fig. 3.1.1). On the other hand, for $\mu - \varepsilon$ pair corresponding to the second and the fourth quadrants are accompanied with the evanescent modes.

3.2 Negative Permittivity (ε < 0)

Time dispersion is related to the dependence of permittivity on frequency. As an example, the permittivity of water decreases from $80\varepsilon_0$ to $1.8\varepsilon_0$ as frequency increases from static to optical regime. The reason for this drop is that the permanent dipole moments of the individual water molecules cannot align themselves rapidly enough with the rapidly varying fields at high frequencies. Another dispersive medium is plasma which is a neutral system of ionized gas which consists of free electrons and positive ions. The force acting on an electron is $\vec{f} = q(\vec{E} + \vec{v} \times \vec{B}) \approx q\vec{E}$ assuming v<<c where $q = 1.6x10^{-19} Coulomb$ and $\vec{E}, \vec{B}, v, c$ are the electric field intensity, magnetic field density, speed of the electron and speed of light in free space, respectively. From Newton's second law, with $e^{-i\varpi t}$ time harmonic convention,

$$q\vec{E} = m\vec{a} = d(m\vec{v})/dt = -i\varpi m\vec{v} \tag{3.9}$$

where $m = 9.1x10^{-31} kg$ is the mass of an electron. The volume current due to electrons is $J_p = nq\vec{v}$ with n being the volume electron density. Employing this equation together with Eqn. (3.9), one obtains,

$$J_p = \frac{nq^2\vec{E}}{-i\varpi m} \tag{3.10}$$

Inserting Eqn. (3.10) in Maxwell's equation where $\vec{J}_f$ represents the source term,

$$\nabla \times \vec{H} = -i\varpi\vec{D} + \vec{J}_p + \vec{J}_f \tag{3.11}$$

the complex permittivity is obtained,

$$\varepsilon(\varpi) = \varepsilon_0\left[1 - \frac{\varpi_p^2}{\varpi^2}\right] \tag{3.12}$$

where the plasma frequency is defined as

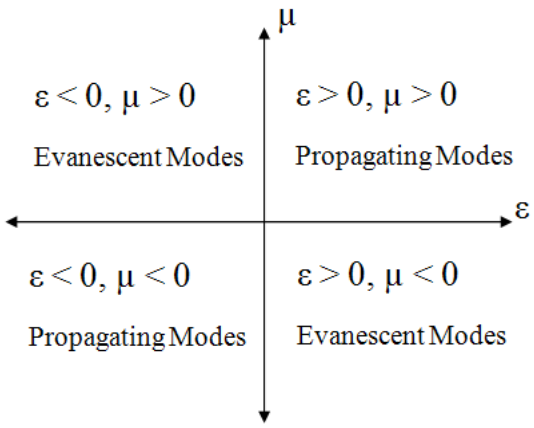

Figure 3.1.1. Mode propagation and the sign of the constitutive parameters.

$$\varpi_p = \sqrt{\frac{nq^2}{m\varepsilon_0}} \approx 56.4\sqrt{n} \tag{3.13}$$

It is seen in Eqn. (3.12) that the permittivity attains negative values below the plasma frequency. However, from Eq. (3.7), the propagation constant becomes imaginary and the resultant evanescent waves cannot propagate in the metal medium [17].

The negative permeability in the microwave regime can be achieved by periodically arranged metallic wires [17,117]. The plasma frequency for the arrangement is given by

$$\varpi_p = \frac{ne^2}{\varepsilon_0 m_{eff}} = \frac{2\pi c_0^2}{a^2 \ln(a/r)} \tag{3.14}$$

where c_0 is the speed of light in free space, a is the period of the lattice and r is the radius of the metallic rods.

The effective medium interpretation holds as long as $a << \lambda = 2\pi c_0 / w$ and the thin wire medium can be treated as a homogenous medium with an effective value of permittivity ε_{eff}. That is, as long as the radius of the thin wires is small in comparison to a, i.e., $\ln(r/a) << 1$, Bragg diffraction is avoided to come into the picture and the diffraction effects are seen only at very high frequencies.

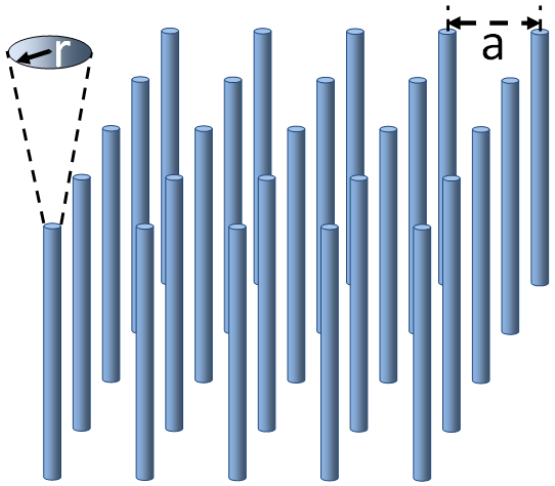

Figure 3.2.1: Thin metallic wires arranged with a lattice constant *a* and radius *r*.

3.3 Negative Permeability ($\mu < 0$) and Negative Refraction ($n<0$)

The existence of the electric charges causes the response of the materials to external electric field. Thus, negative permittivity values can be obtained below the plasma frequency. However, since there are no magnetic charges to react to the applied magnetic fields, negative permeability cannot be achieved in the natural materials, practically. The wire configuration which provides with negative permittivity does not respond to magnetic fields. This issue is overcome by the design of Pendry *et al*. [118]. In these designs capacitive and inductive Split Ring Resonators (SRRs) are used (Fig. 3.3.1(a)). The natural materials' magnetic response is enhanced to exhibit negative permeability in a certain band of frequency.

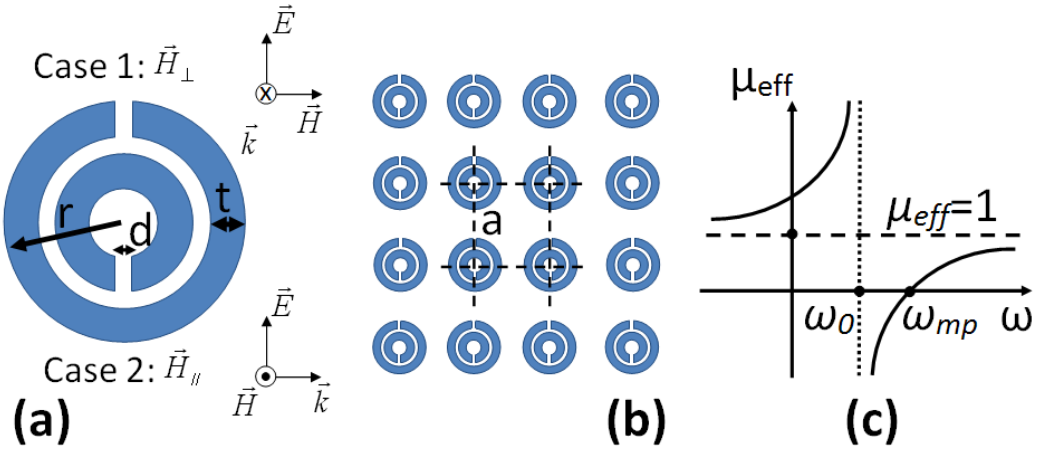

Figure 3.3.1. (a) Single SRR, Case 1 for $\vec{H}_{\perp}$, Case 2 for $\vec{H}_{//}$, (b) Periodically arranged SRRs, (c) The effective permeability of the periodically arranged SRRs.

Pendry *et al*. showed that the SRRs' resonance wavelength is much larger than the period *a* of the SRRs [118]. Thus, the SRR structure can be treated as an isotropic medium. The oppositely oriented two rings provide with a large capacitance, which enables the current flow on the metallic rings and yields to the resonant behavior due to the arisen capacitance:

Defining $F = \pi r^2 / a^2$ as the fractional volume (filling factor) of the cell and the capacitance per unit area $C = \frac{\varepsilon_0}{d} = \frac{1}{dc_0^2 \mu_0}$, the effective permeability is obtained as [118]:

$$\mu_{eff} = 1 - \frac{F}{1 + \frac{2\sigma i}{\varpi r \mu_0} - \frac{3}{\pi^2 \mu_0 \varpi^2 C r^3}} = 1 - \frac{\frac{\pi r^2}{a^2}}{1 + \frac{2\sigma i}{\varpi r \mu_0} - \frac{3dc_0^2 \mu_0}{\pi^2 \mu_0 \varpi^2 r^3}} \tag{3.15}$$

The pole of μ_{eff} is given as

$$\varpi_0 = \sqrt{\frac{3}{\pi^2 \mu_0 C r^3}} = \sqrt{\frac{3dc_0^2}{\pi^2 r^3}} \tag{3.16}$$

and the magnetic plasma frequency is

$$\varpi_{mp} = \sqrt{\frac{3}{\pi^2 \mu_0 C r^3 (1-F)}} = \sqrt{\frac{3dc_0^2}{\pi^2 r^3 (1-\frac{\pi r^2}{a^2})}} \qquad (3.17)$$

which is equivalent to say $\frac{\varpi_0}{\sqrt{(1-F)}} = \varpi_{mp}$.

Investigating Fig. 3.3.1(c), from lower frequencies towards higher frequencies, μ_{eff} permits propagating modes upto ϖ_0. In the vicinity of ϖ_0, it diverges to positive infinity and beyond ϖ_0 it abruptly jumps to negative infinity. Between ϖ_0 and ϖ_{mp}, the negative permeability values are accompanied with evanescent modes and no propagation is observed. The width of this band is determined by the filling factor F. Beyond ϖ_{mp}, μ_{eff} rises towards unity.

The relation of the propagation and the polarization of the incident wave is studied in [15] by examining the stop bands and the sign of μ_{eff}. The two possible configurations for the incident field are depicted in Fig. 3.3.1(a). In the first case, magnetic field $\vec{H}$ is vertical to the SRR surface normal and it is notated by $\vec{H}_{\perp}$ while in the second case $\vec{H}_{//}$ is along the SRR surface normal. In both cases, electric field $\vec{E}$ is parallel to the SRR surface. For both polarizations there occur bandgaps for propagation, nevertheless μ_{eff} is not trivially negative and whether the bandgap arises due to negative μ_{eff} or negative ε_{eff} should be examined. It is possible to estimate the origin of the bandgap and the existence of negative μ_{eff} or ε_{eff} by varying the dielectric function and the scattering mechanisms in the structure [15, 119]. Smith *et al.* showed that for $\vec{H}_{//}$, the magnetic field is coupled to the SRR structures and negative value for μ_{eff} is attained over a moderate band. However for the $\vec{H}_{\perp}$ case, μ_{eff} possesses a slowly varying small-valued function and which does not produce negative values [15].

Considering one dimensional wave equation,

$$\frac{\partial^2 E}{\partial x^2} = \mu\varepsilon \frac{\partial^2 E}{\partial t^2} \tag{3.18}$$

the solution is in the form of $\exp(i(nk_0 x - wt))$ where $n = \sqrt{\mu_r \varepsilon_r}$ and $k_0 = \varpi / c_0$. The propagating modes exist for real n where μ_{eff} and ε_{eff} are both +ve or are both –ve. Without losing the generality, the parallel polarization case (i.e., the electric field component is in the plane of propagation) is examined in Fig. 3.3.2 and the reflected and the possible directions of the refracted wave are depicted. The discussion can be extended to the perpendicular polarization (i.e., the electric field is in the direction of the normal of the plane of propagation). Medium 1 is defined to have positive μ_{eff} and ε_{eff} and the incident beam is depicted in Region II. The reflected field propagates in Region I. The transmitted wave is negatively refracted towards Region III if both μ_{eff} and ε_{eff} are negative in Medium 2. If the constitutional parameters are both positive in Medium 2 then positively refracted beam is observed as in Region IV. The reasoning comes from the boundary conditions for the tangential ($_t$) and normal ($_n$) components:

$$E_{t1} = E_{t2} \qquad H_{t1} = H_{t2} \tag{3.19}$$

$$\varepsilon_1 E_{nt1} = \varepsilon_2 E_{n2} \qquad \mu_1 H_{nt1} = \mu_2 H_{n2}$$

Considering μ_{eff} and ε_{eff} are negative in Medium 2, the tangential components are preserved whereas opposite directions are valid for the field components in comparison from Medium 1 to Medium 2. Assuming a material with $\varepsilon_r = \mu_r = -1$, one can write $\varepsilon_r = \exp(i\pi)$ and $\mu_r = \exp(i\pi)$ then $n = \sqrt{\mu_r \varepsilon_r} = \exp(i\pi/2) \cdot \exp(i\pi/2) = -1$ whereas $\mathrm{Re}\{\eta\} = \mathrm{Re}\{\sqrt{\mu_r / \varepsilon_r}\} > 0$ for a passive medium [13]. Besides, what is to keep in mind is that to achieve a passive material the square root of either ε or μ alone must have a positive imaginary part,

[120]. From Eq. (3.5) and Eq. (3.6), the *z*-component of the wave vector ($\vec{k}_t^{\,-}$) is also reversed since $\sqrt{\frac{\mu_{eff,2}}{\varepsilon_{eff,2}}}$ produces a negative sign (both μ_{eff} and ε_{eff} are negative in Medium 2). However, for an isotropic medium, from Eq. (3.8) the Poynting vector which is related to the power flow is oppositely directed wrt to the wave vector. For anisotropic media, the angle between phase and group velocities is not necessarily 180°. But, the situation in Region III of Fig. 3.3.2 represents the picture for refraction, the flow of power and phase propagation in a general way. The refraction angle θ_t obeys the Snell's law: $n_1\sin(\theta_i) = n_2\sin(\theta_t)$. Thus, in comparison to a right-handed medium (Region IV), for the left-handed medium (Region III) the refraction angle θ_t is equal in magnitude to that of Region IV. Only difference is that θ_t has a negative sign.

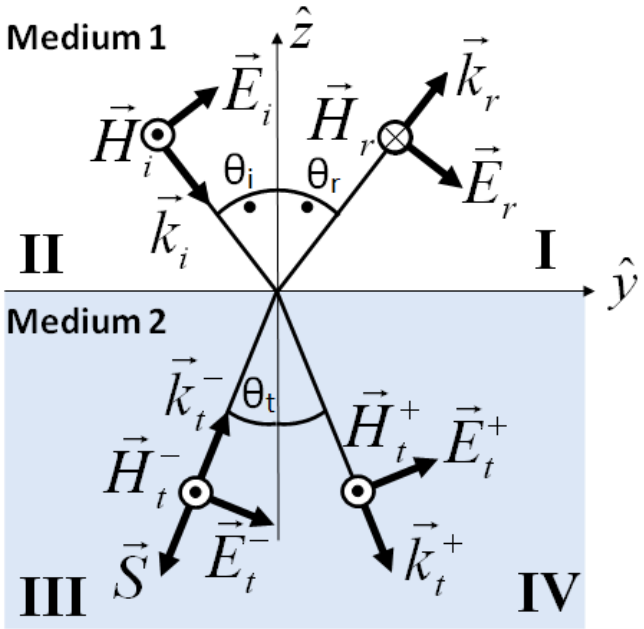

Figure 3.3.2. Reflection in Region I, positive refraction in Region IV for positive μ-ε and negative refraction in Region III for negative μ-ε.

Smith *et al.* investigated the dissipated power during propagation in the case of $n<0$ [121]. The work done on the fields is given as:

$$\mathrm{P} = \Omega W = -\frac{1}{2}\int_V j^* E(x,\Omega)dx = \pi \frac{\mu}{cn} j_0^2 \tag{3.20}$$

For physical waves which also satisfy causality, the work done (W) should be positive. This is satisfied in the right-handed medium as both n and μ are positive. In addition, for the case of $n<0$ and $\mu<0$, W turns out to be positive, as well. As a result, the waves propagate away from the source, which is in agreement with the causality and Veselago's proposals [13].

3.4 Left-Handed Behavior in Fishnet Metamaterial

3.4.1 Introduction

After reviewing the basics of metamaterials, in the rest of the thesis we will be examining the theoretical and experimental aspects of fishnet metamaterial. The results that will be mentioned will rely mainly on [117]. The multimedia files are also avaliable for [117].

When a beam is incident from a Right Handed (RH) medium onto a slab of a LH medium, the transmitted light is refracted towards the same half space as the incident wave with respect to the surface normal. This is a result of the NRI associated with the LH medium. Consequently, the propagating modes are focused at the exit of the LH medium [14]. Moreover, the evanescent modes in the direction of propagation are recovered by the NRI material. In other words, the propagating modes experience a phase correction as in a conventional lens

and the evanescent modes are enhanced in amplitude [123]. Thus, a resolution beyond the diffraction limit can be achieved for a restricted range of parameters [124,125].

The bandwidth of the negative refraction is limited by the frequency span of the magnetic resonance achieved by the SRRs. Conversely, Transmission Line (TL) based NRI materials are offered [126] and they have been demonstrated to provide increased bandwidth [127]. TL is constructed planary and is loaded with lumped L-C elements, where the constitutive parameters are both negative for a certain bandwidth generating a backward-wave radiation [128,129]. Alternatively, a structure with the increased bandwidth of NRI employs Ω-shaped rings in the microwave regime, while reducing the transmission losses [130]. Another experimental demonstration of the NRI and negative phase velocity in the microwave regime is given in [131].

Targeting operation frequencies beyond the infrared regime by means of scaling down the dimensions of the SRRs is not practical, because the SRRs' magnetic response saturates and deviates from that of an ideal conductor as dimensions get smaller [132]. In order to overcome both the magnetic saturation and the problems related to the manufacturing of the SRRs in nanoscale, pairs of metallic wires [133] and dielectric slabs with perforated metallic layers on both surfaces are proposed [134]. The anti-parallel currents in the metallic layer pairs and opposite charges accumulating in the corresponding ends create the magnetic response ($\mu_{eff} < 0$). In these designs, the electric response ($\varepsilon_{eff} < 0$) was still evident as a result of the electromagnetic interactions between the neighboring wires. In both of the referred studies the operational frequency corresponds to the infrared region while research carried out in the microwave regime also exist [135,136]. The introduction of the cut wire pairs to the field relieved a portion of the difficulties in fabrication. Yet, the cut wire pairs were electrically large and it turned out to be very challenging to sustain a double

negative response out of these configurations in the absence of the additional geometries.

Consequently, in search for alternative designs the approaches employing dielectric slabs and metallic wires are modified and improved to yield the fishnet structure. Double fishnet structures patterned with gold were shown to exhibit negative phase and group velocities at the same time [137]. The losses were reduced and the negative refraction at 780 nm is obtained by using a silver fishnet pattern [138]. Fishnet metamaterials operate for both polarizations due to their symmetry as shown in the work by Kafesaki *et al*. who carried out the investigation in the microwave regime for different variations of the fishnet geometry [139].

One of the main advantages of the fishnet structures compared to the SRR is its ability to produce a magnetic response for the normal incidence. In this manner, the incident H-field is coupled through the parallel metallic plates. As a result, it provides a resonant magnetic response analogous to that of the SRR, associated with strong anti-parallel currents on both metallic faces of the same fishnet layer [140]. Thus, a strong LH response with only one slab layer is possible. Besides, fishnet geometry enables planar manufacturing. This simplicity is advantageous at the manufacturing step, in contrast to the SRR case. As a result of the LH behaviour, the negative phase advance is seen in the fishnet configurations [141]. The fishnet structure led to the currently lower-loss high-frequency LH materials over a wide range of structural parameters [142]. Hence, optical applications have been made possible [143,144].

The section is organized to include two main discussion parts. We have worked both with individual fishnet patterned dielectric layers and a wedge-shaped structure that is obtained by employing the same type of fishnet layers in the microwave regime. In the first part, we conduct the transmission and reflection studies for the fishnet stacks to understand the wave propagation inside such structures and to attain the retrieval parameters which we later

compare with the outputs from the wedge study. In addition, the first part of the section also covers the examination of the fishnet arrangement, which aims to shed light on the ongoing debates concerning the elucidation of the physical mechanisms of the fishnet configurations. In this part, we have adapted the models offered in the literature to our own design and inspected the validity of the proposed models both numerically and experimentally. In order to capture a complete picture of the underlying physics the different perspectives in the debates have been borrowed. The second part of the present section concentrates on the wedge configuration. We have investigated the negative refraction in the wedge structure, which is the typical experimental method used for the observation of the LH properties in composite metamaterials [18,145,146]. Despite the realizations at optical wavelengths and quasi-optical regimes [143,147], the present work parametrically investigates the validity of the homogenization and the prism effects for the first time with the wedge experiments in the microwave domain. In our work, the complete picture of the transmission through the wedge structures is aimed to be discussed by considering the electromagnetic response of the fundamental building blocks of the relevant wedge configuration. In this manner, the extent of the stringent implications of the fundamental block's electromagnetic response on the validity of the homogenization of the wedge arrangements is going to be opened to discussion with a parametrical analysis. Simulations are performed to observe the LH behaviour as a result of the phase reversal in the NIM [146,148,149]. Two dimensional (2D) scan measurements are provided to compare the NRI value with those apparent in the 2D scan simulations. These quantities are compared with the retrieved NRI for the fishnet layers. The effect of the periodicity (a_s) along the direction of propagation on the refractive power and transmission is studied. Thus, the convergence of the NRI values with the changing unit cell size and layer number is inspected. The section is concluded by comparing the quantities and discussing the validity of the NRI values

extracted from the experimental and numerical results both for the retrieval analyses and wedge studies.

3.4.2 The analysis of the fishnet structure

Teflon boards with double-sided PCBs are patterned in the metallic fishnet form with mirror symmetry on both faces [(see figure 3.4.1(a)]. Periodicities along *i*- and *y*-axes are equal ($a_i = a_y = 14$ mm). The metallic strips of the fishnet are $w_i = w_y = 7$ mm wide along *i*- and *y*-directions, respectively. Thus, the fishnet is symmetric on the 2D surface plane. The height of the boards is $9a_y$ (126 mm). The thickness of the metal is 20 μm. The thickness of the dielectric Teflon substrate is 1 mm. The permittivity of the Teflon board is taken as $\varepsilon = 2.16$ and the tangent loss (δ) is 0.005.

The wedge structure is developed by stacking the Teflon boards, as shown in figure 3.4.1(b). Each Teflon layer placed in front of the other is a period (a_i) shorter than the previous one. The longer side of the prism is $20a_i$, which corresponds to the width of the wedge. The distance a_s is the period of the fishnet layers along the incident surface normal. The thickest region of the wedge parallel to the incident surface normal is $19a_s$,. Then, the wedge angle is obtained as $\theta_w = \tan^{-1}\left(19a_s / 19a_i\right)$. Geometrically, θ_i which is the incident angle for the outgoing surface [see figure 3.4.1(f)] is equal to θ_w Calculation of the wedge angle gives 8.1°, 12°, 15.9°, 19.7° when a_s is set to 2 mm, 3 mm, 4 mm and 5 mm, respectively. Then, a_s values (2 mm to 5 mm) correspond to $\lambda/10.5$, $\lambda/7.0$, $\lambda/5.2$ and $\lambda/4.2$ at 14.3 GHz.

We have carried out the 2D *XY*-scan experiments with the help of a stepper-motor-driven robot which is controlled by the computer [see figure 3.4.1(e)]. The S_{21} measurements are performed with a HP8720B network analyzer. The

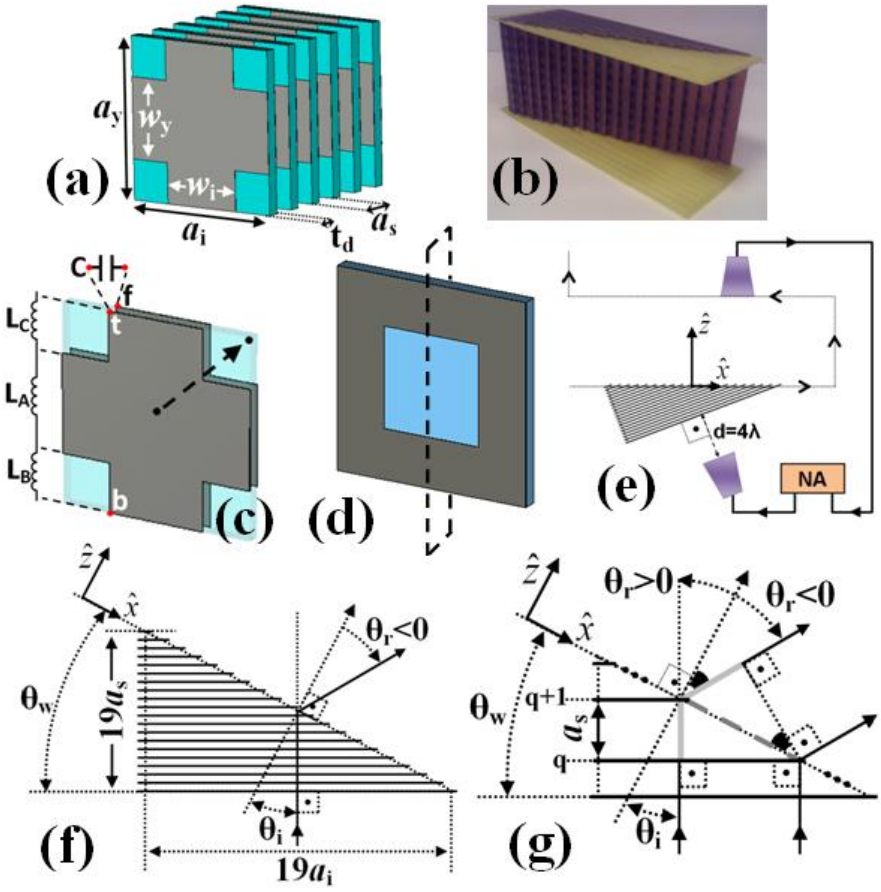

Figure 3.4.1. (Colour Online) (a) Stacked six periods of fishnet structure, (b) The wedge arrangement formed with the help of a yellow-coloured frame which is made of thin FR4 material. (c) The double metallic layer configuration of the fishnet cell and the inductance and capacitance values attributed to the related sections of the unit cell, (d) another unit cell representation which is possible when the unit cell centre in figure 3.4.1(c) is shifted from the point at the centre to the point at the corner along the direction of the dashed arrow, (e) the experimental setup. The wedge structure, the Network Analyzer (NA) and the horn antennae are illustrated with the 2D scanning scheme, (f) the geometric definitions related to the wedge structure. θ_r is the refraction angle that the outgoing beam makes with the exit surface normal, (g) definitions of the parameters used for the diffraction analysis for the q^{th} and $(q+1)^{th}$ layer of the wedge structure.

transmitter and the receiver horn antennae can operate in the 12-18 GHZ range. The *E*-field of the radiated signal is parallel to *y*-axis where *H*-field is on the transverse plane.

3.4.2.1 *Modelling the fishnet configuration as an LC tank*

One of the earliest approaches to analyze the principles of the wave propagation inside the fishnet configurations was developed in [139] and the supporting circuit models were presented in [142]. In the regarding studies, the fishnet structure was considered as a metamaterial with two bands of operation which constitute namely the LH and RH bands. The fishnet geometry is treated as a metal-deposited plus sign [see figure 3.4.1(c)] both in [139] and [142]. Alternatively, the fishnet can also be considered as a subwavelength aperture staying loyal to the Bloch restrictions on the unit cell, as in the case of figure 3.4.1(d). Both of these perspectives will be interchangeably used in the proceeding sections. Accordingly, the surface current distribution of the double-sided fishnet layer with the aforementioned geometrical parameters is shown in figure 3.4.2 for both the LH and the RH regimes. CST Microwave Studio has been used in our simulations, which utilizes Finite Integration Technique. In figure 3.4.2(a), the current direction on one surface is observed to be opposite to that of the currents flowing on the other surface of the same layer. Thus, an inductance L is attributed to this pair of currents in opposite directions where a current loop is formed [139]. On the other hand, the current directions are seen to be the same in the RH regime [see figure 3.4.2(b)].

In figure 3.4.3, the electric and magnetic field components are provided for 5 cascaded fishnet layers where $a_s = 4$ mm. The cross sections are given for the cascaded subwavelength apertures residing at the centre of each layer [see figure 3.4.1(d)]. Since E_x and H-field components different than H_x turn out to be very small in magnitude compared to the other components of the propagating beam, they are not depicted. On the other hand, in both of the LH and RH bands a strong electric field is pronounced in y-direction [see figure 3.4.3(a) and 3.4. (b)]. This component is attributed to the capacitive effect along the aperture. As for the z-component of the E-field, E_z is seen to be strongly localized between the metal layered surfaces of the dielectric slab for the LH band [see figure

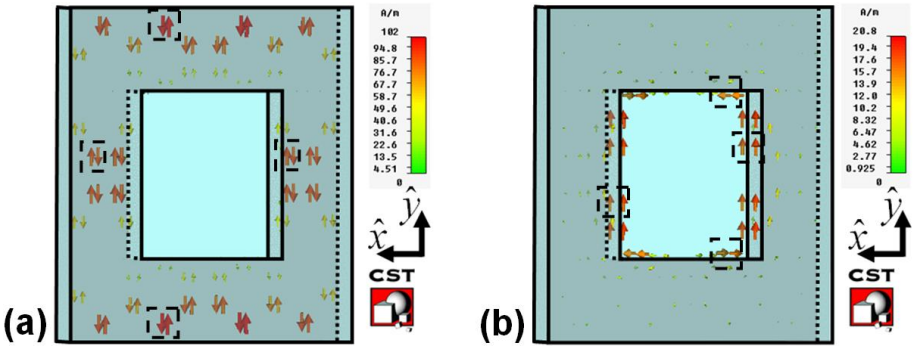

Figure 3.4.2. (Colour Online) (a) The current distribution in the LH band at 14.20 GHz (media 1 of ref. 117) and (b) the current distribution in the RH band at 17.4 GHz (media 2 of ref. 117). The current directions on both of the surfaces of the fishnet layer are indicated in dashed boxes. The arrow on the left shows the current direction on the back surface and the arrow on the right shows the current direction on the front surface of the fishnet layer. The propagation direction is along the $\hat{z}$ -direction, which is through the aperture.

3.4.3(c)]. This situation indicates the existence of the capacitive effect between the metallic surfaces of a layer along the direction of the wave propagation. In contrast to case of the LH band, E_z reveals itself only as a byproduct of the diffractions at the edges of the subwavelength aperture at the RH band [see figure 3.4.3(d)]. The strong magnetic field is concentrated inside the dielectric slab for the LH band [see figure 3.4.3(e)]. This magnetic field can be interpreted as the field which induces the circulating currents (the anti-parallel currents) illustrated in figure 3.4.2(a). Thus, an inductive effect is asserted in the LH band associated with the metallic parts, i.e., wires of the fishnet. This is not the case for the RH band. Specifically, H_x is not as strong as it is in the LH band [compare figure 3.4.3(e) and 3.4. (f)] and the surface currents are not in opposite directions in the RH band [see figure 3.4.2(b)].

Then, the fishnet configuration is subject to different *LC* formations for LH and RH bands owing to distinct physical mechanisms, which will determine the magnetic and electric resonances, respectively. The relevant *LC* elements are depicted in figure 3.4.1(c) for the LH band. The Bloch conditions of the unit cells of the fishnet structure dictate the voltage distribution to be periodic. As a

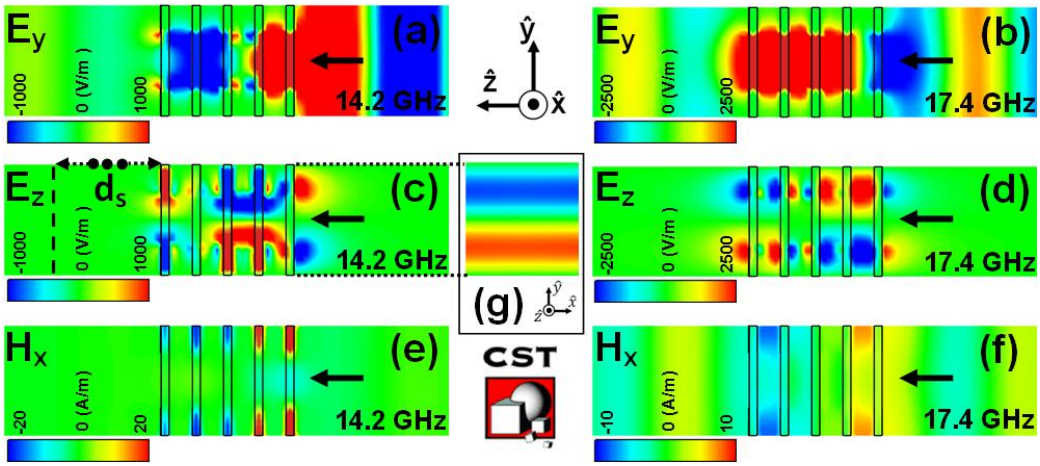

Figure 3.4.3. (Colour Online) The field components for the LH band (14.2 GHz) and the RH band (17.4 Ghz) for a five layers of fishnet arrangement with $a_s = 4$ mm, (a) E_y component of the electric field at the LH band (media 3 of ref. 117), (b) E_y component of the electric field at the RH band (media 4 of ref. 117), (c) E_z component of the electric field at the LH band (media 5 of ref. 117), (d) E_z component of the electric field at the RH band (media 6 of ref. 117), (e) H_x component of the magnetic field at the LH band (media 7 of ref. 117), (f) H_x component of the magnetic field at the RH band (media 8 of ref. 117). The remaining field components are negligibly small. (g) (Inset at the centre) E_z component of the electric field at the LH band on the *xy*-plane. The cross sectional field component is sketched at a distance $d_s = 15.5$ mm away from the exit side of the stacked fishnet plates, as shown in figure 3.4.3(c).

result, the line segment (along a_i) that passes through point *t* at the top of the unit cell in figure 3.4.1(c) can be considered to be electrically short circuited to the line segment (along a_i) passing through point *b* at the bottom of the unit cell. Then, the inductances L_B and L_C which are shown in figure 3.4.1(c) are series to each other. Moreover, because of the symmetry of the unit cell, $L_B = L_C$. Following the discussion in [139], the total inductance happens to be the combination of two parallel inductances, i.e., $L \sim L_A // (L_B + L_C)$. The values of the individual inductances can be approximated as the corresponding total area of the solenoid divided by the width of solenoid:

$$L_A \sim \frac{w_y t_d}{a_i}, \quad L_B = L_C \sim \frac{l_{B,C} t_d}{w_i}, \tag{3.21}$$

where $l_{B,C} = (a_y - w_y)/2$. The dominant electric field component for the LH band (E_z) will bring a capacitance between the parallel metallic patterns while the field is localized inside the dielectric slab. This capacitance can be approximated by $C \sim (3/4)\varepsilon a_i a_y / t_d$. The accompanying capacitance can be considered as the stray capacitance of the inductors and the total arrangement will yield a magnetic resonance frequency in the following form:

$$f_m = \frac{1}{2\pi\sqrt{LC}} \sim \sqrt{\frac{1}{3/4\,\varepsilon}\left(\frac{1}{a_y w_y} + \frac{w_i}{2a_i a_y l_{B,C}}\right)}. \quad (3.22)$$

The magnetic resonance was reported to be around 21 GHz in [140] for the fishnet structure with the following parameters $a_i = a_y = 10$ mm, $w_i = w_y = 2l_{B,C} = 5$ mm and $\varepsilon = 1.94$. Again, the magnetic resonance was found to be around 13 GHz in [139]. Assuming that the proportionality in Eq. (2) holds, the envisaged a magnetic resonance turns out to be 13.1 GHz for the design with $a_i = 7$ mm, $a_y = 9.5$ mm, $w_i = 1.5$ mm, $w_y = 7$ mm, $2l_{B,C} = 2.5$ mm and $\varepsilon = 4$. Thus, this simple LC tank modeling of the fishnet configuration roughly estimates the location of the magnetic resonance for a variety of the design parameters based on the physical interpretation of the induced surface currents and field components. Equation (2) predicts the magnetic resonance frequency as 14.22 GHz for our own study with the given dimensions ($a_i = a_y = 14$ mm, $w_i = w_y = 2l_{B,C} = 7$, $\varepsilon = 2.16$). This point will be revisited in the subsequent discussions once the transmission results are given.

Similarly, the LC tank modeling is also valid for the electrical resonance. Unlike the circulating surface currents in the LH band, the inductance is caused by the induced surface currents on the straight wires around the subwavelength opening [see figure 3.4.2(b)]. The dominant component of the electric field (E_y) results in a capacitive formation along the plane of the aperture for the RH regime [see figure 3.4.3(b)]. Therefore, merely the examination of the fields and

surface currents gives away clues about the transmission spectrum of the fishnet design. A LH band will be centreed around the magnetic resonance frequency, which will be followed by a RH band extending up to the electrical resonance frequency, as in the case of the conventional metamaterials.

3.4.2.2 *The transmission Results*

The simulated transmission spectrum for the considered single-layer fishnet configuration is plotted in figure 3.4.4(b) (solid blue line). The unit lattice shown in figure 3.4.2 has been utilized during the transmission simulations. Tangential components of the electric and magnetic fields are set to zero at the *x*-*z* (top and bottom walls) and *y*-*z* (side walls) planes of the unit cell boundaries, respectively, which implies the periodic boundary conditions because of the symmetric nature of the fishnet geometry. The overall features of the transmission spectrum do not strike us. In accordance with the predictions of the previous analysis in Sec. 2.1, the LH transmission peak is located at 14.21 GHz. There are two major bands of operation. Then, a circuit model has been developed in order to characterize the transmission spectrum of the single fishnet layer [see figure 3.4.4(a)]. A similar model had been proposed in [150]. The fishnet is represented with two *RLC* filters as a discontinuity surrounded by the TLs. The TLs stand for the vacuum blocks between the fishnet geometry and the transmitter/receiver along the direction of propagation. The inductors at the discontinuity are accompanied with the resistors to account for the losses. The values of the circuit elements are tabulated in table 3.4.1. Pursuing a similar treatment that is given in [150], the *RLC* values are found out by applying a fitting procedure. Once the values of the circuit elements are known, S_{21} is plotted for the LH (red dashed line) and RH bands (green dotted line). It is observed that the transmission spectrum can be expressed with *RLC* elements at microwave frequencies as it was argued in [150] for the optical counterparts.

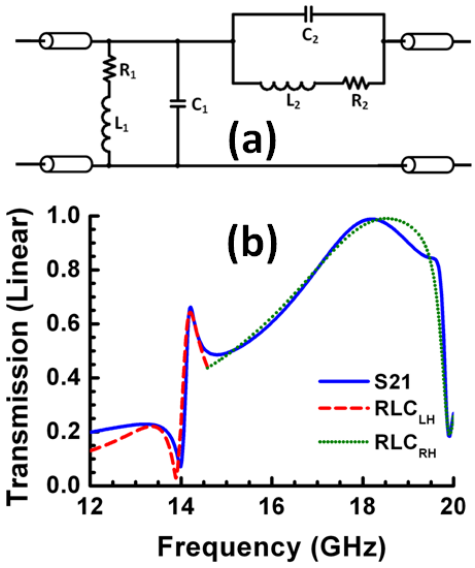

Figure 3.4.4. (Colour Online) (a) The TL model and (b) the transmission spectrum of the fishnet configuration for 1 layer. The simulation results are plotted in solid blue whereas the *RLC* model in (a) yields red-dashed and green-dotted lines at LH and RH bands, respectively.

The transmission measurements for two and five layers of fishnet NIM are given in figure 3.4.5 for varying a_s values. Each fishnet layer had a width and a height of $20a_i$ and $9a_y$ along *x*- and *y*-axes, respectively. The regarding sizes of the fishnet layers were chosen to be equal or more than 6λ at 14.3 GHz. This enables the assumption of the periodic boundary conditions to be valid when the central area of the fishnet layer that is aligned with respect to the antennas is illuminated with a finite beam width. Likewise, the fishnet layers are placed within the near-field region of the transmitting and receiving antennas in order to avoid both the divergence of the incoming excitation beam and the resulting diffraction mechanisms at the edges of the fishnet layers. The transmission results are calculated for a higher frequency resolution in contrast to the previously discussed case in figure 3.4.4(b) for the corresponding a_s values. The LH band around 14.2 GHz is apparent in the transmission results. The transmission peak frequencies taken from figure 3.4.5 are tabulated in table 3.4.2. In addition, the LH transmission peak frequency is also recalculated with

the new frequency resolution settings for the single layer case with the aim of making a fair comparison and it is found to be at 14.18 GHz. The numerical and experimental results are in agreement and consistent with the values reported in [141].

	LH ($f \sim 14.25$ GHz)	RH ($f > 15$ GHz)
R_1 (Ω)	0.001	0.010
L_1 (pH)	100	374
C_1(fF)	1260	201.240
R_2 (Ω)	0.100	0.100
L_2 (pH)	404	106.530
C_2 (fF)	325	600

Table 3.4.1. Circuit parameters for the LH and RH Bands.

The first remark we have to make is the coupling mechanism between the stacked layers. The coupling is more pronounced and it strongly modifies the exact location of the magnetic resonance and thereby the LH transmission peak as the layer to layer separation gets smaller. Consequently, the LH transmission peak is observed within a frequency band of 14.18 GHz-14.21 GHz and 14.22 GHz-14-27 GHz in the simulations and the experiments, respectively, for $a_s = 2$ mm. As for $a_s = 5$ mm, the transmission peak varies in the 14.18 GHz-14.30 GHz band and in the 14.24 GHz-14.36 GHz band for the simulations and the experiments, respectively. It is not coincidental to observe that the LH transmission peak is closest to the peak noticed in the isolated fishnet (1-layer) transmission results. In other words, the coupling mechanism between the layers is degraded by setting $a_s = 5$ mm and the LH peak is spotted at a value closer to the one calculated for a single layer. Shen *et al.* also observed such a blue shift

in the LH transmission peak in [142] while the unit cell separation along the propagation constant shrinks. This mechanism will be very crucial for the interpretation of the results related to the wedge configuration. The shift is attributed to the decrease of the total flux passing through each resonator owing to the increased interactions of the unit cells along the propagation direction for decreased values of a_s. Furthermore, the LH transmission band gets narrower whilst a_s is increased from 2 mm to 5 mm, again owing to the weakened coupling between the layers. The other aspect of the coupling mechanism is the enhanced transmission following the LH band with the decreasing a_s values. The valley between the LH and RH bands tends to disappear due to a better impedance matching. After all, the transmission is the highest in the limiting case between the LH and RH bands and the two bands more or less merge when the metallic patterns on the layer surfaces are in contact by setting $a_s = 1$ mm (not shown here). For the limiting case, a subwavelength waveguide is formed leaving out the volume dedicated to the vacuum spacing between the layers. Particularly, this case will not be studied in this work. It will be shown in the proceeding sections that a lattice spacing smaller than a certain value is not suitable for wedge configurations. The plasma frequency which is designated as the beginning of the RH band is inclined to vary with a_s. This effect is associated with the change in the average metal density in the unit cell volume.

The losses come into play as the number of layers is increased. The coupling mechanism between the layers brings in immunity against the losses at a certain degree. Then, the influence of the losses is the most evident when we compare the two cases depicted in figure 3.4.5(d) and 3.4.5(h). The losses are largely caused by the substrate losses since E_z is mainly localized inside the substrate between the plates in figure 3.4.3(c). Ideally, the characteristic features of a metamaterial should not be dependent on the addition of extra layers. Yet, we witness a slight change in the magnetic resonance frequency based on the simulation results, which was earlier reported in [141], as well. Nevertheless, we

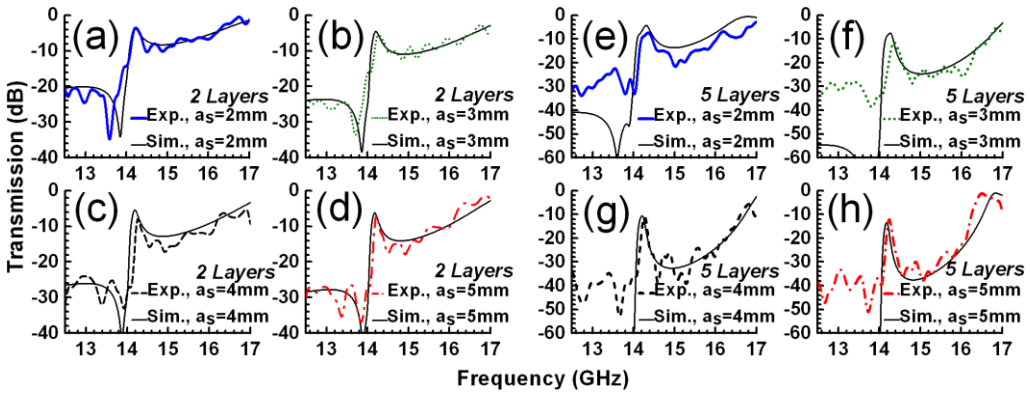

Figure 3.4.5. (Colour Online) Transmission (S_{21}) values for (a) 2 layers of fishnet with $a_s = 2$ mm, (b) 2 layers of fishnet with $a_s = 3$ mm, (c) 2 layers of fishnet with $a_s = 4$ mm, (d) 2 layers of fishnet with $a_s = 5$ mm, (e) 5 layers of fishnet with $a_s = 2$ mm, (f) 5 layers of fishnet with $a_s = 3$ mm, (g) 5 layers of fishnet with $a_s = 4$ mm, (h) 5 layers of fishnet with $a_s = 5$ mm.

# of layers	a_s	Simulation		Experiment	
2 layers	2 mm	-3.53 *dB*	14.21 GHz	-3.57 *dB*	14.23 GHz
	3 mm	-4.50 *dB*	14.20 GHz	-5.47 *dB*	14.27 GHz
	4 mm	-5.42 *dB*	14.19 GHz	-7.92 *dB*	14.27 GHz
	5 mm	-6.21 *dB*	14.18 GHz	-7.09 *dB*	14.22 GHz
5 layers	2 mm	-4.24 *dB*	14.30 GHz	-7.33 *dB*	14.36 GHz
	3 mm	-7.46 *dB*	14.26 GHz	-11.44 *dB*	14.35 GHz
	4 mm	-10.62 *dB*	14.21 GHz	-11.04 *dB*	14.27 GHz
	5 mm	-13.48 *dB*	14.18 GHz	-12.13 *dB*	14.24 GHz

Table 3.4.2. Transmission peaks for 2 and 5 layers when a_s=2, 3, 4 and 5 mm.

should bear in mind that these slight changes do saturate for higher number of layers according to the simulation results (not shown here).

In general, the overall numerical results are in good agreement with the experimental results apart from the slight mismatches in the measured transmission values and the frequency shifts. The major mismatch in the transmission results is below 14 GHz. The main cause of the discrepancy is the diffractions from the edges. Similar problems below the magnetic resonance had also been encountered in [141] and [142]. Periodic boundary conditions had been assumed in the calculations. Moreover, the transmission spectrum of the fishnet layers is very susceptible to the angle of incidence as it is reported in [151-153]. It was shown both experimentally and numerically in those regarding studies that even a shift of 2 degrees in the incident angle resulted in significant changes in the transmission spectrum. The exact location of the LH band in the frequency domain turned out to be very sensitive to the angle of orientation of the fishnet structure with respect to the source. Subsequently, non-idealities in the measurements arise from the unintentional misalignments which can produce an angle of incidence as high as 1 degree in our experiments. Additionally, the alignment of the stacked layers amongst each other is handled manually, which makes the measurements liable to minor errors. In the end, we should also consider the discrepancies and slight changes between the modeled excitation source and the employed antennas together with the utilized material parameters in the simulations and the manufactured fishnet layers.

3.4.2.3 *The Retrieval Analysis*

The retrieval analysis has been commonly employed in several studies in order to estimate the effective refractive index of the examined structures [138,141,147,151,154]. A retrieval analysis that is similar to the ones in [155] is performed to obtain the effective permittivity and permeability of the fishnet

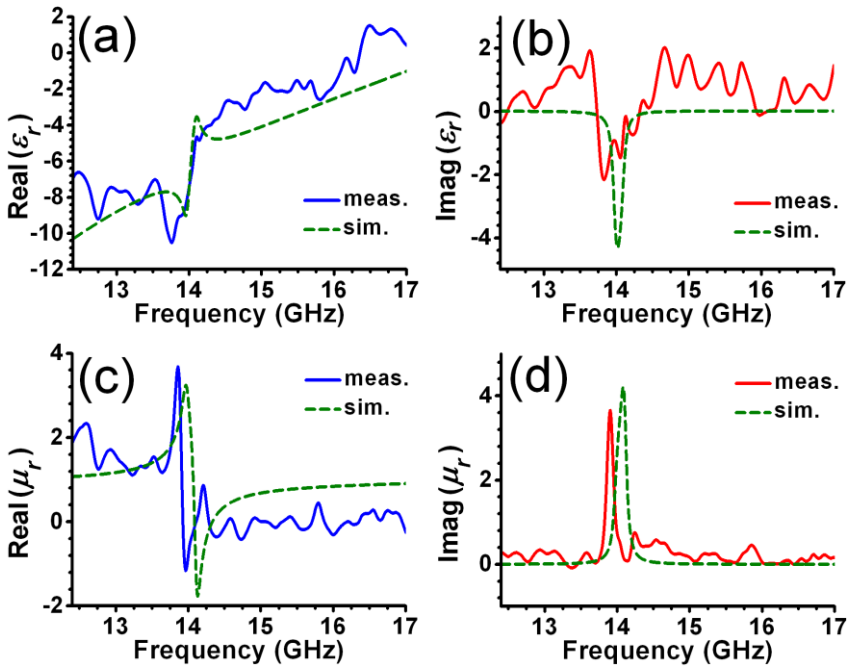

Figure 3.4.6. (Colour Online) Retrieval analysis results for one layer fishnet structure. The simulation (dashed) and experimental results (solid) related to the effective constitutive parameters are plotted.

medium. The experimental reflection coefficients (S_{11}) are obtained by applying the method described in [156]. The retrieval analysis is carried out for both the simulation and experimental results and plotted in figure 3.4.6. The retrieved parameters of the experimental measurements are depicted without applying a smoothing filtering. Still, the main characteristics are consistent with the numerical predictions as it is outlined in figure 3.4.6.

The retrieved constitution parameters in [136] belong to the cut-wire pairs operating at very similar frequency values around 14 GHz. These parameters are shown in figure 3.4.4 of [136]. The striking difference is about the effective permittivity values. The imaginary part of the permittivity which is also responsible for the losses inside the metamaterial turns out to be one order of magnitude higher than the present results in figure 3.4.6(b). Despite the fact that Teflon substrate has been utilized in our experiments rather than FR4 as in the

case of [136], the fishnet suffers less from the losses on the overall in comparison to the cut-wire pair counterparts independent of the substrate selection. The fishnet arraignments also provide superior transmission in comparison to the realizations with the SRR wire combinations [157]. The impedance matching of the fishnet layers are improved around the LH transmission band with respect to the mentioned alternatives. The next important remark we have to make is about the real part of the permittivity which increases rapidly after the magnetic resonance in figure 3.4.4 of [136] in contrast to the smoothly increasing values depicted in figure 3.4.6(a). This rapid increase for the cut-wire case pulls down the plasma resonance and in turn situates the RH band closer to the LH band. In contrast, the well separated LH and RH bands as in the case of fishnet geometries lead to stronger magnetic response and promise a broadband impedance match with the environment.

3.4.2.4 *Back to Fishnet As a Metamaterial*

Menzel *et al.* argued the validity of the effective material parameters in [158] for the fishnet geometry, in which they showed that the weak spatial dispersion was mandatory for such mesoscopic systems to be described in terms of the effective material parameters. They have illustrated that genuine effective material parameters can be introduced only under strict conditions for arbitrary angles of incidence. Stringent constraints have to be imposed on the unit cell size. Marques *et al.* criticized the standard interpretation of the negative refraction adopted in [133,138,143] for the fishnet arrangements [159]. It was brought into attention in [159] that the standard interpretation could not explain why the transverse periodicity of the fishnet geometry was chosen close to the operational wavelength in the regarding studies. At the same time Jelinek *et al.* demonstrated that the homogenization of the fishnet metamaterials was only possible for the incident waves within a small apex angle cone [160]. Eventually, the discussions stimulated new theoretical investigations of the

fishnet configurations. In one of these studies, the origins of the LH band were elucidated with the aid of the gap surface plasmon polaritons propagating through the subwavelength holes [161]. The same phenomenon appearing at the microwave frequencies was justified by making use of the spoof surface plasmons [162].

Independently, Frequency Selective Surfaces (FSS) had been known as early as in the beginnings of the 20^{th} century. Slot arrays were examined as conventional dichroic filters while the operational wavelength (λ) was chosen to be smaller than the cutoff wavelength (λ_c) of the holes [163]. Nevertheless, at the turn of the 21^{st} century the pioneering work of Ebbesen *et al.* reopened the interest in perforated plates even operating at wavelengths higher than the cutoff wavelength of the holes, which resulted in the Extra-Ordinary Transmission (EOT) [164]. The EOT was also observed in sub-terahertz regime and it is attributed to the coupling of the leaky modes through the evanescent waveguide modes of the subwavelength holes [165,166]. It has been emphasized that the EOT is essential in order to achieve the negative refraction in fishnet geometries and a connection between the two mechanisms has been discovered [167,168]. In the preceding years, the LH EOT has been experimentally and theoretically studied for the stacked subwavelength perforated plates [168-174]. Accordingly, transmission-line equivalent circuit models have been proposed, which utilizes the corresponding impedances of the propagating modes to account for the EOT [175-178]. These models are inspired from the FSS and predicted many features of the phenomenon. Analytical investigations provided further physical insight into the physics of the EOT, which linked the diffraction theory analysis with the circuit theory approach [179,180].

Under the light of the current discussions, we know that EOT is governed by the evanescent modes of the subwavelength aperture. Furthermore, our fishnet design bears similarities with the previously examined structures. However, most of the attention is paid to the arrangements with relatively thick purely

metallic layers [169-172]. In some rare cases, these fishnet configurations are patterned on top of a dielectric substrate [177] or sandwiched between two dielectric layers [173,175,181]. The finite dimensions of the slot array degrade the performance of the fishnet geometry under the beam illumination [166]. The sandwiched dielectric slab in between the two interfaces allowed the detection of the EOT phenomenon even in the Fresnel region of the antennas [173]. The dielectric medium is inserted in between the two thin metallic patterns for the presently studied case, which produces differences in the physical mechanism. Although it is not the main scope of this work, we would only like to mention the observed differences and similarities between the present design and the formerly studied cases at this stage. Developing a detailed physical understanding based on these discrepancies and resemblances is the subject of another study.

First of all, our present configuration [see figure 3.4.1(d)] with the mentioned boundary conditions is also equivalent to an artificial TEM waveguide with the relevant perfect electric and magnetic walls, as it has been the case for the previous studies [170,171]. Then, TE_{20} and TM_{02} are the main possible contributors to the transmission with the lowest mode numbers. The symmetry of the problem permits only even-numbered modes for this particular waveguide [172]. Specifically, the electric fields of the TM_{02} modes are in the form of

$$\begin{aligned} E_x &\propto \sin(m\pi x/a_i)\sin(n\pi y/a_y) \\ E_y &\propto \cos(m\pi x/a_i)\cos(n\pi y/a_y) \\ E_z &\propto \cos(m\pi x/a_i)\sin(n\pi y/a_y) \end{aligned} \qquad (3.23)$$

where the mode numbers, $\mathrm{m}=0$ and $\mathrm{n}=2$. Having inserted the mode numbers, it is found out that this mode (TM_{02}) does not possess *x*-component of the electric field or *y*-component of the magnetic field. This semi-analytical method is consistent with our previous statements concerning the field components at the LH band in Sec. 2.1. Furthermore, the illustrated E_z in figure 3.4.3(g) has

only functional variations along *y*-axis, which agrees well with the evanescent waveguide mode in Eqn. (3).

The cutoff frequency of the individual apertures can be calculated for the lowest mode (TE_{10}) of the dielectric loaded rectangular waveguide, $f_c^{diel} = c\Big/\left(2(a_i - w_i)\sqrt{\varepsilon}\right) \approx 14.58$ GHz. For this asymmetric problem the cutoff frequency $f_c^{air} \approx 21.4$ GHz looking from the air side. Due to the special selection of the parameters, i.e., $2(a_i - w_i) = a_i = a_y$, TE_{20} and TM_{02} have the same cutoff frequencies. The EOT is explained as an outcome of the perturbed TE_{10} (the ground state of the individual hole) that is cross-coupled to the TEM modes of the artificial waveguide [175]. Consequently, the LH band residing around 14.3 GHz is just below the cutoff frequencies of the regarding evanescent modes, which is a very similar condition reported in [169-174]. The geometrical parameters have been chosen in [165] and [166] such that $r < \lambda_c < a < \lambda$, where *a* is the lattice spacing and *r* is the aperture radius. The arrangement of the periodicity and the aperture geometry has been the key factor in achieving the EOT for fully metallic slot arrays. On the other hand, $(a_i - w_i) < a_i = \lambda_c^{air} = 2(a_i - w_i) < \lambda_c^{diel} < \lambda$ in our own design due to the sandwiched dielectric slab [see figure 3.4.1(d)]. It should be emphasized that the geometrical recipe for achieving EOT is different in our case. Nevertheless, the EOT is observed below the cutoff frequency, which makes the fishnet arrangement favorable in terms of the losses in contrast to the other metamaterial geometries. In other words, the EOT itself is the origin of the LH band.

Unlike our heuristic approach in Sec. 2.1, the impedances of the corresponding modes are analytically examined and equivalent circuit models have been built in [175-178]. The overall structure is again represented with an LC tank for very thin metallic screens [178]. Then, the admittances can be

calculated as $Y_L = -Y_0\sqrt{1-(f_c/f)^2}$ and $Y_C = -Y_0\Big/\sqrt{1-(f_c/f)^2}$ for the inductive and capacitive terms, respectively, where $Y_0 = \sqrt{\varepsilon/\mu}$. Accordingly, the inductive and capacitive nature of the modal admittances can be seen when $f < f_c$. It was shown in the regarding studies that the inductance was associated with TE_{20} mode, whereas TM_{02} mode was responsible for the capacitance [175-178]. Then, the total impedance of the parallel LC tank attributed to the subwavelength hole is $(Y_L + Y_C)^{-1}$. It is readily seen from the resulting formula that subwavelength holes are inductive well below the cutoff frequency. It was stated that TM_{02} mode plays the dominant role in the EOT and it is the periodicity along the electric field that governed the EOT in purely metallic perforated plates [178]. For such realistic thick screens the modal admittance expressions (Y_L and Y_C) include higher order terms as well as the incorporated losses. Even so, there are two important frequency points around the LH band. In one of them, the susceptance of Y_L is compensated by the susceptance of Y_C and the LH transmission peak appears. In that case, the metallic slot array is impedance matched to the air. The susceptance of Y_C continues to increase after the transmission peak and a singularity emerges from the capacitive part at $f = f_c$. This particular null in the transmission is called Rayleigh-Wood (RW) anomaly. The diaphragm that is modeled as a parallel LC tank connected to the ground acts as a short circuit at the RW anomaly. For the thin metallic screens with subwavelength holes EOT is located very close to the RW anomaly and has a limited bandwidth [178]. Hence, the RW anomaly corresponds to the saddle point between the LH and RH bands in figure 3.4.5 for our arrangement. The drop in the transmission varies in the range from 4.7 *dB* to 24 *dB* with respect to the LH transmission peak around the saddle point for different set of parameters in figure 3.4.5. Ideally, RW anomaly forced zero transmission in the fully metallic layers. Yet, Beruete *et al.* discussed in [175] and [177] that the thin dielectric loading of the fishnet configurations can suppress the RW anomaly.

They have expressed the modal admittances of the contributing modes and a pole in the admittance term always existed as long as the supporting dielectric slab was thick enough. In the case of the rectangular unit cell in [175] and [177], the TE_{20} mode is intentionally adjusted to be the lowest higher order mode. Under these circumstances, the auxiliary factor $F = t_d \sqrt{\varepsilon - 1} / a_i$ was defined to determine whether the pole would appear in the admittance term and whether the capacitance would tend to infinity as in the case of the unloaded subwavelength apertures. For the thin dielectric substrates with $F < 0.25$ the suppression of the RW anomaly takes place and only a local maximum comparably lower than unity in the transmission spectrum is spotted [175,177]. The RW anomaly is also suppressed in figure 3.4.5 in our case; the LC tank representing the subwavelength aperture is not grounded between the LH and RH bands. Yet, the contribution of the TM_{02} mode is present in our configuration due to the symmetry of the square unit cell. Then, a direct adaptation of the *F* number derived in [175] for the determination of the poles is not applicable. The origin of this kind of suppression in the RW anomaly awaits to be unveiled. Additionally, EOT that resides close to f_c^{diel} attains a maximum value of -3.5 *dB* amongst the distinct configurations given in figure 3.4.5. The striking difference is the null in the transmission spectrum just before the LH band. Such a pole in the admittance term had not been pointed out in the regarding previous studies [165-182]. In contrast, the modal impedances were smoothly increasing till the EOT band in those studies. This extra pole which dominates just before the LH transmission peak has been modeled with an additional LC tank (L_2, C_2, R_2) in figure 3.4.4. Our design also comprises dielectric loaded subwavelength holes. It should be stressed that there are resemblances with the referenced studies that considered the problem as an EOT phenomenon through an array of subwavelength apertures. Nonetheless, a unit lattice consisted of a dielectric slab sandwiched between two metallic layers and

a succeeding air spacing (a hybrid, non-uniform lattice structure) has not been analyzed in [165-182] unlike the case in [139-142]. The interactions between the two facing metallic plates in the form of anti-parallel surface currents constitute the LH band in our case. The single side deposited fishnet pattern does not yield the LH band, which is fundamentally different from the situation in [165-182]. The equivalent circuit models addressing the dielectric loaded thin metallic screens have to be reexamined taking into consideration the interactions between the metallic layers, which is beyond the scope of this present work. In spite of these differences, the outlined physical mechanisms in [165-182] establish a starting point in understanding the physics behind our own fishnet geometry.

In figure 3.4.7(a) and 3.4.7(b), the dispersion diagram of the fishnet unit cell is given for the LH and RH bands, respectively for varying a_s values. Eigen Mode solver of CST Microwave Studio has been utilized in the calculations. The results are in agreement with our previous discussions. The LH band is located in the vicinity of 14.3 GHz, whereas the RH band is found out roughly within the range starting from 16 GHz and extending up to 20 GHz. The bandgap between these two bands is associated with the RW anomaly. We define an approximate bandwidth for the LH bands for the corresponding a_s values based on the broadness of the plotted bands on the frequency axis (on the *y*-axis). Then, the bandwidth of the LH band got smaller with increasing a_s values in figure 3.4.7(a) as the coupling mechanism between the layers got weaker in accordance with the transmission results in figure 3.4.5. Moreover, the midpoint of these bands can be approximately thought as the transmission peak of the LH band. These midpoints are estimated as 14.34 GHz, 14.3 GHz, 14.26 GHz and 14.22 GHz when a_s is 2 mm, 3 mm, 4 mm and 5 mm, respectively. We can come to the conclusion that the approximation is reasonable if we compare these values with the presented values in table 3.4.2 for the five-layer case. Still, we have to bear in mind that the dispersion calculations consider periodic conditions along the direction of propagation and

the losses both originating from the metals and dielectrics are not taken into account. Subsequently, we again witness a down shift in the band midpoints with increasing a_s values. The reasons of such a shift have been discussed in Sec. 2.2. The range of the RH band is also modified with the change of the a_s values. The starting edge of the RH band, in other words the plasma frequency is altered, which is again consistent with the depicted transmission results in figure 3.4.5.

The most essential feature of the given bands associated with the LH band is the negative slope. The negative slope in the diagram ($d\omega/dk < 0$) indicates opposite phase and group velocities inside the NIM in the LH band in our spectral region of interest ($f > 14.1$ GHz) where significant transmission is pronounced. Conversely, the slope is positive for the RH band in figure 3.4.7(b), as expected. These are the distinctive characteristic features of the dispersion bands corresponding to the LH and RH propagation regimes. Dispersion relations of the fishnet geometries have also been investigated along the propagation direction in several previous studies [170-172]. The LH band with a negative slope was shown in the regarding studies around the EOT frequency. Alternatively, the RH band with a positive slope was spotted after the cutoff frequency of the individual subwavelength apertures. The RH band does not point to anything different than the frequency response of the conventional dichroic filters in frequency selective surface applications. The forbidden band between these two regimes emerged and it is identified with the RW anomaly [167]. The sign of the slope of the LH band remains negative as long as the fishnet geometries are operated under cutoff frequencies of the individual apertures [170]. It was demonstrated in [171] and [172] that the LH wave propagation could be switched to RH electromagnetic beam propagation by adjusting the stacking period between the fishnet layers and at least theoretically a slow wave could be observed in fishnet arrangements during this transition.

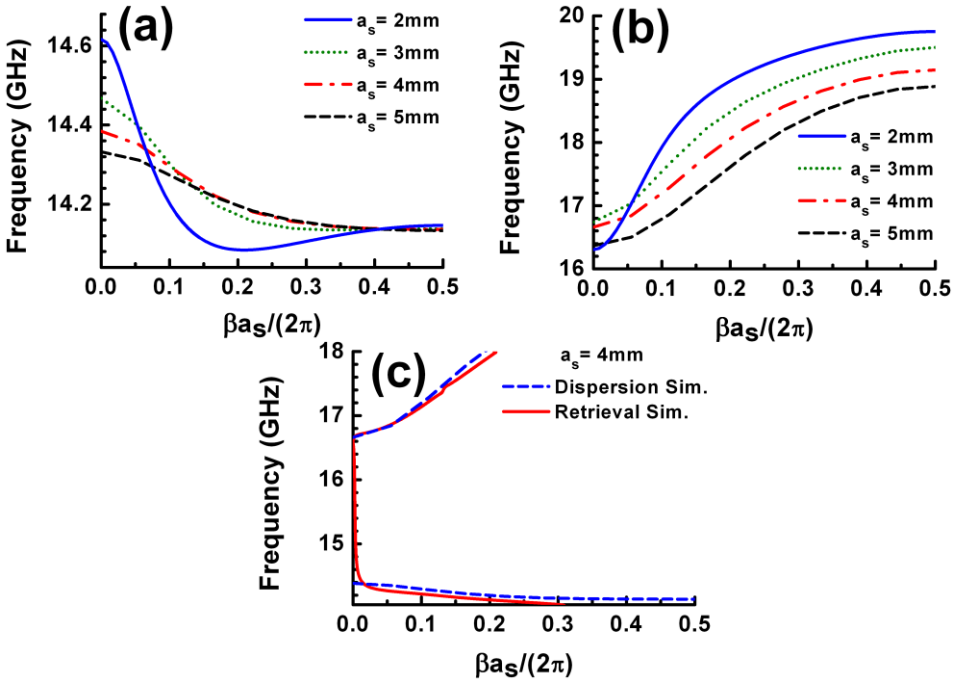

Figure 3.4.7. (Colour Online) The dispersion diagram (a) around the LH band and (b) the RH band. (c) The dispersion information which is obtained by applying the retrieval procedure for a single layer of fishnet ($a_s = 4$ mm) is also plotted (red solid line) for comparison.

For larger periods, the LH character is lost and the stacked fishnet layers are converted into photonic band gap structures with a period along the propagation direction comparable to the operational wavelength. Since our stacking period attains a value as high as $\lambda / 4.2$, we safely stay in the LH propagation regime for all of the studied cases of a_s.

Marques *et al.* adopted the analytical perspective and derived the dispersion relations of the electromagnetic wave propagating through stacked fishnet metamaterials in [159]. They have shown that backward-wave propagation is always expected just below the RW anomaly provided that the longitudinal periodicity is electrically small and the apertures are small enough. Under these restrictions, the stacked fishnet layers can be homogenized for the normal incidence along the longitudinal direction and they behave like the backward-wave TLs. Beruete *et al.* implemented the TL model for the stacked perforated

plates in [170], in which the subwavelength holes are considered as self inductive elements and the intense coupling between the hole array plates resulted in the capacitive term. The TL model as a combination of the shunt inductances and series capacitances allowed backward radiation [128]. The longer periods along the direction of propagation degrade the coupling mechanism between the layers and the LH propagation disappears.

Hence, the dispersion relation of the fishnet structure with $a_s = 4$ mm is replotted (dashed-blue line) together with the dispersion relation obtained as a result of the retrieval analysis (solid-red line) by employing the deduced constitutive parameters (μ and ε) in $k = \omega\sqrt{\mu\varepsilon} = 2\pi f\sqrt{\mu\varepsilon}$ and taking the real part of the wavenumber in figure 3.4.7(c). The two calculations have been conducted for distinct frequency ranges. This is the main reason of the discontinuity for the retrieval results below 14 GHz. Yet, as far as the main frequency range of interest covering the LH and RH bands is concerned, the dispersion results calculated from different branches coincide. This is another way of saying that the TL model proposed for the stacked fishnet layers holds accurately for our case, since the propagation constant for the lossless TL, $\beta = \omega\sqrt{LC}$ where $L \sim \mu$ and $C \sim \varepsilon$ [128]. Except for the slight contribution of the modes in the suppressed RW anomaly in our configuration (between 14.4 GHz and 16.6 GHz), as it is discussed recently, the two dispersion relations are in agreement with each other.

The excitation source is modeled in CST Microwave Studio as a horn antenna that is placed approximately 4λ away from the wedge structure. Absorbing boundary conditions are utilized in order to counteract the possible diffractions at the edges of the wedge structure and the electric fields are illustrated in figure 3.4.8. The field propagates only through the apertures and thereby the phase fronts inside the wedge arrangement are disconnected. The available steady-state electric field solutions that are in the form of

$E = \vec{x}E_x \exp(-j\varphi_x) + \vec{y}E_y \exp(-j\varphi_y) + \vec{z}E_z \exp(-j\varphi_z)$ at a certain frequency in figure 3.4.8(a) are multiplied with a phase term, $\exp(j\phi)$ in order to mimic the time evolution of the time harmonic fields, where $\phi = \omega t$. Subsequently, the field propagation is monitored for three different phase values corresponding to distinct time frames in figure 3.4.8. Thus, the LH behaviour is pronounced such that the phase fronts propagate in backward direction opposite to the energy flow direction inside the wedge medium while both the energy and phase propagation are in the same direction in air medium. The direction of the propagation can be figured out by comparing the relative locations of the phase fronts that are indicated by the dashed lines and arrows. Due to the loss mechanism originating from the additional fishnet layers, the intensity of the fields decays inside the wedge structure and at the output it is observed as if the beam is emitted from the rightmost part of the wedge configuration. The coupling mechanism was introducing immunity against such losses stemming from the addition of extra layers. Thus, the beam is emitted with a comparably larger width at the exit side of the wedge when $a_s = 2$ mm in contrast to the depicted case with $a_s = 4$ mm in figure 3.4.8 [compare movie files 9-12 of ref. 117]. In other words, the suppression of the losses owing to the coupling mechanism results in the enhanced contribution of the thicker columns to the transmission. This situation can be observed in the attached videos related to the phase fronts. It should also be noted that the wave is coupled and can only propagate through the channels encompassing subwavelength holes. The details of the referred wedge studies are going to be studied in the upcoming section.

3.4.3 The parametrical retrieval analysis and the studies of the wedge configuration

As an output of the previous sections, our fishnet configuration can be perceived as a 1-D metamaterial and it supports backward-wave propagation around the LH band for which the homogenization procedure can still be applied for the normal incidence. In the rest of this work, the investigation of the effective NRI in the fishnet medium will be carried out through two branches. The first part will include the retrieval analysis. The simulation as well as the experimental results of the S_{21} and S_{11} parameters will be used to retrieve the constitutive parameters, μ and ε, where the reflection and transmission simulations and experiments are performed with the fishnet layers of the same size. The convergence of the retrieval analysis for different numbers of stacked layers is going to be investigated. The dependence of the retrieval results on the coupling mechanism between the layers is also going to be discussed. In the second part of this section, we are going to focus on the 2D scanning simulations which are carried out by CST Microwave Studio and their comparison with the 2D scanning experiments employing the wedge structure. Since the radiated fields are directional, the results obtained in this step enable the direct calculation of the NRI by using the Snell's law. In the end, we are going to compare the effective NRI values coming from these different examinations.

3.4.3.1 *The dependence of the retrieval results on the coupling mechanism and the number of the stacked fishnet layers*

Employing the retrieved permittivity and permeability values found in Sec. 2.3, the effective refractive indices are calculated and plotted in figure 3.4.9 for one and two layers of fishnet structures with $a_s = 2$ mm. Switching from one layer to two layers, the dip value of the effective NRI becomes smaller in

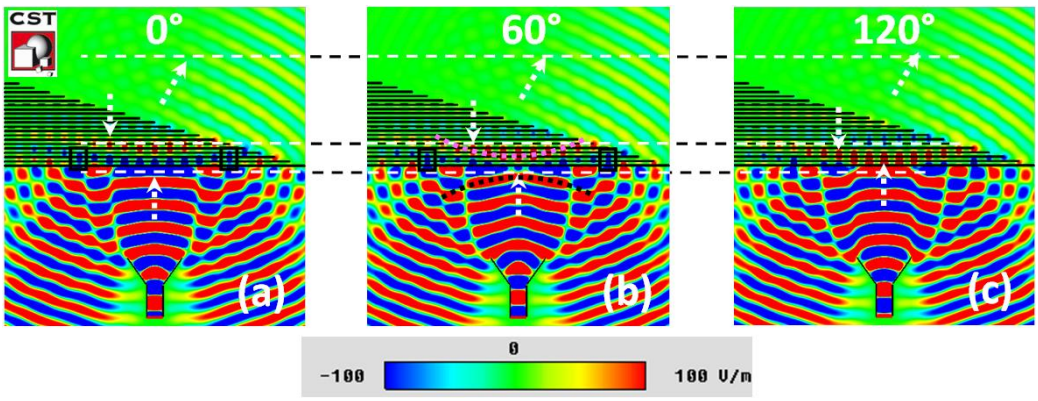

Figure 3.4.8. (Colour Online) The steady-state electric fields at 14.2 GHz at the corresponding time frames. (a) $\omega t = 0^o$, (b) $\omega t = 60^o$ and at (c) $\omega t = 120^o$. The arrows and dashed lines are shown in order to make it easier to visualize the direction of the propagation and the backward propagation, respectively. The respective movie files are also provided for $a_s = 2$ mm (media 9 of ref. 117), $a_s = 3$ mm (media 10 of ref. 117), $a_s = 4$ mm (media 11 of ref. 117), for $a_s = 5$ mm (media 12 of ref. 117).

absolute value. This observation is in agreement with the findings of [183] in which it was reported that the constitutive parameters' absolute value got smaller as the number of layers increased. According to Koschny *et al*. the operation wavelength has to be at least 30 times larger than the unit cell size of the metamaterial along the propagation direction such that the retrieval analyses are fairly immune to the variations in the unit cell size [184]. In contrast, $a_s = \lambda / 10.5$ as pointed out earlier around the LH band for the densest case. Consequently, the sensitivity of the retrieval results to the number of the involved layers in the calculations are foreseeable. Furthermore, the experimentally attained transmission and reflection data give rise to the effective index values very close to the ones obtained from the simulations with the exception of a slight blue shift originating from the mismatches in the material parameters and the difficulties in the experiments.

Simulations are carried out to investigate the variation of the NRI as a function of the number of fishnet layers and the changes in a_s. The results are

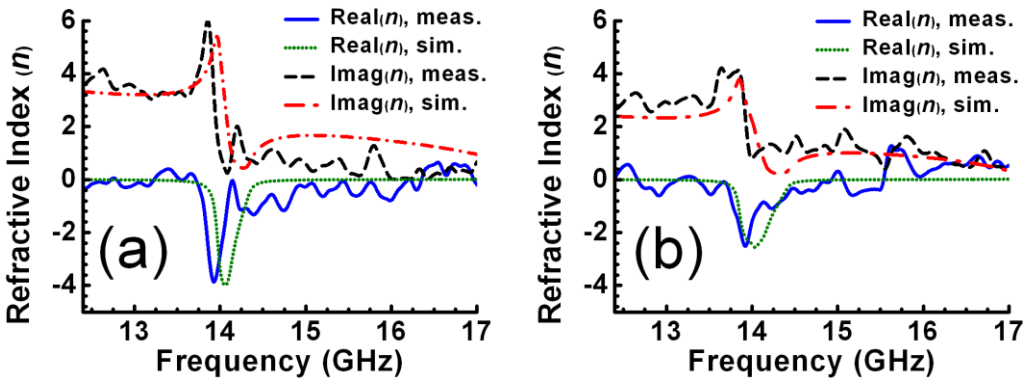

Figure 3.4.9. (Colour Online) Refractive indices calculated by the retrieval procedure employing S_{21} and S_{11} simulation and measurement results for (a) one layer and (b) two layers of fishnet structures. The real and the imaginary parts of the simulation and experimental results are plotted.

given in figure 3.4.10 where the real parts of the refractive indices are plotted. First of all, it is apparent that as the number of layers increases the NRI curves tend to converge to a final curve. That is, for the larger number of layers, the corresponding NRI value does not vary as much as it does for smaller number of layers at any chosen frequency. This observation is also in agreement with the discussion in [183] about the convergence of the NRI when the number of unit cells increases. Secondly, the NRI values got smaller in absolute value whilst a_s is augmented. Such a remark gives clues about the role that is played by the coupling mechanism between the fishnet layers.

Additional discussions can be about the sufficient number of layers to achieve the convergence in the NRI. The corresponding dip values of the NRI depicted in figure 3.4.10 can be found in table 3.4.3. The NRI values are noted down for each unit cell size while the number of the layers included in the retrieval analysis is changed from 3 to 10. It is noticed in the regarding table that in the case of $a_s = 2$ mm with 3 layers of fishnet, the dip value of the NRI is -2.3. As the number of layers is increased up to 10, the NRI dip value converges to -1.8. The same variations at the dip value of the NRI are recorded as from

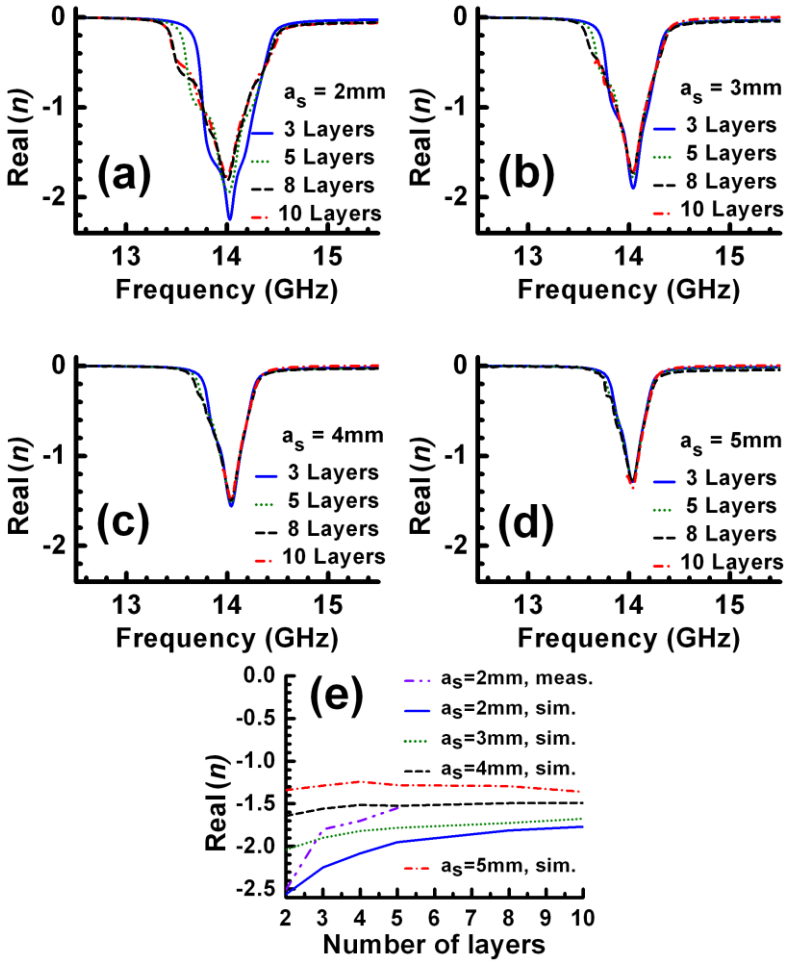

Figure 3.4.10. (Colour Online) The real part of the refractive indices of the fishnet structures with different number layers are obtained by the retrieval simulations for (a) $a_s = 2$ mm, (b) $a_s = 3$ mm, (c) $a_s = 4$ mm, (d) $a_s = 5$ mm as a function of frequency. (e) The real part of the refractive index for distinct unit cell sizes while the number of layers is changed. The depicted values correspond to the magnitudes of the dip values in the curves from (a) to (d). The extracted retrieval values from the experiments for $a_s = 2$ mm is also plotted (dashed double dot violet line) in the same figure.

-1.9 to -1.7, from -1.55 to -1.45 and from -1.36 to -1.3 for the rest of the cases when a_s becomes 3, 4 and 5 mm, respectively. An increase from 5 to 8 layers or from 8 to 10 layers disturbs significantly neither the dip value nor the other NRI values in the rest of the LH band, i.e., the NRI curve saturates after a certain number of layers. For a more quantitative approach, the dip values of the

a_s	3 layers	10 layers
2 mm	-2.3	-1.8
3 mm	-1.9	-1.7
4 mm	-1.55	-1.45
5 mm	-1.36	-1.3

Table 3.4.3. The dip values of the NRI in figure 3.4.10.

retrieved refractive indices are plotted in figure 3.4.10(e). The plotted data in figure 3.4.10(e) is obtained by directly using the minimum values of the curves in figure 3.4.10(a), (b), (c) and (d). It is observed that with the increasing a_s, the required number of layers to achieve a converged NRI decreases. Considering the simulation results in figure 3.4.10(a) for $a_s = 2$ mm, more than 7 layers are required to reach a constant NRI which is not altered any more with the addition of the new layers. On the other hand, 6 layers, 4 layers and 2 layers are sufficient to achieve a saturated NRI value for $a_s = 3$ mm, $a_s = 4$ mm and $a_s = 5$ mm, respectively. This observation is attributed to the reduced coupling between the layers when a_s increases. Even though the unit cell size along the propagation direction is decreasing, the convergence of the effective parameters gets more difficult to accomplish. This fact might sound to be in contradiction with the earlier claims about the retrieval analysis performed on SRR and wire combinations [184] at first glance. Particularly for the fishnet geometry, the coupling mechanism between the layers dominates when the unit cell size is reduced and the convergence of the effective NRI is found to be slower unlike the case with the SRR-wire combinations.

In figure 3.4.10(e), the experimentally obtained retrieval results are also plotted only for $a_s = 2$ mm (dashed double dot violet line). The number of

layers is limited to 5 for the experimental case, since the transmission becomes too low to obtain consistent retrieval parameters for higher number of layers. Additionally, only with the aid of the coupling mechanism against the losses we could carry out the retrieval analysis for the case of $a_s = 2$ mm in the experiments. There is still an evident a convergence behaviour in the dip values of the NRI value for the experimental results when $a_s = 2$ mm, as it can be seen in figure 3.4.10(e). The difficulty of collecting the phase information owing to the misalignments and the aggregated losses obstruct obtaining steady retrieved effective parameters in the experiments for larger a_s values.

The experimental results for the NRI which are obtained by the retrieval analysis are given in figure 3.4.11 for $a_s = 2$ mm. The number of layers is increased from 1 to 5. The lower frequency parts are omitted in the curves for larger number of layers since an inconsistent behaviour is observed due to low transmission for the frequencies below the transmission peak, which is illustrated in the transmission plots given in figure 3.4.5. Nonetheless, the curves for 3, 4 and 5 layers are plotted to express the trend of the behaviour with the increased number of layers. For convenience, the corresponding simulation results which are already given in figure 3.4.10(a) are also replotted in figure 3.4.11(f). It can be once again observed that as the number of layers increases the absolute of the dip value of the NRI decreases while the NRI band becomes wider. Referring back to figure 3.4.6(c), there is a region where $\mathrm{Re}(\mu) > 0$ for $f < 13.92$ GHz in the experimental results and for $f < 14.02$ GHz in the numerical results. Yet, the effective refractive index for the same 1 layer configuration turns out to be $\mathrm{Re}(n) < 0$ again for the same respective frequency regions, as depicted in figure 3.4.11(a). Then again, the transmission figures were very poor at the mentioned frequency ranges which is located just before the LH band [see figure 3.4.5]. This seemingly ambiguous situation is ascribed to these losses and the details of the explanation can be found in [185] and

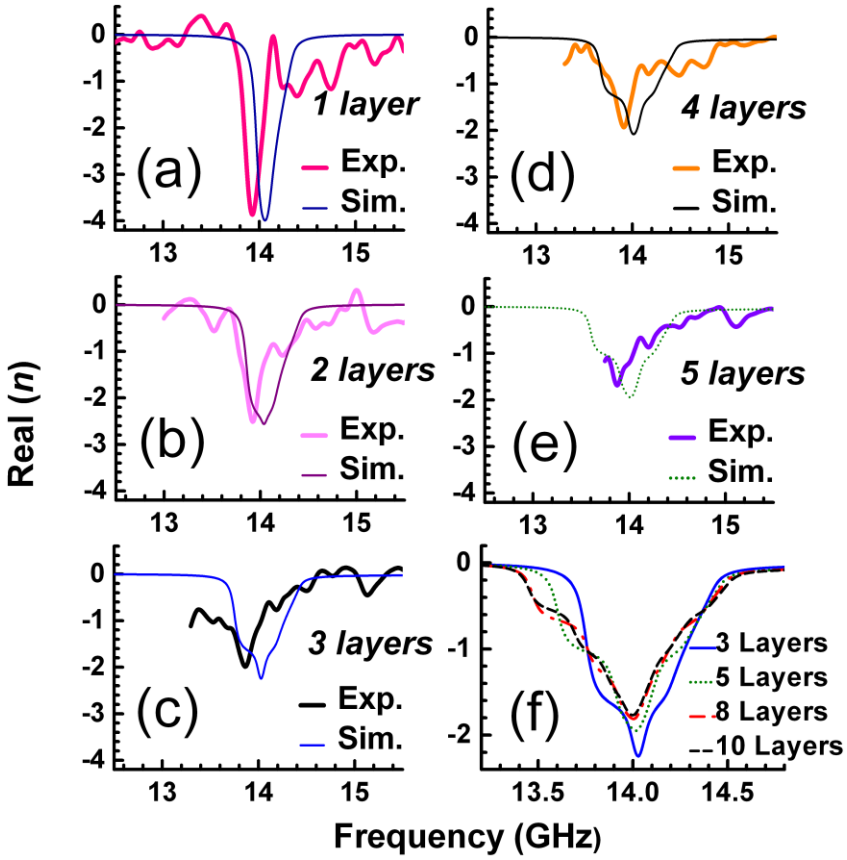

Figure 3.4.11. (Colour Online) From (a) to (e), for $a_s = 2$ mm, both the experimental and the simulation retrieval analysis results are given for the fishnet of (a) 1 layer, (b) 2 layers, (c) 3 layers, (d) 4 layers, (e) 5 layers. In (f), the simulated retrieval results for 3-10 layers ($a_s = 2$ mm) are replotted. The thin solid blue curve in (c) and the dotted green curve in (e) are replotted with the same line types in (f) for the convenience of comparison.

[186]. Lastly, a close examination of [183] reveals that the corresponding plasma frequencies move downwards in the frequency domain with increasing a_s values. The same behaviour of the plasma frequency is exhibited in the dispersion plots of figure 3.4.7(b) and also in the transmission results of figure 3.4.5 such that the starting edges of the dispersion plots in figure 3.4.7(b) are shifted downwards for larger unit cell sizes.

3.4.3.2 *The 2D Scan Studies (Simulations and Experiments)*

The wedge configurations are already utilized in the previous studies with the prospective applications in the telecommunications [186,188]. In addition to the retrieval analysis, the 2D scan experiments employing the wedge-shaped fishnet structure are performed, for which the scanning routine is depicted in Fig 3.4.1(e). The transmitter horn antenna has been placed approximately 4λ (at 14.3 GHz) away from the input surface of the wedge configuration. The aperture area of the identical horn antenna pair is 6.5×4.6 cm^2. Then, the Fresnel Number for such an emitting aperture turns out to be $N_F = A_{\max}^2 / L\lambda > 1$, which indicates that the wedge arrangement is illuminated inside the near-field region of the transmitter antenna (A_{max} is the diagonal of the aperture and L is the distance between the transmitter antenna and the wedge configuration). The fields arrive at the input of the wedge structure after going through a relatively low beam divergence and illuminate a certain part of the wedge interface. This condition can be best monitored in figure 3.4.8. Afterwards, the fields leaving the wedge configuration are recorded by the receiver antenna that scans an area comprising 57.5 cm along *x*-axis and 100 cm along *z*-axis [see figure 3.4.1(e) for the directions]. Consequently, the longest dimension of the wedge structure $D = \sqrt{(19\times a_s)^2 + (20\times a_i)^2}$ and $2D^2/\lambda > R_{\max}$, where R_{max} is the maximum separation between the receiver antenna and the output side of the wedge configuration while the receiver antenna is performing the scanning within the described area. Thus, we are obliged to stay in the near-field region for all of the frequency range of our interest and examined a_s values. However, the directional beams emanating from the output side of the wedge configuration enables the calculation of the deflection angles which are going to be crucial in the estimation of the effective refractive index for the wedge.

The angle of the beam radiated from the output surface of the wedge is measured to calculate the effective NRI by using the Snell's law. The 2D scan

experimental results used for this calculation are given in figure 3.4.12 for a sample frequency (14.28 GHz) for all considered a_s values. The transmission values in figure 3.4.12 are normalized with respect to the maximum attained value for each scenario. These maximum intensities for each case are given in the regarding figure caption. At the sample frequency, the absolute value of the NRI gets bigger, i.e., the wedge structure becomes more refractive while changing a_s between 5 mm, 4 mm down to 3 mm, respectively. As a result, the beam in figure 3.4.12(b) which corresponds to $a_s = 3$ mm case is slightly more inclined with regard to the surface normal of the wedge output interface than those in figure 3.4.12(c) and 3.4.12(d) corresponding to $a_s = 4$ mm and $a_s = 5$ mm cases, respectively. The $a_s = 2$ mm case depicted in figure 3.4.12(a) will be investigated within the context of figure 3.4.16. For the time being, it should be mentioned that a noticeable drop in the transmission values is observed in figure 3.4.12(a) in comparison to the other unit lattice spacing cases. Furthermore, the emanating fields from the wedge surface could not survive for long distances again for $a_s = 2$ mm case. The supplementary videos of the simulation results are also provided, in which the electric fields are plotted [see movie files 17-20 of ref. 117]. A fading effect is again evident for $a_s = 2$ mm after a propagation distance of about 50 cm in the simulation results. Thus, the emitted fields for the case with $a_s = 2$ mm have been confirmed to have a rapid reduction rate. In addition, $a_s = 2\,\text{mm}$ case has been analyzed and it turns out to be the most sensitive scenario to the possible misalignments in the experimental setup owing to the intensified coupling mechanism between the stacked layers. An intentional random shift along *x*-axis has been applied in the simulations in order to estimate the vulnerability of the wedge configuration to such misalignments. A decrease in the intensity values within the range of 3 to 4 has been verified as an outcome of the simulations with a misalignment only along one axis, which aids in understanding the discrepancies specialized to $a_s = 2$ mm in figure

3.4.12(a). Apparently, the situation worsens for the experimental results in which the misalignments in other dimensions are also entailed. Likewise, the misalignments up to 1/5 mm amongst the patterns of the same fishnet layer on both surfaces produces another non-ideality in the experiments, which further degrades the performance of the whole experimental results on the same order as having random misalignments between alternating layers. Nonetheless, it can be seen both in the experimental and simulation movie files that while a_s is kept constant the beam moves in the counter clockwise direction for the increased frequency, which in turn implies that the absolute NRI is decreasing for the frequency range of our interest [see movie files 13-20 of ref. 117].

Figure 3.4.12 clearly demonstrates the negative refraction. Nevertheless, negative refraction had also been shown in the absence of metamaterials by utilizing lossy dielectrics, as well [189]. Munk argued in [190] that the simple Snell's law could no longer be used in the estimation of the effective refractive index for such lossy configurations. In this work, Munk concluded that the asymmetric aperture formation at the exit surface of the wedge configuration due to the losses is the main responsible factor while part of the radiated field appeared on the negative side. Moreover, Hansen emphasized in [191] that the negative refraction caused solely by the loss mechanism required those losses to be very high. Thus, the negative refraction manifested in the NIM composed of the wire and SRR combinations became subject to questions from the perspective of the involved losses. On the other hand, the fishnet metamaterial is mainly favored because of its low losses and this feature promotes it as a well established candidate for the optical applications, as it is discussed earlier. Our fishnet design offers approximately a -3.5 *dB* loss for two layers. Besides, the main beam is directed to the negative side as shown in figure 3.4.12. Although in figure 3.4.12, there are signatures of other features originating from the contributions from the reflections, the negatively refracted beam is well pronounced, which eliminates the possibility of claiming the phenomenon as a

consequence of the wedge losses and the finite prism effect. It is also noteworthy to remember the negative phase advance depicted in figure 3.4.8 within this framework, which puts forward further evidence for the source of the negative refraction instead of the explanations based on the loss mechanisms in our case.

Next, the effect of diffraction in the formation of the outgoing beams is investigated and illustrated in figure 3.4.13. In the diffraction formula, the path difference [solid gray line sections in figure 3.4.1(g)] can be expressed as $na_s - l\sin(\theta_r) = m\lambda$ where the first term corresponds to the path difference in the metamaterial between layers q and q+1 and the second term corresponds to the path difference in air. The effective refractive index at the corresponding frequency is n and l is the length of the line section shown with the dashed gray line in figure 3.4.1(g) and m is the diffraction order. Since $l = a_s/\sin(\theta_i)$, the overall formula can be rearranged as $\sin(\theta_r) = (-m\lambda + na_s)\sin\theta_i / a_s$, where the solutions of the real valued θ_r are indicated with the yellow shaded regions. It is apparent that only the 0^{th} order transmittance (dotted green lines) is evident within these defined areas except for the slight intrusions coming from the higher orders in the frequency territories away from the LH band. Specifically, the -1^{st} order diffraction comes into the picture when $14.03\ \text{GHz} \le f \le 14.04\ \text{GHz}$ and $14\ \text{GHz} \le f \le 14.06\ \text{GHz}$ for $a_s = 4$ mm and 5 mm, respectively. Furthermore, the +1^{st} order diffraction appears roughly above 17.5 GHz for both $a_s = 4$ mm and 5 mm. Aside from these frequency ranges we do not encounter the contribution of the higher order diffraction beams. Thus, the outgoing beam clearly cannot be formed as a result of diffraction.

In the simulation results which are exhibited in the related video files a persistent field can be seen for all cases of a_s that radiates from the tip of the wedge configuration [see movie files 17-20 of ref. 117]. This field originates from the reflections at the wedge input surface. A portion of the impinging wave

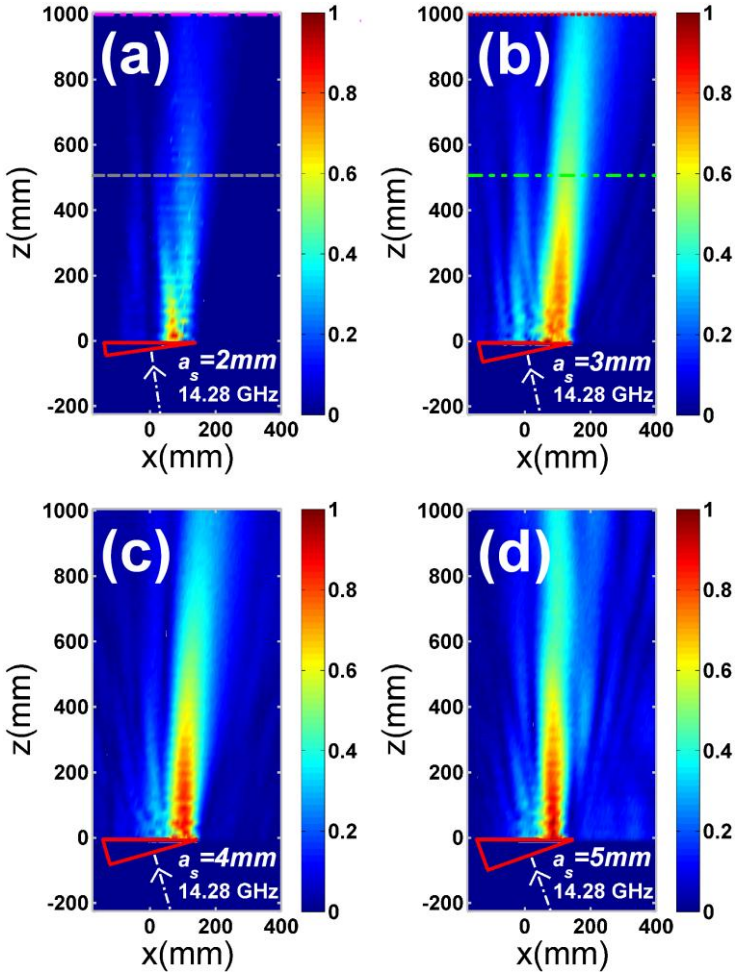

Figure 3.4.12. (Colour Online) The 2D scan experimental results illustrating the intensity distribution for (a) $a_s = 2$ mm, (b) $a_s = 3$ mm, (c) $a_s = 4$ mm, (d) $a_s = 5$ mm. The triangle drawn by the red coloured frame indicates the orientation, position and the relative size of the wedge structure within the measurement domain. The region of interest is limited to $z \geq 0$. The white dashed line and the arrow show the direction of the incident beam. The dashed and the dotted cross sections in figure 3.4.12(a) and figure 3.4.12(b) will be used in the context of figure 3.4.14. The regarding movie files for $a_s = 2$ mm (media 13 of ref. 117), $a_s = 3$ mm (media 14 of ref. 117), $a_s = 4$ mm (media 15 of ref. 117) and $a_s = 5$ mm (media 16 of ref. 117) are provided to inspect the behaviour at other frequency values. The numerically obtained electric field distributions are also presented in the regarding movie files for $a_s = 2$ mm (media 17 of ref. 117), $a_s = 3$ mm (media 18 of ref. 117), $a_s = 4$ mm (media 19 of ref. 117) and $a_s = 5$ mm (media 20 of ref. 117) at the selected frequency values. The maxima of the intensity values in the experimental results are 0.0423, 0.2134, 0.2531 and 0.1656 for $a_s = 2$ 3, 4 and 5, respectively at $f = 14.28$ GHz. The corresponding maxima of the electric field values in the simulation results are 224.110 V/m, 90.619 V/m, 72.569 V/m and 70.619 V/m at $f = 14.28$ GHz.

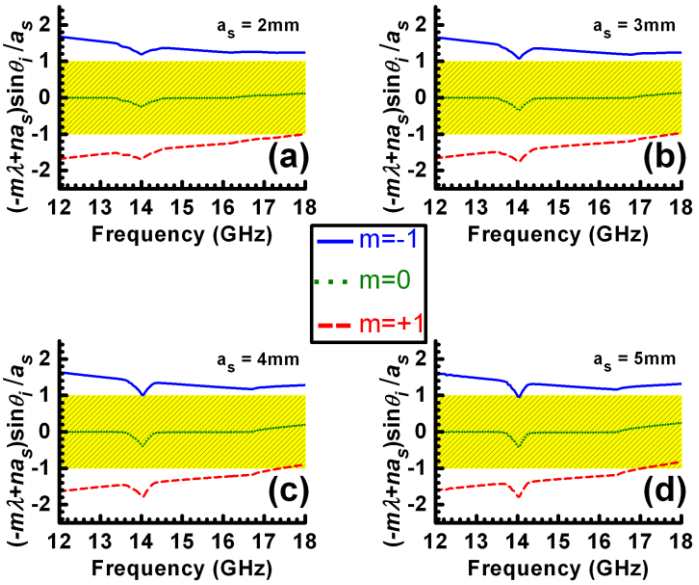

Figure 3.4.13. (Colour Online) The value of $\sin(\theta_r)$ for a range of frequency values. The real solutions of $\sin(\theta_r)$ reside inside the yellow shaded regions on the plots. The -1st (solid blue line), 0th (dotted green line) and +1st (dashed red line) order diffractions are illustrated for (a) $a_s = 2$ mm, (b) $a_s = 3$ mm, (c) $a_s = 4$ mm and (d) $a_s = 5$ mm.

at the input side is coupled to the surface of the wedge configuration. These waves are diffracted from the rightmost tip of the wedge. On the other hand, such a beam is not observed in the experimental results owing to the fact that absorbers were employed at the sides of the wedge arrangement. Additionally, the electric field distributions are given in the media files in contrast to the case with the depicted experimental results in which the intensity values are plotted. Consequently, the emerging fields at the exit side of the wedge configuration look wider in the simulation results.

The effect of the magnetic resonance centreed around the LH band in the transmission can be seen in figure 3.4.14 which is prepared to gain insight about the variation of the angular direction of the radiated beam as a function of frequency. To obtain figure 3.4.14(a), for each frequency we have extracted the single stripe of measurements along *x*-direction at $z = 500$ mm (gray coloured

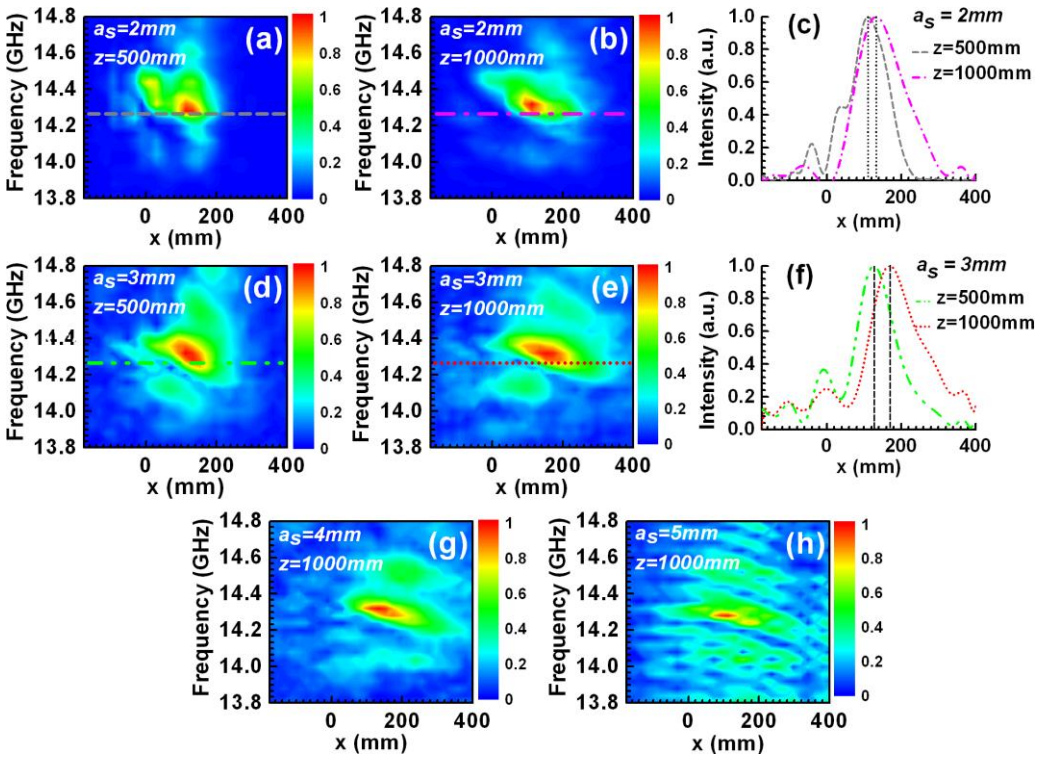

Figure 3.4.14. (Colour Online) The measured intensity distribution maps for (a) $a_s = 2$ mm at $z = 500$ mm, (b) $a_s = 2$ mm at $z = 1000$ mm, (d) $a_s = 3$ mm at $z = 500$ mm, (e) $a_s = 3$ mm at $z = 1000$ mm, (g) $a_s = 4$ mm at $z = 1000$ mm, (h) $a_s = 5$ mm at $z = 1000$ mm. (c) The cross sections from figure 3.4.12(a) and 3.4.12(b) are plotted, (f) The cross sections from figure 3.4.12(d) and 3.4.12(e) are plotted.

dashed cross section in figure 3.4.12(a), $a_s = 2$ mm) and have mapped this single stripe of measurement into figure 3.4.14(a). This procedure is repeated for a sequence of frequencies around the magnetic resonance frequency (14.3 GHz). As the proof for the existence of the NRI, the hot spot appearing in figure 3.4.14(a) is expected to shift rightwards as the *z*-axis cross sections are taken at an increased *z*-value. Then, the same process is repeated for $z = 1000$ mm, i.e., the magenta coloured dash-dotted cross section in figure 3.4.12(a) is mapped into figure 3.4.14(b) for each frequency around the magnetic resonance frequency. The refraction angle, θ_r can be found by examining the shift of the

transmission peak along *x*-axis when the sampling cross section coordinate is moved from $z = 500$ mm to $z = 1000$ mm. For the sample frequency of 14.28 GHz, the cross section at $z = 500$ mm indicated by the gray coloured dashed line in figure 3.4.14(a) is compared with the cross section at $z = 1000$ mm indicated by the magenta coloured dash-dotted line in figure 3.4.14(b). These cross sections are both plotted in figure 3.4.14(c). The shift between the peaks along *x*-axis (Δx) is 20 mm while the difference along *z*-axis (Δz) is 500 mm from $z = 500$ mm to $z = 1000$ mm and $\theta_r = -\tan^{-1}(\Delta x/\Delta z) \approx -2.3^o$. Remembering that $\theta_i = 8.1^o$ for $a_s = 2$ mm and applying Snell's law, the effective refractive index is calculated as $n = \sin(\theta_r)/\sin(\theta_i) = -0.29$. This value is indicated by the dash-double dotted lines in figure 3.4.16(d) to show the NRI value for $a_s = 2$ mm [solid blue line in figure 3.4.16(d)] at 14.28 GHz. Next, a similar process is carried out for the $a_s = 3$ mm case. The green coloured dash-double dotted cross sections at $z = 500$ mm from figure 3.4.12(b) are mapped into figure 3.4.14(d). In the same manner, red coloured dotted cross sections at $z = 1000$ mm from figure 3.4.12(b) are mapped into figure 3.4.14(e). The cross sections which are sampled at 14.28 GHz in figure 3.4.14(d) and figure 3.4.14(e) are plotted together in figure 3.4.14(f). It is seen in figure 3.4.14(f) that $\Delta x = 45$ mm when $\Delta z = 500$ mm, which yields $\theta_r = 5.1^o$. Recalling that $\theta_i = 12^o$ when $a_s = 3$ mm, the NRI at 14.28 GHz is calculated from Snell's law as -0.43. This value is indicated by the dash-double dotted lines in figure 3.4.16(d) to show the NRI value for $a_s = 3$ mm [dotted green line in figure 3.4.13(d)] at 14.28 GHz. figure 3.4.14(g) consists of the cross section mappings taken from figure 3.4.12(c) for $a_s = 4$ mm at $z = 1000$ mm while the cross section mappings for $a_s = 5$ mm at $z = 1000$ mm in figure 3.4.12(d) are depicted in figure 3.4.14(h). These last two figures are provided in order to enable a fair comparison with figure 3.4.14(b) and 3.4.14(e) for the completeness of the set of information about the cross

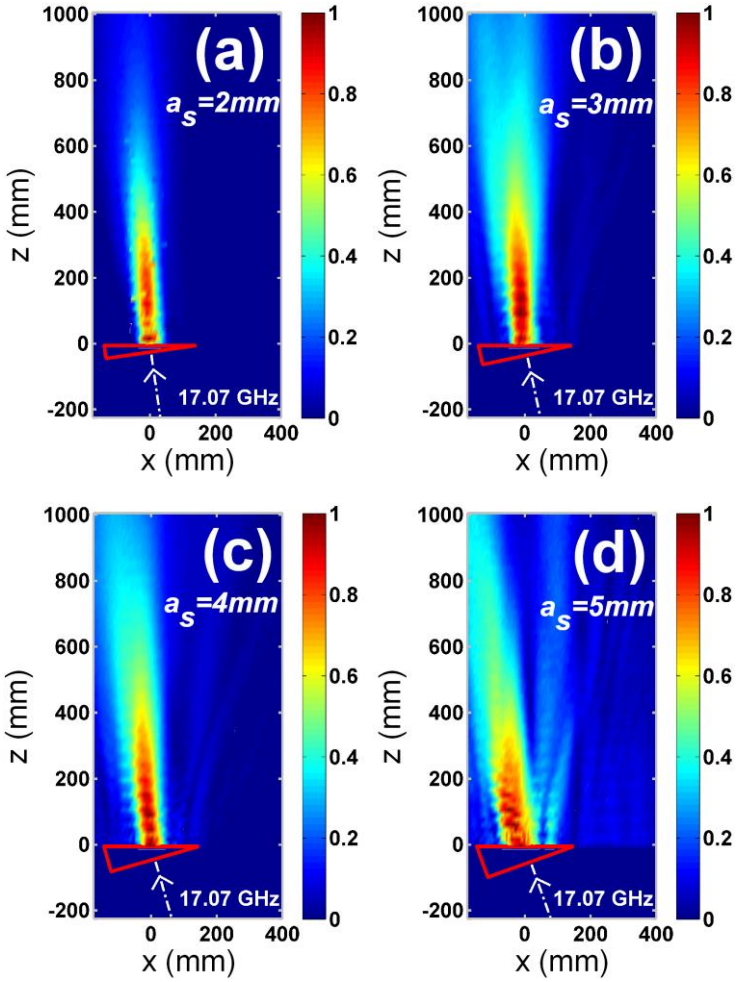

Figure 3.4.15. (Colour Online) The radiation at $f = 17.07$ GHz for (a) $a_s = 2$ mm, (b) $a_s = 3$ mm, (c) $a_s = 4$ mm, (d) $a_s = 5$ mm. The beams are positively refracted for all cases. The maxima of the intensity values in the experimental results are 0.2, 0.6, 0.6 and 0.18 for $a_s = 2$ 3, 4 and 5, respectively at $f = 17.07$ GHz.

sections taken at $z = 1000$ mm for $a_s = 2$ mm to $a_s = 5$ mm. It is seen in figure 3.4.14(e), (g) and (h) that as a_s is increased the hot spot which corresponds to the transmission at resonance is shifted slightly towards left. As a result, the refraction angle and consequently the absolute values of the NRI are decreased. The position of the hot spot for $a_s = 2$ mm lies in between that of cases $a_s = 3$

mm and $a_s = 4$ mm. This is another aspect of the findings of figure 3.4.16(d). The special case for $a_s = 2$ mm and the overall dependence of the NRI to the corresponding a_s values will be revisited in the upcoming section.

Finally, the *XY*-scan results for a non-resonant frequency are given in figure 3.4.15 for comparison. Considering the incident beam and the normal of the exit surface, the positive refraction is observed in the 2D Scanning experiments obtained at 17.07 GHz. This particular frequency belongs to the RH band and it is above the cutoff frequency of the dielectric loaded apertures, as it was discussed in the previous sections. As a result, higher transmission values in comparison to those illustrated in figure 3.4.12 are monitored in figure 3.4.15. It should be noted that in accordance with the LH band experimental intensity distribution results for $a_s = 2$ mm, the fields have once again died out quicker in figure 3.4.15(a) in contrast to the other cases depicted in figure 3.4.15(b), (c) and (d) owing to the experimental difficulties. The experimental results are once more normalized with respect to the highest attainable intensity values in figure 3.4.15 for each case. These maxima can be seen in the regarding figure caption. Then, the optical path inside the wedge configuration is the largest for $a_s = 5$ mm, which brings relatively higher losses and correspondingly smaller intensity values. The difficulties in the experiment originating from the misalignments for $a_s = 2$ mm case is again evident by yielding a rather smaller maximum intensity value. Figure 3.4.9 reveals that the effective refractive index of the wedge structure is supposed to be $0 < n < 0.5$ depending on the retrieval results. Hence, the intensity results illustrated in figure 3.4.15 is in agreement with the predictions of the retrieval analysis. Then, the wedge arrangement can be considered within the context of the near zero index materials. Such arrangements designed with metamaterials had been previously demonstrated to improve the directivity of the embedded sources by refracting the outgoing beam at an angle very close to the normal of the output interface obeying the

Snell's law [192]. Likewise, the outgoing beam is detected to be refracted close to the surface normal in our case. The incoming field from the antenna propagates parallel to the normal of the entrance surface of the wedge inside the wedge configuration all the way up to the exit surface and impinges with an incident angle almost equal to the wedge angle. Since the wedge angle is increased while a_s is swept from 2 mm to 5 mm, the outgoing beam follows this increment in the wedge angle from figure 3.4.15(a) to (d) by steering the radiated beam in the counter clockwise direction. Finally, the higher order diffractions are not seen in figure 3.4.15 in view of the fact that figure 3.4.13 does not generate a real solution for the refracted angle at this particular frequency for all a_s values. There exists only an edge effect as it is defined for the RH wedge configurations in [193] for $a_s = 5$ mm. It is less pronounced in $a_s = 4$ mm case. This edge effect accompanied the main beam for the wedge arrangements when the operational frequency was chosen to be higher than the cutoff frequency of the apertures constituting the fishnet layers in [193], which is in analogy with the current situation in figure 3.4.15.

3.4.3.3 *The comparison of the Retrieval and 2D Scan Studies*

When we return back to figure 3.4.12, we immediately notice that the outgoing beam is shifted towards right while a_s is increased from 2 mm to 5 mm. The same shift is evident in the simulation results that are given in the movie files, as well. Since, the coupling mechanism between the two adjacent fishnet layers was more pronounced when a_s got smaller values, the wave inside the wedge configuration could survive for longer periods once $a_s = 2$ mm and suffered from relatively higher losses for the case of $a_s = 5$ mm [inspect media files 9-12 of ref. 117]. As a result, the main portion of the exiting beam is emitted from a location closer to the tip of the wedge configuration for larger a_s values. Yet, we have to emphasize once again that this loss mechanism is not responsible for the

negative refraction in the wedge structures, as it is discussed earlier. The refractive index values that are extracted from the wedge simulations are in close range of the retrieved values of the metamaterial fishnet slabs under a finite beam width illumination. The effect of the losses does not manifest itself in the RH band and a significant lateral shift of the outgoing beam is not reported in figure 3.4.15. These losses are dramatically decreased and the outgoing beam emanates from the whole surface of the wedge for the fully metallic fishnet layers lacking any addition of the dielectric layers [147,193]. Thus, the effect of the losses in the overall does also play a major role in the evaluation of the beam width that is originating from the output surface of the wedge structure. Due to the frequency dependence of the transmission of the fishnet layers, it is not completely fair to compare the effective aperture sizes at the exit interface of the wedge configurations in figure 3.4.12. Nevertheless, it is apparent that the effective aperture reduces in size as a_s values got increased from 3 mm up to 5 mm. The same features have been observed in the corresponding simulation results, as well. When we also take into consideration the frequency dependence, it is witnessed that the beam attains the largest width for $a_s = 2$ mm. The effective aperture size at the output interface is a contributing factor that determines the spatial widening of the beam in figure 3.4.14. The smaller beams tend to diverge more but are still smaller in width in contrast to the initially wide beams, since we stay in the near field at $z = 1000$ mm, such a characteristic can be seen in figure 3.4.14. Expect for the experimentally difficult case, $a_s = 2$ mm, the hot spot representing the beam width is the smallest for $a_s = 5$ mm and gets expanded for $a_s = 3$ mm [compare figure 3.4.14(e), (g) and (h)]. Lastly, the reduced coupling between the layers in $a_s = 5$ mm resulted in smaller intensity values to be produced at the output. Thus, the enlarged spatial spreading of the $a_s = 5$ mm case in figure 3.4.14(h) is caused by the normalization process of the intensity profiles.

However, it is not trivial to decide on the wedge arrangement that instantly gives away the highest transmission results. The wave propagates easier without the need to tackle the losses for a smaller a_s value. On the other hand, the wave travels through higher number of layers along the propagation direction again for a smaller a_s value, which introduces losses. It can be straightforwardly deduced that the case with a smaller a_s value generates the higher transmission values for the fishnet metamaterial slab case, but there is a compensation mechanism between the coupling mechanism and the losses coming from the involved number of layers for the wedge case due to the specific shape of the prism. Hence, comparable transmitted intensity values can be monitored for wedge configurations with distinct a_s values.

The transmission band is expected to move to the higher frequencies with a smaller a_s value, as it is shown in the previous sections. Correspondingly, the LH transmission band resides in between 14.24 GHz and 14.49 GHz, 14.18 GHz and 14.47 GHz, 14.18 GHz and 14.4 GHz, 14.16 GHz and 14.36 GHz for $a_s = 2$ mm, 3 mm, 4 mm and 5 mm, respectively in figure 3.4.14 [compare the extension of the islands representing the transmitted intensities in the frequency domain in figure 3.4.14(b), (e), (g) and (h)]. Meanwhile, the operational bandwidth depends on two factors. The coupling mechanism broadens the LH band, while the addition of the extra layers restricted the operational bandwidth [inspect figure 3.4.5]. Since the wave is bound to propagate through higher number of layers for a smaller a_s value inside the wedge configuration, it should be pointed out that a smaller a_s value does not guarantee a wider transmission band. This phenomenon explains why the $a_s = 3$ mm case possesses an enlarged transmission band with respect to the $a_s = 2$ mm case in figure 3.4.14.

Next, we move on to the comparison of the previously attained retrieval results with the extracted refractive index values from the wedge configurations. The calculated refractive indices using the results of the retrieval analysis

employing the stacked fishnet layers of the same dimensions and the 2D Scan studies employing the wedge structure are plotted together in figure 3.4.16. Recalling the discussion related to figure 3.4.10, the retrieval analysis experienced a convergence with the insertion of additional layers. Several layers were needed to be sufficient to reach the converged value of the effective NRI. The assumption that the converged value of the NRI is almost reached for all a_s values with 8 layers is made based on the situation given in figure 3.4.10(e). In figure 3.4.16(a), the refractive indices which are obtained by the retrieval analysis of the simulations for $a_s = 2$ mm to $a_s = 5$ mm are replotted for 8 layers of fishnet. Again, the region remaining inside the dash-double dot frame in figure 3.4.16(a) is replotted in figure 3.4.16(c) for the convenience of the reader. These simulation NRI curves obtained by the retrieval procedure is to be compared with those given in figure 3.4.16(b) and (d) which are obtained by directly applying the Snell's law to the 2D scan simulation and experimental results, respectively. Ideally, the corresponding curves in figure 3.4.16(b), (c) and (d) are expected to overlap to verify that the results obtained by retrieval analysis are valid and are comparable with those obtained by applying the Snell's law. In figure 3.4.16(b), (c) and (d) the similar behaviour in the NRI is observed for $a_s = 3$ mm, 4 mm and 5 mm. In all of them, there is a trend such that for increasing a_s the absolute value of the NRI is decreased in the whole frequency range plotted. As for $a_s = 2$ mm, the effective NRI becomes more ambiguous since more number of layers are involved in the transmission. The comparison between the NRI values becomes once again nontrivial. As the number of layers increased the NRI value decreased in absolute value, whereas a decrement in a_s ended up with an increase of the absolute value of the NRI value. The wedge configuration can be interpreted as a combination of the columns with different number of layers. Thus, a close inspection of media files 9-12 of ref. 117 already revealed that the main portion of the wave exited from

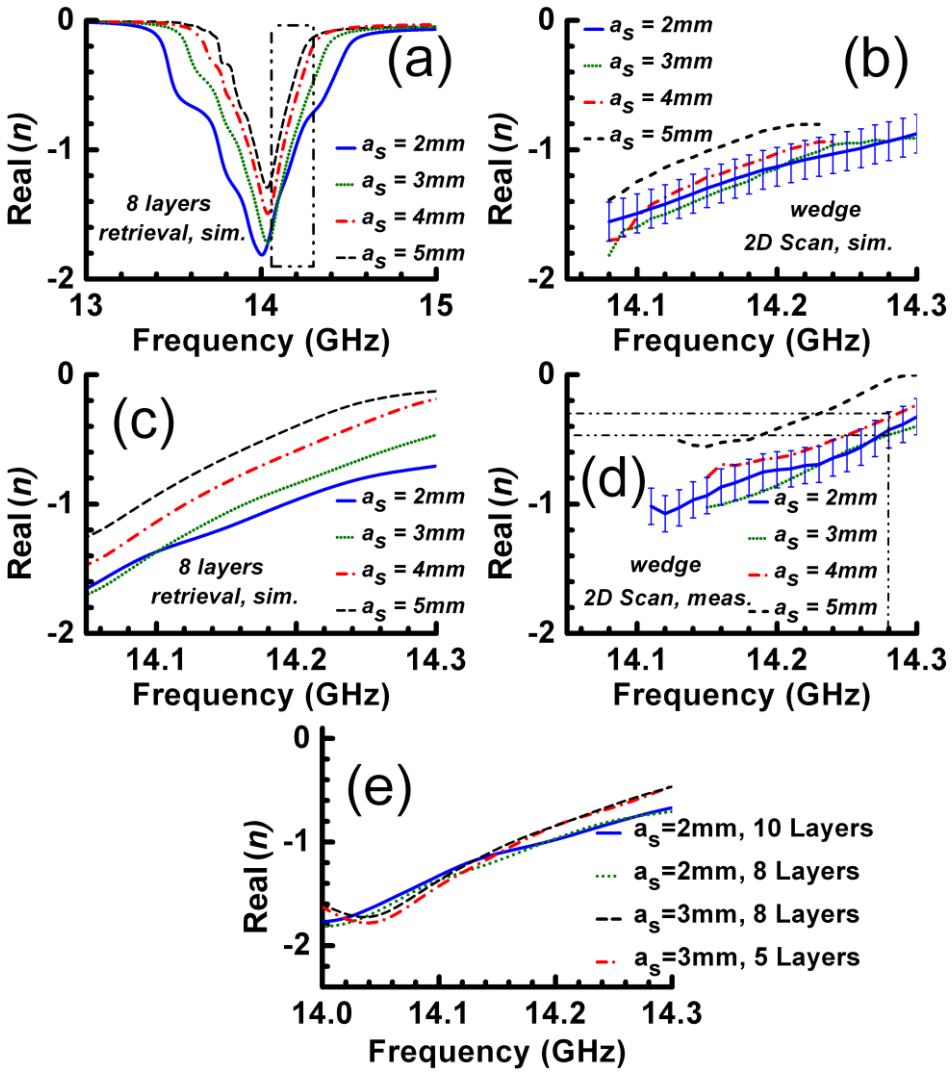

Figure 3.4.16. (Colour Online) The NRI obtained by (a) the retrieval analysis applied to 8 fishnet layers stacked by separation of $a_s = 2$ mm (*simulation*), (b) applying Snell's law to the 2D *XY* Scan *simulations* using the wedge shaped fishnet structure, (c) zooming into the framed region in figure 3.4.16(a), redrawn for the convenience, (d) applying Snell's law to the 2D Scan *experiments* employing the wedge structure. The horizontal and vertical dash-double dotted line sections in figure 3.4.16(d) are explained in the context of figure 3.4.14(c) and (f). They indicate that the corresponding NRI is -0.29 for $a_s = 2$ mm (solid blue line) and is -0.43 for $a_s = 3$ mm (dotted green line) at 14.28 GHz. (e) The retrieved refractive index results for the given a_s values and number of layers (*simulation*).

the columns with higher number of layers for $a_s = 2$ mm in the above discussions. Consequently, there is once again another compensation mechanism

between the number of layers and the utilized a_s value in the estimation of the NRI. Obviously, the values attained in figure 3.4.16(c) that are based on the transmission through a fishnet metamaterial slab will differ from the extracted NRI values from a wedge configuration of the same design. Figure 3.4.16(e) aims to address the issue of the *sensed* NRI and it also attempts to elucidate how the $a_s = 2$ mm case can take smaller amplitudes of NRI values in comparison to the $a_s = 3$ mm case. For a wedge shaped fishnet structure a distribution of the refractive indices should be taken into account rather than a certain converged NRI value once the layer to layer coupling becomes strong, as in the case of $a_s = 2$ mm. This is the main reason why the error bars are included for $a_s = 2$ mm in figure 3.4.16. While the beam is travelling through the columns of 1-D transmission lines with different lengths in the wedge configuration, it attains distinct propagation constants specific to every column. The phase fronts of the incident wave and the one travelling inside the wedge configuration are shown in figure 3.4.8 with black and pink colours, respectively. Yet, the propagation constants are assigned to higher values for the columns closer to the tip of the wedge at the right hand side due to the decreased number of layers. Then, a careful examination shows that the phase fronts at the right hand side are slightly lagging behind the ones at the left hand side [the comparison is highlighted in the boxes in figure 3.4.8(b)]. The significant fraction of the wave exits the wedge from a region that lies between the 8^{th} and 10^{th} columns for $a_s = 2$ mm, whereas the substantial part of the exiting beam is detected at the area intersecting with the end of the columns from the 5^{th} up to the 8^{th} for $a_s = 3$ mm. Then, for a certain range of frequency values the NRI can attain smaller values in absolute value for the case of $a_s = 2$ mm in comparison to the case of $a_s = 3$ mm, as depicted in figure 3.4.16(b) and (d). Such a condition would not be sustainable for the metamaterial slab case after 14.1 GHz, as illustrated in figure 3.4.16(c). Conversely, the simulations and experiments based on the

wedge configuration has allowed the case of $a_s = 2$ mm to get NRI values smaller in amplitude than that of $a_s = 3$ mm case to an extended frequency as high as 14.2 GHz, approximately.

It is suspected that the high sensitivity of the NRI values to the layer number for the case of $a_s = 2$ mm gives rise to the relatively rapid decrease of the radiated fields in comparison to the other scenarios at the exit of the wedge configuration in figure 3.4.12(a). The refracted beam originating from neighboring columns is directed with a certain angle for $a_s = 3$ mm, 4 mm and 5 mm, which enables us to detect the radiation at $z = 1000$ mm. On the other hand, the emanating beam at the exit of the wedge configuration is deduced to have a wider wave vector spectrum for $a_s = 2$ mm, owing to the sensitivity of the NRI values with the employed layer numbers. Thus, it is concluded that the fields undergoes destructive interference mechanism resulting in the disappearance of a directed beam at $z = 1000$ mm for $a_s = 2$ mm case.

Comparing figure 3.4.16(b) and (c), the reported results are found to be close to each other especially in the 13.8 GHz-14.22 GHz band. Furthermore, the results in figure 3.4.16(d) are comparable with those given in figure 3.4.16(c) in the 14.14 GHz-14.30 GHz band. Thus, for the 14.14 GHz-14.22 GHz band, the retrieval simulations together with the 2D scan simulations of the wedge shaped fishnet structure and the actual 2D wedge structure experiments yield to similar results.

Figure 3.4.17 depicts all of the refractive index values attained from different approaches for all a_s cases. Additionally, the experimentally obtained retrieval results are also plotted only for $a_s = 2$ mm in figure 3.4.17(a). Ideally, all of the four curves are expected to overlap for the validity of the match between the retrieval analysis results and the 2D scanning results in figure 3.4.17(a). All the curves are plotted in their available frequency ranges in figure 3.4.17. Especially, in the 2D Scanning simulations and experiments which are carried

out with the wedge shaped fishnet structure, there exists a challenge to pursue the application of the Snell's law in the calculations for an observable directive beam. However, the beam formation has been observed only through certain operational frequency bands. The NRI bandwidth was getting larger with the decreasing a_s values, as already discussed in the previous sections. In accordance with these earlier claims, the operational bandwidth for the corresponding a_s values where a NRI was still observable turned out to be the largest for $a_s = 2$ mm and smallest for $a_s = 5$ mm in figure 3.4.17.

The data only above the frequency corresponding to that of the NRI dip value can be presented for the experimental results obtained by the retrieval analysis. Actually, the low transmission levels were apparent just before the LH transmission peak [see figure 3.4.5], which obstructs the consistent phase measurements below the frequency corresponding to the NRI dip value. In the same manner, the NRI values could also be only illustrated for the frequency ranges after the NRI dip in the 2D scanning results. The frequency shift between the experimental and simulation results is attributed to the difference between the actual electromagnetic parameters of the dielectric material and the commercially provided information.

Figure 3.4.17 shows that a homogenization procedure that can be applied from the retrieval results attained from the fishnet metamaterial slab works up to a certain degree. All of the refractive index results based on the scanning experiments fall into a close vicinity of the retrieval results, which removes the doubts concerning the origins of the physical phenomenon. Despite of the ongoing discussions about the underlying physics of the negative refraction in metamaterials, the negative refraction is clearly attributed to the LH material rather than the loss mechanisms and neither the geometry of the prism nor the possible diffractions in our design. Yet, a performance comparison analysis cannot be generalized amongst the considered a_s values solely based on the

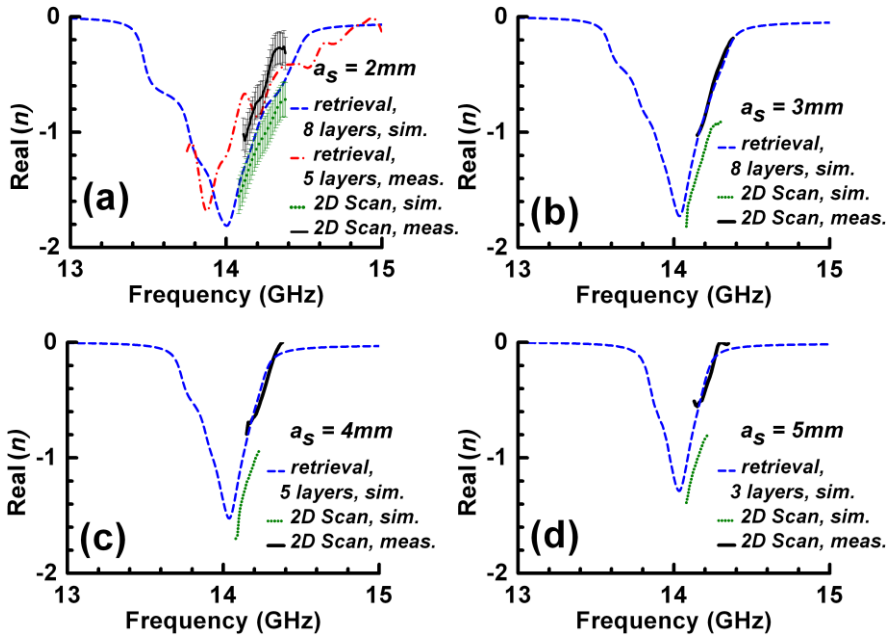

Figure 3.4.17. (Colour Online) The comparison of the NRI values found by different methods with the given number of layers in the retrieval results (dashed blue line) obtained in simulations. In (a), the experimentally retrieved NRI values are also given only for $a_s = 2$ mm (red dashed dot line). The extracted NRI values from the scanning simulations (dotted green line) and measurements (solid black line) are also plotted for (a) $a_s = 2$ mm, (b) $a_s = 3$ mm, (c) $a_s = 4$ mm and (d) $a_s = 5$ mm.

metamaterial slab results. It is seen in figure 3.4.17 that the case with $a_s = 2$ mm produces the largest deviations from the retrieved results while generating an uncertainty in the NRI values in the scanning results represented with the error bars.

3.4.4 Conclusion

The origins of the resonance characteristics for the stack of fishnet layers are investigated by demonstrating the inductive and capacitive effects in the LH band. The oppositely directed parallel currents on different faces of the same

layer are attributed to the inductive behaviour while inducing a strong H_x component of the magnetic field due to the loop like currents [see figure 3.4.2 and 3]. Additionally, the capacitive effect is eminent with the electric field formation (E_z) between the metallic depositions of the same layer. As a result, the high transmission is explained as a consequence of the *LC* resonance in the LH band, heuristically. The corresponding *LC* model in [139] is connected to the existing field components in the fishnet structure. The generalized formulation for the magnetic resonance frequency is verified for two other sets of fishnet geometries studied in the literature. Furthermore, the *LC* model also predicts accurately the location of the magnetic resonance frequency for our design. The transmission peak of the LH band is spotted at 14.18 GHz in the transmission simulations (1-layer case) whereas the *LC* model yielded a magnetic resonance at 14.22 GHz. The situation is different for the RH band for which the subwavelength apertures of the fishnet arrangement introduce a capacitive effect in contrast to the LH band. As a result, the transmission of a single fishnet layer is modeled with different equivalent lumped circuit parameters for the LH and RH bands [see figure 3.4.4 and table 3.4.1]. In the end, it is shown that the physical interpretation of the induced currents and field components enables a means of understanding several features of the transmission spectrum of the fishnet structures.

From another perspective, the LH behaviour in our design is explained by referring to the artificial TEM waveguide modes of the subwavelength apertures [169-174]. Adapting this approach has been proven to be useful for our case in interpretation of the supported TM_{02} mode of the artificial waveguide, which produces only E_y, E_z *and* H_x field components. Under the light of the previous debates, the electromagnetic propagation through the fishnet arrays has been examined in our case combining different perspectives in order to clarify the characteristics of the transmission spectrum of our fishnet structures, which will be crucial in the understanding of the results to be offered by the wedge studies.

Similar to the case of the fully metallic fishnet layers utilized in the earlier studies, our LH band, which is another manifestation of the EOT, is demonstrated to reside below the cutoff frequency of the subwavelength apertures. However, the discrepancies with the fully metallic fishnet configurations are also emphasized since the dielectric slab for our case is sandwiched by two aligned metallic fishnet patterns. Thus, a LH band is apparent even with a single layer of fishnet in the present study [see figure 3.4.6, 3.4.7 and 3.4.9]. Nevertheless, the modal admittances of the evanescent modes propagating through the subwavelength arrays are exploited to gain insight about the RW anomaly in the current design. The present study has revealed that a suppression of the RW anomaly for our case is evident. Accordingly, a transmission null after the LH transmission peak is not observed and the drop in the transmission is limited in the range from 4.7 *dB* to 24 *dB* with respect to the LH transmission peak for different sets of parameters [see figure 3.4.5]. Additionally, a null in the transmittance has also been detected in the transmission spectrum just before the LH band unique for our case.

Several observations are summarized for the parametrical variations in a_s and number of layers from the transmission studies [see figure 3.4.5 and table 3.4.2]:

i) In the LH band the transmission values turn out to be higher for smaller a_s arising from the enhanced coupling.

ii) The valley between the LH and RH bands tend to disappear (even more suppression of the RW anomaly) due to better impedance matching for smaller a_s.

iii) Besides, the magnetic resonance frequency tends to saturate and do not change with the additional layers after a certain number of employed layers.

iv) The LH bandwidth gets expanded with decreasing a_s owing to the elevated coupling mechanism between the layers.

v) When a_s is reduced, the transmission peak experiences a blue shift due to the reduction in the average magnetic flux passing through the individual fishnet layers. Thus, it causes the inductive effect which is attributed to this magnetic flux to be weakened. As a result, the resonance frequency increases.

vi) The losses are increased as the distance travelled by the electromagnetic wave is prolonged, i.e., the number of layers is increased.

vii) The LH bandwidth is inversely proportional to the employed number of layers.

Later on, the retrieval analysis is carried out to find the effective permittivity, permeability and the refractive index values [see figure 3.4.6 and 3.4.9]. These parameters have been employed in order to attain the dispersion relation for the propagating wave inside the homogenized fishnet slab. Another calculation of the dispersion relation is made by the Eigen mode solver of the CST Microwave Studio software. The calculations of the dispersion relation from these two methods are found to be in agreement, which further approves that the stacked fishnet layers form a 1D metamaterial along the direction of propagation [see figure 3.4.7]. Furthermore, the statement indicated in (v) is validated once again with the dispersion results for different a_s values. Apart from the findings mentioned above, the dispersion graphs made it possible to add other observations:

viii) Concerning the parametrical variations in the fishnet configurations the plasma frequencies move downwards with increasing a_s values. This behaviour of the plasma frequency is exhibited in the dispersion plots and also in the transmission results such that the starting edges of the dispersion plots shift downwards for larger unit cell sizes.

ix) The LH band possesses negative slope which dictates negative phase velocity. On the other hand, the RH band in the dispersion plots illustrates a positive slope as in the case of usual materials.

The retrieval analysis is performed on both the simulation and the experimental results. The consistent NRI which corresponds to the LH frequency band is observed for both of the results. It is deduced from the retrieval studies that [see figure 3.4.9, 3.4.10, 3.4.11 and table 3.4.3]:

x)The convergence in the NRI values happens to be dependent on the number of layers for the investigated design.

xi) As the number of layers along the propagation direction is increased the absolute value of the NRI gets smaller.

xii) The absolute value of the NRI again gets smaller for increasing a_s values. The dip value of the NRI converges to -1.8 ($a_s = 2$ mm), -1.7 ($a_s = 3$ mm), -1.45 ($a_s = 4$ mm) and -1.3 ($a_s = 5$ mm) for 10 layers of fishnet.

xiii) For each case of a_s, the NRI value converges to a distinct constant with the increasing number of layers.

xiv) The number of layers required for the convergence of the NRI is reduced for higher a_s values. That is, the variation in the NRI which occurs when changing the number of layers is decreased when a_s is set to be a bigger value. For $a_s = 2$ mm, more than 7 layers are required to reach a stable NRI which is not disturbed by the increased number of layers. On the other hand, 6 layers, 4 layers and 2 layers are sufficient to achieve a relatively converged NRI for $a_s = 3$ mm, $a_s = 4$ mm and $a_s = 5$ mm, respectively.

xv)The frequency band that resides on the left hand side of the LH transmission peak [see figure 3.4.5] already exhibited very low

transmission values. The corresponding NRI values for this specific band turn out to be artificially negative, where $\mathrm{Re}(\mu) > 0$.

xvi) The NRI bandwidth is extended with the decreasing a_s values in analogy with the statement (iv).

In the second part of the study, fishnet layers are stacked in the form of a wedge [see figure 3.4.1]. The assembled metamaterial prism is investigated in the 2D-*XY* Scan simulations and measurements. In one side of the ongoing discussion, the origin of the negative refraction is attributed to the loss mechanism. However, the LH behaviour is observed in the simulations for our case such that the phase and group velocities are in opposite directions inside the wedge structure where their directions are the same for the fields propagating in air, as implied in statement (ix) [see figure 3.4.7 and 3.4.8]. This puts forward further evidence for the source of the negative refraction. Furthermore, the diffraction analysis of the outgoing beam reveals that diffraction is not the dominant factor in the transmission process. Within the focused frequency range, the contribution of the higher order diffraction beams is not encountered. It is shown that the outgoing beam clearly cannot be formed as a result of diffraction [see figure 3.4.13].

Carrying out the 2D Scan studies for $a_s = 2$ mm through $a_s = 5$ mm, the dependence of NRI on a_s is investigated. The overall performance of the distinct cases has been examined bearing in mind the gathered indications of the previous analyses so far. The field radiated from the wedge shaped fishnet structure is in the form of a directional beam [see figure 3.4.12 and 3.4.14] that enables us to calculate the NRI by using the Snell's Law [see figure 3.4.16]. In both of the simulations and experiments, the outgoing beam is refracted negatively which proves the existence of the NRI in the LH frequency band [see figure 3.4.12, 3.4.14 and 3.4.15].

xvii) In the 2D-*XY* scan studies, the beam moves in the counter-clockwise direction for the increasing frequency values, which in turn implies that the absolute NRI is decreasing for the frequency range of our interest. Thus, the operational NRI band lies in the right hand side of the LH transmission peak [see movie files 13-16 and 17-20 of ref. 117].

xviii) A fading effect is evident for $a_s = 2$ mm after a propagation distance of about 50 cm in the simulation results as well as in the experimental results which partially suffer from the misalignments in the fishnet layers. Further simulations for the case of $a_s = 2$ mm verify that this case is the most sensitive scenario to the possible misalignments in the experiments.

xix) For other cases, well defined outgoing and negatively refracted beams are observed. As for the RH band, the outgoing beams are positively refracted with positive refractive index values close to 0, which produces outgoing beams parallel to the output surface normal.

xx) Relying on the statement (i), the lower a_s valued wedge configurations are expected to yield higher transmission values. However, the thicker portions of wedge structure can contribute to the transmission for smaller a_s value due to stronger coupling for the 2D Scan studies [see figure 3.4.8 and movie files 9-12 of ref. 117]. Thus, the statement (vi) comes into play and an opposing mechanism is evident in the transmission figures.

xxi) The statement (v) is verified in the 2D scanning results. Thus, the wedge configuration with the smaller a_s experiences the maximum transmission at higher frequencies.

xxii) It is found in the retrieval studies that the operational bandwidth is larger for smaller a_s due to enhanced coupling [statement (xvi)] while the addition of the extra layers restricted the operational bandwidth [statement (vii)]. Thus, the operational bandwidth has two opposing contributing effects.

xxiii) The wedge configuration can be interpreted as a combination of columns with different lengths. In the 1-D TL approach, these columns have different propagation constants [in accordance with the statement (xi)], in turn yielding different NRI values. More number of columns is involved in the transmission for the $a_s = 2$ mm case. Compliant with the statement (xiv), the wedge structure possesses a wide range of NRI variation for $a_s = 2$ mm in comparison to other cases, which brings the necessity for further attention in interpreting the results that are obtained with the wedge structures.

In the end, we have made use of the whole information that the building blocks of the wedge configuration provide for us in terms of the retrieval analyses and transmission results. All of these results have been pursued in order to grasp the performance characteristics of the wedge shaped fishnet arrangements and compare their significant features with the variation of the lattice separation along the propagation distance. Accordingly, the NRI is apparently not caused by the loss induced prism effects namely the geometrical effects, but such geometrical effects give birth to peculiarities for different lattice spacings in the performance characteristics of the wedge shaped structure. Ideally, the lattice spacing is desired to be assigned to smaller values in terms of the operational wavelength for the metamaterials. Yet, as we have outlined in this section the LH behaviour is not obsolete for such conditions with smaller a_s values, but the self-consistent variation in the performance characteristics that

were valid for larger a_s values are dramatically altered. Therefore, one has to be cautious while applying a direct homogenization based on the metamaterial slab results to model the frequency response of the wedge shaped fishnet metamaterials even at normal incidence angle. Nevertheless, the results of our study suggest that it is possible to observe an agreement up to a certain degree between the estimated NRI values coming from the 2D wedge results (experimental and numerical) and the homogenization approach for which the retrieval procedure is utilized for certain a_s values [see figure 3.4.17].

Chapter 4

Conclusion

Controlling the propagation of Electromagnetics Waves is imperative in the photonic applications. The periodic modulation of the permittivity in the case of PCs and/or modulation of both of the permittivity and permeability as in the case of Metamaterials provide with a means for the controlling the transmission of the electromagnetic waves. This thesis reports the studies on PCs which enable focusing, waveguiding, spatially filtering, demultiplexing of Electromagnetics waves as well as the negative phase velocity arising from the *backward* properties due to the special designs in the PCs. In addition, the aspects of backward propagation accompanied with the Left-Handed behavior in Metamaterials are examined. Chapter 2 is dedicated to the efforts in PCs while the studies in metamaterials are given in Chapter 3.

Mentioning the basics of PCs in Section 2.1, we have described a novel approach to implement graded index structures using two dimensional PC in Section 2.2. The lattice spacing along the transverse direction to propagation is altered and we show, both theoretically and experimentally, that such a spatial perturbation is an effective way to obtain graded index PC (GRIN PC). The

response of the structure to spatially wide incident beams is investigated and strong focusing behavior is observed. At 18 GHz, the focused *E*-field distribution is observed at the exit side of the PC. The measured focus distance to the exit-side surface of the PC is 6mm ($\lambda/2.8$). Besides, the large spot size conversion ratio can be attainable and is mainly limited by the finite size of the structure. For an input pulse which has a FWHM value of 17.5*a*, the measured spot size conversion ratio is 7.4. The designed GRIN PC shows promise for use in optical systems that require compact and powerful focusing elements compared to the traditional bulky lenses.

In Section 2.3, the GRIN PC configuration was placed at the input side of a photonic crystal waveguide (PCW) in order to efficiently couple the light waves into the waveguide. We compared the transmission efficiencies of light in the absence and presence of the GRIN PC structure. We report a significant improvement in coupling when the GRIN PC is incorporated with the PCW. The intensity profiles were obtained by carrying out the experiments at microwave frequencies. Finite Difference Time Domain (FDTD) based simulations were found to be in good agreement with our experimental results. In these simulations, the improvement when the GRIN PC is employed as the coupling block is expected as 6.5 *dB* in comparison to the case when there is no coupler. The measured improvement (5 *dB*) is in agreement with the simulation result.

In Section 2.4, spatial filtering is demonstrated at beam-type excitations by utilizing finite-thickness slabs of two-dimensional dielectric PCs owing to the exotic Fabry-Perot resonances that are preserved over a wide angle of incidence variation. Bandstop and dual-bandpass filtering effects are illustrated theoretically and the corresponding filters are realized in the microwave experiments by using square-lattice PCs. It is shown that the basic transmission features that were observed earlier for a plane-wave illumination are also recognizable at beam-type excitations. The proposed spatial filtering mechanism exhibits a directional beaming. The desired widths and the locations of the pass and stop bands are

attainable in the angle domain with a proper choice of the operating frequency for the given excitation characteristics.

In Section 2.5, PC with a surface defect layer (made of dimers) is studied in the microwave regime. The dispersion diagram is obtained with the Plane Wave Expansion Method. The dispersion diagram reveals that the dimer-layer supports a surface mode with negative slope. Two facts are noted: First, a guided (bounded) wave is present, propagating along the surface of the dimer-layer. Second, above the light line, the fast traveling mode couple to the propagating spectra and as a result a directive (narrow beam) radiation with backward characteristics is observed and measured. In this leaky mode regime, symmetrical radiation patterns with respect to the normal to the PC surface are attained. Beam steering is observed and measured in a 70° angular range when frequency ranges in the 11.88-13.69GHz interval. Thus, a PC based surface wave structure that acts as a frequency dependent leaky wave antenna is presented. Angular radiation pattern measurements are in agreement with those obtained via numerical simulations that employ the FDTD method. Finally, the backward radiation characteristics that in turn suggest the existence of a backward leaky mode in the dimer-layer are experimentally verified using a halved dimer-layer structure.

In Chapter 3, the studies about Metamaterials are given. After providing with the basics of the negative constitutive parameters and negative refraction in Sections 3.1 to 3.3 in Section 3.4, for a fishnet metamaterial, the correspondence between the two sets of information to obtain NRI values is explained: a) The first set is found by the simulations and experiments where the retrieval analysis is performed for the fishnet patterned dielectric layers. The simulation of transmission and reflection as well as the retrieval results obtained by employing the S21 and S11 coefficients are supported by the measurement results. b) The second set is found by the two-dimensional scan experiments and simulations employing the wedge structure consisting of the same type of fishnet layers. In the search for the physical origins of the left-handed transmission band for the

subwavelength aperture array, it is discussed that the fishnet layers behave as an LC resonator as well as a TEM waveguide and a 1D transmission line at magnetic resonance frequency ω_m. The dependence of the retrieval results on the lattice separation and number of layers are investigated. The conclusions from the examination of the subwavelength arrays and the parametrical retrieval analyses are merged in order to understand the negative refraction in the wedge shaped fishnet arrangements with a consideration on the limits of the homogenization.

As it was pointed out, the control over the propagation of the electromagnetic waves in the optical integrated circuits is a contemporary research topic. In an optical integrated circuit, various components for different functions are needed. In this sense, waveguides, steering or demultiplexing blocks, lenses, polarizers can be mentioned. Besides, different filtering blocks are handy where the filters may rely on spatial and/or frequency selectivity as well as distinguishing response for the polarization of the incoming electromagnetic waves, shortly *light*. Although the studies are carried out in the Microwave regime in this thesis, due to the scalability property of the Maxwell Equations, similar results can be obtained in different frequency regimes, specifically in the infrared and the visible zone. However, the careful choice of the dielectric and metal becomes crucial in the optical applications since the loss mechanism becomes more evident as the frequency is increased. The demonstration of the applications in the optical domain is beyond the scope of this thesis. Nevertheless, in an optical circuit, light should be transmitted from one part to another part of the circuit without significant loss. Besides, light should not be scattered and should preserve its spatial width during transmission. This can readily be achieved semiconductor waveguides. Alternatively, a lens design based on photonic crystals is demonstrated in conjunction with a low loss photonic crystal waveguide in this thesis. The graded index photonic crystal lens which is obtained by spatial modulation of the period provides with advantages

as it can replace the bulky optical lenses while being compatible with the photonic crystal waveguide, where the integrated optical circuit manufacturing is also feasible. The thesis also covers the applications of different kinds of filters where spatial filtering and frequency dependent demultiplexing and steering are demonstrated. In turn, the basics of the spatial filtering can be used to achieve and to explain the diode like behaviour in photonic crystals in the transmission of light. Thus, unidirectionality can be obtained by controlling the propagation of light to replace the diodes which allows current due to electron motion in only a defined direction in the integrated electronic circuits. The signatures of backward waves as well as negative refraction are observed in the reported photonic crystal research in the thesis. On the other hand, the left handed behavior in the metamaterials which is accompanied with the backward (negative) phase velocity can also be utilized to achieve negative refraction. The refraction that is observed in nature is called as positive refraction where the resolution of an optical microscope is limited by the diffraction limit. By means of negative refraction that is demonstrated in the third chapter of this thesis special effects like super resolution, superprism, and subwavelength imaging beyond diffraction limit becomes possible. We have examined and characterized the left handed properties of the fishnet metamaterial which enables a more suitable geometry especially for manufacturing designs that operate in the optical wavelengths in comparison to previously studied metamaterials like SRRs, cut-wires etc. In conclusion, the thesis reports various efforts in photonic crystals and metamaterials. The findings of these efforts are applicable in the optical wavelengths and ready to be adapted in the integrated optical circuits.

Thus, the future work includes realization of photonic crystals and matematerials which operate in the infrared and visible regime to replace the conventional bulky lenses, waveguides, as well as electronic diodes and filters. Besides, it is possible to use the metamaterials for super resolution in nuclear

magnetic imaging and/or to achieve subwavelength focusing to realize media like DVDs, CDs with enhanced memory capabilities.

Recent efforts on PCs involve the hybridization of PCs with graphene which is accompanied with high nonlinearity. One-atom thick carbon layer which is initially a non-active structure can be turned into an active medium that generated microwave signals enabling parametric wavelength conversion at telecommunication wavelengths. That is, new optical frequencies are generated through nonlinear mixing of two electromagnetic fields at low operating energies. It allows reduced energy per information bit. The enhanced optical nonlinearity which is required for the digital on/off two-state switching and memories may lead to all-optical data processing platfrom and low power photonic integrated circuits [194]. In another recent study, high temperature PC made of metals like tungsten and tantalum is produced. That these metals can stand temperatures as high as 1200 ºC enables devices for solar-thermal conversion or solar-chemical conversion, radioisotope-powered devices, hydrocarbon-powered generators or components to harvest energy from waste heat at powerplants or industrial facilities. In this scheme, radioisotope thermal generators generate heat from the decay of radioactive material (for example, plutonium). PCs that can survive high temperatures can be tuned to absorb infrared radiation. The captured energy can then be converted into electricity via a thermocouple pair [195]. Optoelectronically active 3D photonic crystal is another topic that draws attention of the researchers. Such a development could enable new advancements for solar cells, lasers, metamaterials. In contrast to previous attempts where the manufactured 3D PCs were only optically active (i.e., they can’t turn electricity to light or vice versa). In [196], tiny alumina spheres packed together are used a template and the internal vacancies are filled with GaAs by an exitaxial growth. Then, removing the template (alumina spheres), a complex, porous 3D structure of single-crystal semiconductor is obtained. Thus, an LED obtained by means of electrical driven 3D PC structure

is demonstrated. The key discovery here was the growth of single-crystal semiconductor through this complex template. Devices made of such photonic crystals can compensate for absorptive loss by adding gain, making the structure lossless and enabling large-scale volumes that are capable of negative refraction and cloaking.

Following the terms mentioned above, there is on-going research to come up with metamaterials which satisfy the following three properties: Firstly, these metamaterials should operate in the optical regime. This goal is partially satisfied by the manufactured designs that operate at 439THz [197]. Secondly, the new designs should be three dimensional (3D) rather than being (1D) as it is reported in the metamaterials chapter of this thesis. Thirdly, these 3D metamaterials which operate at optical frequencies should attain low loss values, which puts forward three main classes of challenge for the future metamaterials. The increased number of layers to achieve 3D metamaterials is accompanied with the question of optimum number of layers, which should be carefully taken into account as stressed out in the concept of parametric analysis section of this thesis. Similar considerations about the number of layers and periodicity will arise for optical metamaterials as those appearing in the fishnet metamaterial which is designed to operate in the microwave regime in the thesis. The fishnet structure is suitable to be manufactured in the optical regime by using the standart electron-beam lithography, focused ion beam lithography, intereference lithography and nanoimprint lithography techniques. However, for exotic optical activity like chirality or circular dichroism the internal volume of the unit cell has to be processed. This can be achieved by direct laser writing (DLW) which has a resolution of 50nm [198]. However for the time being large scale bulk metamaterial production cannot be achieved with DLW as the height of the samples that can be processed is limited by the DLW process itself. Alternatively, membrane projection lithography can be used. Its current resolution is suitable for applications in the deep infrared regime (~10 μm) and

needs to be improved [199]. As for to overcome the loss occurring in metallic metamaterials, low loss, off-resonant dielectric structures are offered. According to the Mie theory, dielectric spheres and cylinders can be utilized to achieve negative permeability [200]. With proper adjustment, the two set combination of spheres with different radii, or different permittivity provide with negative permittivity and negative permeability resonances, while negativity of each constitutive parameter is arising due to one set of the arrangement. However, these resonances are very narrow and it is still a challenge to achieve a wide negative refraction band. Despite the demonstration of isotropic negative refractive index 3D metamaterial which employs purely dielectric spheres in the microwave [201], the application in the optical regime is yet to be reported. There are other studies considering combinations of materials in the search for isotropic 3D metamaterials: In [202], dielectric spheres are embedded in a negative permeability medium composed of metallic wires. Alternatively, dielectic spheres with negative permeability are coated by thin layer of Drude metal which provides with negative permittivity and yielding negative refractive index at infrared [203]. The realization of low loss dielectric isotropic 3D metamaterials is still possible even in the random or non-periodic arrangements of dielectric spheres since the electric and magnetic dipole resonances of dielectric spheres are preserved while providing with refractive negative refractive index [204]. Another recent challenge in metamaterials aims to reduce the losses. A practical transmission value of around 90% per layer in metamaterials diables the 3D application if the number of layers is increased upto hundred (or above) since the transmission is scaled down to $0.9^{100} \approx 0.00003$ with such number of layers. The current efforts include to use of dielectric spacer layer that is doped with dye molecules being pumped by optical picosecond pulses as a gain medium [205] or utilizing semiconductor gain in SRRs [206]. Nevertheless, these efforts provide with limited loss compensation

and further research to overcome the loss issue is needed. Further summary of the recent efforts on metamaterials can be seen in [207].

To sum up, the adventure of metamaterials starting from the microwave regime has reached to a destination where the operation as a 3D bulk structure (of low physical dimensions) is available at optical frequencies, though only for certain direction and polarization. Further efforts will be towards manufacturing bulk metamaterials in large scale. Together with the opportunity that the metamaterials neither reflect nor transmit the electromagnetic waves at a limited frequency band for a broad incidence angle [208, 209], the large scale metamaterials can open new possibilities in solar energy harvesting [210] and detector technology which especially important for medical imaging.

Thus, it is seen that the current trend in Photonic Crystals and Meamaterials towards the realization of low loss 3D isotropic structures that operate at optical frequencies. Currently, not all of these properties are achieved in the same design and it is still a challenge to resolve the issues arising in the efforts towards the manufacturing of devices. From this perspective, the fields of Photonic Crystals and Metamaterials are still promising. Just as a notice, I believe it is crucial that young researchers that to do graduate study on these subjects have better keep in mind to improve their knowledge in the analytical and theoretical aspects while they are becoming competent on manufacturing of these devices, i.e., not to be satisfied only being able or not to reserve most of their time during the graduate study to manufacture the nanoscale devices in the cleanroom environment but improving their analytical skills throughout the graduate study as well becomes more beneficial in the consideration of further steps of their academic career.

BIBLIOGRAPHY

[1] E. Yablonovitch, "Inhibited spontaneous emission in solid-state physics and electronics," *Phys. Rev. Lett*. 58, pp. 2059-2062, 1987.

[2] S.Y. Lin, V.M Hietala, L. Wang, E.D. Jones, "Highly dispersive photonic band-gap prism," *Opt. Lett.* 21, pp. 1771-1773, 1996.

[3] H. Kosaka, T. Kawashima, A. Tomita, M. Notomi, T. Tamamura, T. Sato and S. Kawakami, "Superprism phenomena in photonic crystals," *Phys. Rev. B* 58, R10096-R10099, 1998.

[4] M. Notomi, "Theory of light propagation in strongly modulated photonic crystals: Refractionlike behavior in the vicinity of the photonic band gap," *Phys. Rev. B* 62, pp. 10696-10705, 2000.

[5] J. Witzens, M. Loncar and A. Scherer, "Self-collimation in planar photonic crystals," *IEEE J. Sel. Top. Quantum Electron*. 8, pp. 1246-1257, 2002.

[6] L. Wu, M. Mazilu and T. F. Krauss, "Beam Steering in Planar-Photonic Crystals: From Superprism to Supercollimator," *IEEE J. Lightwave Technol.* 21, pp. 561-566, 2003.

[7] A. R. McGurn,"Intrinsic localized modes in photonic crystal circuits," *Chaos* 13, pp. 754-765, 2003.

[8] S. Fan, P. R. Villeneuve, J. D. Joannopoulos, H. A. Hauss, "Channel drop tunneling through localized states," *Phys. Rev. Lett.* 80, pp. 960-963, 1998.

[9] A. Mekis, J. C. Chen, I. Kurand, S. Fan, P. R. Villeneuve and J. D. Joannopolous, "High transmission through sharp bends in photonic crystal waveguides," *Phys. Rev. Lett*. 77, pp. 3787-3790, 1996.

[10] H. Kurt and D. S. Citrin, "Photonic-crystal heterostructure waveguides," *IEEE J. Quantum Electron.*, vol. 43, pp. 78-84, 2007.

[11] S. H. G. Teo, A. Q. Liu, M. B. Yu and J. Singh, "Fabrication and demonstration of square lattice two-dimensional rod-type photonic band

gap crystal optical intersections," *Photonics Nanostruct. Fundam. Appl*. 4, pp. 103-115, 2006.
[12] G. Manzacca, D. Paciotti, A. Marchese, M. S. Moreolo and G. Cincotti, "2D photonic crystal cavity-based WDM multiplexer," *Photonics Nanostruct. Fundam. Appl*. 5, pp. 164-170, 2007.
[13] V. G. Veselago, "The electrodynamics of substances with simultaneously negative values of ε and μ," *Sov. Phys. Usp.* 10, 1968, pp. 509-514.
[14] J. B. Pendry, "Negative Refraction Makes a Perfect Lens," *Phys. Rev. Lett.* 85, pp. 3966-3969, 2000.
[15] D. R. Smith, W. Padilla, D. C. Vier, S. C. Nemat-Nasser and S. Schultz, "Composite Medium with Simultaneously Negative Permeability and Permittivity," *Phys. Rev. Lett.* 84, pp. 4184-4187, 2000.
[16] J. B. Pendry, A. J. Holden, D. J. Robins, W. J. Stewart, "Magnetism from conductors and enhanced nonlinear phenomena," *IEEE Trans. On Microwave Theory and Tech*. 47, pp. 2075-2084, 1999.
[17] J. B. Pendry, A. J. Holden, W. J. Stewart, I. Youngs, "Extremely Low Frequency Plasmons in Metallic Mesostructures," *Phys. Rev. Lett*. 76, pp. 4773-4776, 1996.
[18] R. A. Shelby, D. R. Smith and S. Schultz, "Experimental verification of a negative index of refraction," *Science* 292, pp. 77-79, 2001.
[19] X. Zhang and Z. Liu, "Superlenses to overcome the diffraction limit," *Nature Materials* 7, pp. 435-441, 2008.
[20] Z. W. Liu, H. Lee, Y. Xiong, C. Sun and X. Zhang, "Far-field optical hyperlens magnifying sub-diffraction-limited objects," *Science* 315, pp. 1686-1686, 2007.
[21] I. I. Smolyaninov, Y. J. Hung and C. C. Davis, "Magnifying superlens in the visible frequency range," *Science* 315, pp. 1699-1701, 2007.
[22] E. Cubukcu, K. Aydin, E. Ozbay, S. Foteinopoulou and C. M. Soukoulis, "Subwavelength Resolution in 2D Photonic-Crystal-Based Superlens," *Phys. Rev. Lett*. 91, pp. 207401 (4 pages), 2003.
[23] Z. Y. Li and L. L. Lin, "Evaluation of lensing in photonic crystal slabs exhibiting negative refraction," *Phys. Rev. B* 68, pp. 245110 (7 pages), 2003.
[24] R. Meisels, R. Gaji´c, F. Kuchar and K. Hingerl, "Negative refraction and flat-lens focusing in a 2D square-lattice photonic crystal at microwave and millimeter wave frequencies," *Opt. Express* 14, pp. 6766-6777, 2006.
[25] E. Foca, H. Föll, J. Carstensen, V. V. Sergentu, I. M. Tiginyanu, F. Daschner and R. Knöchel, "Strongly frequency dependent focusing efficiency of a concave lens based on two-dimensional photonic crystals," *Appl. Phys. Lett.* 88, pp. 011102 (3 pages), 2006.
[26] I. Bulu, H. Caglayan, K. Aydin and E. Ozbay, "Study of the field emitted by a source placed inside a two dimensional left-handed metamaterial," *Opt. Lett.* 32, pp. 850-852, 2007.

[27] K. Aydin, I. Bulu and E. Ozbay, "Subwavelength resolution with a negative-index metamaterial superlens," *Appl. Phys. Lett*. 90, pp. 254102 (3 pages), 2007.
[28] E. Centeno and D. Cassagne, "Graded photonic crystals," *Opt. Lett.* 30, pp. 2278-2280, 2005.
[29] E. Centeno, D. Cassagne and J. P. Albert, "Mirage and superbending effect in two-dimensional graded photonic crystals," Phys. Rev. B 73, pp. 235119 (5 pages), 2006.
[30] F. S. Roux and I. De Leon, "Planar photonic crystal gradient index lens, simulated with a finite difference time domain method," *Phys. Rev. B* 74, pp.113103 (4 pages), 2006.
[31] H. Kurt and D. S. Citrin, "Graded index photonic crystals," *Opt. Express* 15, pp. 1240–1253, 2007.
[32] E. H. Khoo, A. Q. Liu, T. H. Cheng, J. Li and D. Pinjala, "Light focusing via Rowland concave surface of photonic crystal," *App. Phys. Lett*. 91, pp. 221105 (3 pages), 2007.
[33] A. Taflove, *Computational Electrodynamics - The Finite-Difference Time-Domain Method* (Norwood, Massachusetts: Artech House, 2000).
[34] C. M. Soukoulis, "The history and a review of the modelling and fabrication of photonic crystals," *Nanotechnology* 13, pp. 420-423, 2003.
[35] P. Russel, "Photonic Crystal Fibers," *Science* 299, pp. 358-362, 2003.
[36] R. D. Meade, A. Devenyi, J. D. Joannopoulos, O. L. Alerhand, D. A. Smith and K. Kash, "Novel applications of photonic band gap materials: Low-loss bends and high Q cavities," *J. Appl. Phys.* 75, pp. 4753-4755, 1994.
[37] B. Temelkuran and E. Ozbay, "Experimental demonstration of photonic crystal based waveguides," *Appl. Phys. Lett.* 74, pp. 486-488, 1999.
[38] Y. Xu, R. K. Lee and A. Yariv, "Asymptotic analysis of Bragg fibers," *Opt. Lett*. 25, pp. 1756-1758, 2000.
[39] J. Bauer and S. John, "Broadband optical coupling between microstructured fibers and photonic band gap circuits: Two-dimensional paradigms," *Phys. Rev. A* 77, 013819 (14 pages), 2008.
[40] D. Taillaert, W. Bogaerts, P. Bienstman, T. F. Krauss, P. V. Daele, I. Moerman, S. Verstuyft, K. D. Mesel and R. Baets, "An out-of-plane grating coupler for efficient butt-coupling between compact planar waveguides and single-mode fibers," *IEEE J. Quantum Electron*. 38 (7) pp. 949-955, 2002,.
[41] D. W. Prather, J. Murakowski, S. Shi, S. Venkataraman, A. Sharkawy, C. Chen and D. Pustai, "High-efficiency coupling structure for a single-line-defect photonic-crystal waveguide," *Opt. Lett*. 27 (18), pp. 1601-1603, 2002.

[42] T. Dillon, J. Murakowski, S. Shi and D. Prather, "Fiber-to-waveguide coupler based on the parabolic reflector," *Opt. Lett*. 33 (9), pp. 896-898, 2008.

[43] C. W. Chang, S. C. Cheng and W. F. Hsieh, "High-efficiency coupling between external and photonic crystal waveguides by longitudinally shifting waveguide junctions," *Opt. Commun.* 242, pp. 517-524, 2004.

[44] A. A. Green, E. Istrate and E. H. Sargent, "Efficient design and optimization of photonic crystal waveguides and couplers: The Interface Diffraction Method," *Opt. Express* 13 (19), pp. 7304-7318, 2005.

[45] P. Sanchis, J. Garcia, J. Marti, W. Bogaerts, P. Dumon, D. Taillaert, R. Baets, V. Wiaux, J. Wouters and S. Beckx, "Experimental demonstration of high coupling efficiency between wide ridge waveguides and single-mode photonic Crystal waveguides," *IEEE Photon. Technol. Lett*. 16, pp. 2272-2274, 2004.

[46] A. Mekis and J. D. Joannopoulos, "Tapered couplers for efficient interfacing between dielectric and photonic crystal waveguides," *J. Lightw. Technol*. 19, 6, pp. 861-864, 2001.

[47] A. Hakansson, P. Sanchis, J. S. Dehesa and J. Marti, "High-efficiency defect-based photonic-crystal tapers designed by a genetic algorithm," *J. Lightw. Technol.* 23, 11, pp. 3881-3888, 2005.

[48] P. Bienstman, S. Assefa, S. G. Johnson, J. D. Joannopoulos, G. S. Petrich and L. A. Kolodziejski, "Taper structures for coupling into photonic crystal slab waveguides," *J. Opt. Soc. Am. B* 20 (9), pp. 1817-1821, 2003.

[49] E. H. Khoo, A. Q. Liu and J. H. Wu, "Nonuniform photonic crystal taper for high-efficiency mode coupling," *Opt. Express* 13, 20, pp. 7748-7759, 2005.

[50] A. Talneau, P. Lalanne, M. Agio and C. M. Soukoulis, "Low-reflection photonic-crystal taper for efficient coupling between guide sections of arbitrary widths," *Opt. Lett.* 27 (17), pp. 1522-1524, 2002.

[51] P. Pottier, M. Gnan and R. M. De La Rue, "Efficient coupling into slow-light photonic crystal channel guides using photonic crystal tapers," *Opt. Express* 15, 11, pp. 6569-6575, 2007.

[52] J. P. Hugonin, P. Lalanne, T. P. White and T. F. Krauss, "Coupling into slow-mode photonic crystal waveguides," *Opt. Lett.* 32, 18, pp. 2638-2640, 2007.

[53] S. G. Johnson, P. Bienstman, M. A. Skorobogatiy, M. Ibanescu, E. Lidorikis and J. D. Joannopoulos, "Adiabatic theorem and continuous coupled-mode theory for efficient taper transitions in photonic crystals," *Phys. Rev. E* 66, pp. 066608 (15 pages), 2002.

[54] M. Qiu, K. Azizi, A. Karlsson, M. Swillo and B. Jaskorzynska, "Numerical studies of mode gaps and coupling efficiency for line-defect waveguides in two-dimensional photonic crystals," *Phys. Rev. B* 64, 155113 (5 pages), 2001.

[55] D. W. Prather, S. Shi, j. Murakowski, G. J. Schneider, A. Sharkawy, C. Chen, B. L. Miao and R. Martin, "Self-collimation in photonic crystal structures: a new paradigm for applications and device development," *J. Phys. D.* 40, pp. 2635-2651, 2007.

[56] H. Kosaka, T. Kawashima, A. Tomita, M. Notomi, T. Tamamura, T. Sato and S. Kawakami, "Self-collimating phenomena in photonic crystals," *Appl. Phys. Lett*. 74, pp. 1212-1214, 1999.

[57] H. Kurt and D. S. Citrin, "A novel optical coupler design with graded-index photonic crystals," *IEEE Photon. Technol. Lett*. 19, pp. 1532-1534, 2007.

[58] H. Kurt, E. Colak, O. Cakmak, H. Caglayan and E. Ozbay, "The focusing effect of graded index photonic crystals," *Appl. Phys. Lett*. 93, pp. 171108 (3 pages), 2008.

[59] D. Schurig and D. R. Smith, "Spatial filtering using media with indefinite permittivity and permeability tensors," *Appl. Phys. Lett*. 82, pp. 2215-2217, 2003.

[60] I. Moreno, J.J. Araiza and M. Avendano-Alejo, "Thin-film spatial filters," *Opt. Lett.* 30, pp. 914-916, 2005.

[61] A. Sentenac and A.-L. Fehrembach, "Angular tolerant resonant grating filters under oblique incidence," *J. Opt. Soc. Am. A* 22, pp. 475-480, 2005.

[62] L. Dettwiller and P. Chavel, "Optical spatial frequency filtering using interferences," *J. Opt. Soc. Am. A* 1, pp. 18-27, 1984.

[63] O.F. Siddiqui and G. Eleftheriades, "Resonant modes in continuous metallic grids over ground and related spatial-filtering applications," *J. Appl. Phys*. 99, pp. 083102 (6 pages), 2006.

[64] Y.J. Lee, J. Yeo, R. Mittra and W. S. Park, "Application of electromagnetic bandgap (EBG) superstrates with controllable defects for a class of patch antennas as spatial angular filters," *IEEE Trans. Antennas Propag.* 53, 224-234, 2005.

[65] A.E. Serebryannikov, A.Y. Petrov and E. Ozbay, "Toward photonic crystal based spatial filters with wide angle ranges of total transmission," *Appl. Phys. Lett*. 94, pp. 181101 (3 pages), 2009.

[66] K. Staliunas and V. J. Sanchez-Morcillo, "Spatial filtering of light by chirped photonic crystals," *Phys. Rev. A* 79, pp. 053807 (6 pages), 2009.

[67] Z. Luo, Z. Tang, Y. Xiang, H. Luo and S. Wen, "Polarization-independent low-pass spatial filters based on one-dimensional photonic crystals containing negative-index materials," *Appl. Phys. B* 94, pp. 641-646, 2009.

[68] P.V. Usik, A.E. Serebryannikov and E. Ozbay, "Spatial and spatial-frequency filtering using one-dimensional graded-index lattices with defects," *Opt. Commun*. 282, pp. 4490-4496, 2009.

[69] R. Rabady and I. Avrutsky, "Experimental characterization of simultaneous spatial and spectral filtering by an optical resonant filter," *Opt. Lett.* 29, pp. 605-607, 2004.
[70] B.T. Schwartz and R. Piestun, "Total external reflection from metamaterials with ultralow refractive index," *J. Opt. Soc. Am. B* 20, pp. 2448-2453, 2003.
[71] K. Sakoda, *Optical Properties of Photonic Crystals* (Springer-Verlag, Berlin Heidelberg, 2005).
[72] P.A. Belov, C.R. Simovski and P. Ikonen, "Canalization of subwavelength images by electromagnetic crystals," *Phys. Rev. B* 71, pp. 193105 (4 pages), 2005.
[73] C. Luo, S.G. Johnson, J.D. Joannopoulos and J.B. Pendry, "All-angle negative refraction without negative effective index," *Phys. Rev. B* 65, pp. 201104 (4 pages), 2002.
[74] T.P. White, C.M. de Sterke, R.C. McPhedran and L.C. Botten, "Highly efficient wide-angle transmission into uniform rod-type photonic crystals," *Appl. Phys. Lett*. 87, pp. 111107 (3 pages), 2005.
[75] B. Temelkuran and E. Ozbay, J. P. Kavanaugh, G. Tuttle and K. M. Ho, "Resonant cavity enhanced detectors embedded in photonic crystals," *Appl. Phys. Lett*. 72, pp. 2376-2378, 1998.
[76] E. Ozbay, E. Michel, G. Tuttle, R. Biswas and K. M. Ho, J. Bostak and D. M. Bloom, "Double-etch geometry for millimeter-wave photonic band-gap crystals," *Appl. Phys. Lett*. 65, pp. 1617-1619, 1994.
[77] E. Ozbay, G. Tuttle, J.S. McCalmont, M. Sigalas, R. Biswas, C. M. Soukoulis and K. M. Ho, "Laser-micromachined millimeter-wave photonic bandgap cavity structures,"*Appl. Phys. Lett*. 67, pp. 1969-1971, 1995.
[78] C. A. Balanis, *Antenna Theory: Analysis and Design* (Wiley, New York, 2005).
[79] B. E. A. Saleh and M. C. Teich, *Fundamentals of Photonics* (Wiley, New York, 1991).
[80] E. Colak, H. Caglayan, A.O. Cakmak, A.D. Villa, F. Capolino and E. Ozbay, "Frequency dependent steering with backward leaky waves via photonic crystal interface layer," *Opt. Express* 17, pp. 9879-9890, 2009.
[81] I. Bulu, H. Caglayan and E. Ozbay, "Beaming of light and enhanced transmission via surface modes of photonic crystals," *Opt. Lett*. 30, pp. 3078-3080, 2005.
[82] E. Cubukcu, K. Aydin, E. Ozbay, S. Foteinopoulou and C.M. Soukoulis, "Electromagnetic waves: Negative refraction by photonic crystals," *Nature* 423, pp. 604-605, 2003.
[83] E. Cubukcu, K. Aydin, E. Ozbay, S. Foteinopolou and C.M. Soukoulis, "Subwavelength Resolution in a Two-Dimensional Photonic-Crystal-Based Superlens," *Phys. Rev. Lett.* 91, pp. 207401 (4 pages), 2003.

[84] M.S. Kumar, S. Menabde, S. Yu and N. Park, "Directional emission from photonic crystal waveguide terminations using particle swarm optimization," *J. Opt. Soc. Am. B* 27, pp. 343-349, 2010.

[85] S. K. Morrison and Y. S. Kivshar, "Engineering of directional emission from photonic-crystal waveguides," *Appl. Phys. Lett*. 86, pp. 081110 (3 pages), 2005.

[86] E. Moreno, F. J. Garcia-Vidal and L. Martin-Moreno, "Enhanced transmission and beaming of light via photonic crystal surface modes," *Phys. Rev. B* 69, pp. 121402 (4 pages), 2004.

[87] P. Kramper, M. Agio, C. M. Soukoulis, A. Birner, F. Muller, R. B. Wehrspohn, U. Gosele and V. Sandoghdar, "Highly Directional Emission from Photonic Crystal Waveguides of Subwavelength Width," *Phys. Rev. Lett.* 92, pp. 113903 (4 pages), 2004.

[88] D. Tang, L. Chen and W. Ding, *Appl. Phys. Lett*. 89, "Efficient beaming from photonic crystal waveguides via self-collimation effect," pp. 131120 (3 pages), 2006.

[89] H. Caglayan, I. Bulu and E. Ozbay, "Highly directional enhanced radiation from sources embedded inside three-dimensional photonic crystals," *Opt. Express.* 13, pp. 7645-7652, 2005.

[90] E. Yablonovitch, T.J. Gmitter and K. M. Leung, "Photonic band structure: The face-centered-cubic case employing nonspherical atoms," *Phys. Rev. Lett*. 67, pp. 2295-2298, 1991.

[91] S. John, "Strong localization of photons in certain disordered dielectric superlattices," *Phys. Rev. Lett*. 58, pp. 2486-2489, 1987.

[92] R. D. Meade, K. D. Brommer, A. M. Rappe and J. D. Joannopoulos, "Electromagnetic Bloch waves at the surface of a photonic crystal," *Phys. Rev. B* 44, pp. 10961-10964, 1991.

[93] V. Dinesh Kumar, K. Asakawa, "Transmission and directionality control of light emission from a nanoslit in metallic film flanked by periodic gratings," *Photon. and Nanostruct. Fundam. Appl*. 6, pp. 148–153, 2008.

[94] H. J. Lezec, A. Degiron, E. Devaux, R. A. Linke, L. Martin-Moreno, F. J. Garcia-Vidal and T. W. Ebbesen, "Beaming light from a subwavelength aperture," *Science* 297, pp. 820-822, 2002.

[95] L. Martin-Moreno, F. J. Garcia-Vidal, H. J. Lezec, A. Degiron and T. W. Ebbesen, "Theory of highly directional emission from a single subwavelength aperture surrounded by surface corrugations," *Phys. Rev. Lett.* 90, pp. 167401 (4 pages), 2003.

[96] H. Caglayan, I. Bulu and E. Ozbay, "Off-axis directional beaming via photonic crystal surface modes," *Appl. Phys. Lett*. 92, pp. 092114 (3 pages), 2008.

[97] H. Kosaka, T. Kawashima, A. Tomita, M. Notomi, T. Tamamura, T. Sato and S. Kawakami, "Photonic crystals for micro lightwave circuits using

wavelength-dependent angular beam steering," *Appl. Phys. Lett*. 74, pp. 1370-1372, 1999.

[98] T. Baba and M. Nakamura, "Photonic Crystal Light Deflection Devices Using the Superprism Effect," *IEEE J. Quantum Electron*. 38, pp. 909-914, 2002.

[99] A. Lai, T. Itoh and C. Caloz, "Composite Right/Left-Handed Transmission Line Metamaterials," *IEEE Microwave Mag*. 10, pp. 34-50, 2004.

[100] T. Tamir and A. A. Oliner, "Guided Complex Waves, Part I," *Proc. Inst. Electr. Eng*. 110, pp. 310, 1963.

[101] T. Tamir and A. A. Oliner, "Guided Complex Waves, Part II," *Proc. Inst. Electr. Eng*. 110, pp. 325, 1963.

[102] A. A. Oliner and D. R. Jackson, "Leaky-Wave Antennas," Ch. 11, *Antenna Engineering Handbook*. J. Volakis, Ed., McGraw Hill, 2007.

[103] S. Lim, C. Caloz and T. Itoh, "Metamaterial-Based Electronically Controlled Transmission-Line Structure as a Novel Leaky-Wave Antenna With Tunable Radiation Angle and Beamwidth," *IEEE Trans. Microwave Theory Tech*. 52, pp. 2678-2689, 2004.

[104] D. F. Sievenpiper, "Forward and Backward Leaky Wave Radiation With Large Effective Aperture From an Electronically Tunable Textured Surface," *IEEE Trans. Antennas and Propagat*. 53, pp. 236-247, 2005.

[105] D. Sievenpiper, J. Schaffner, J. J. Lee and S. Livingston, "A Steerable Leaky-Wave Antenna Using a Tunable Impedance Ground Plane," *IEEE Antennas Wireless Propagat. Lett*. 1, pp. 179-182, 2002.

[106] L. Liu, C. Caloz and T. ltoh, "Dominant mode leaky-wave antenna with backfire-to-endfire scanning capability," *Electron. Lett*. 38, pp. 1414-1416, 2002.

[107] T. Ueda, N. Michishita, A. Lai and T. Itoh, "Leaky Wave Antenna Based on Evanescent-Mode Left-Handed Transmission Lines Composed of a Cut-Off Parallel-Plate Waveguide Loaded with Dielectric Resonators," *IEICE Trans. Electron*. 90–C, pp. 1770-1775, 2007.

[108] I. J. Bahl and K. C. Gupta, "A Leaky Wave Antenna Using an Artificial Dielectric Medium," *IEEE Trans. Antennas and Propag*. 22, pp. 119-122, 1974.

[109] D. R. Jackson, J. Chen, R. Qiang, F. Capolino, A. A. Oliner, "The Role of Leaky Plasmon Waves in the Directive Beaming of Light Through a Subwavelength Aperture," *Optics Express* 16, pp. 21271-21281, 2008.

[110] I. Bulu, H. Caglayan and E. Ozbay, "Radiation properties of sources inside photonic crystals," *Phys. Rev. B* 67, pp. 205103 (7 pages), 2003.

[111] I. Bulu, H. Caglayan and E. Ozbay, "Highly directive radiation from sources embedded inside photonic crystals," *Appl. Phys. Lett*. 83, pp. 3263-3265, 2003.

[112] S. Foteinopoulou, M. Kafesaki, E. N. Economou and C. M. Soukoulis, "Backward surface waves at photonic crystals," *Phys. Rev. B* 75, 245116 (6 pages), 2007.
[113] S. Foteinopoulou, G. Kenanakis, N. Katsarakis, I. Tsiapa, M. Kafesaki and E. N. Economou, C. M. Soukoulis, "Experimental verification of backward wave propagation at photonic crystal surfaces," *Appl. Phys. Lett*. 91, 214102 (3 pages), 2007.
[114] F. Capolino, D. R. Jackson and D. R. Wilton, "Fundamental Properties of the Field at the Interface Between Air and a Periodic Artificial Material Excited by a Line Source," *IEEE Trans. Antennas Propagat*. 53, pp. 91–99, 2005.
[115] F. Capolino, D. R. Jackson, D. R. Wilton, "Mode Excitation From Sources in Two-Dimensional EBG Waveguides Using the Array Scanning Method," *IEEE Microwaves and Wireless Comp. Lett.* 15, pp. 49-51, 2005.
[116] *IEEE Stand. Def. Terms Antennas*. IEEE Std. 145-1993, 1993.
[117] E. Colak, A. O. Cakmak, K. Aydin and E. Ozbay, "A discussion on the validity of the homogenization procedure based on a parametrical study of the negative refraction for the wedge-shaped metamaterial made up of dielectric slabs sandwiched by fishnet patterns," - submitted in 2012, under review.
[118] J. B. Pendry, A. J. Holden, D. J. Robbins and W. J. Stewart, "Low frequency plasmons in thin-wire structures," *Journal of Physics: Condensed Matter*, vol. 10, pp. 4785, 1998.
[119] J. B. Pendry, A. J. Holden, D. J. Robbins and W. J. Stewart, "Magnetism from conductors and enhanced nonlinear phenomena," *IEEE Trans. Microwave Theory Tech.*, vol. 47, pp. 2075, 1999.
[120] D. R. Smith, D. C. Vier, N. Kroll and S. Schultz, "Direct calculation of permeability and permittivity for a left-handed metamaterial," *Appl. Phys. Lett.*, vol. 77, pp. 2246-2248, 2000.
[121] J. B. Pendry and D. R. Smith, "Reversing light with negative refraction," *Phys. Today*, vol. 57, issue 6, pp. 37-43, 2004.
[122] D. R. Smith and N. Kroll, "Negative refractive index in left-handed materials," *Phys. Rev. Lett.*, vol. 85, pp. 2933-2936, 2000.
[123] A. Grbic and G. V. Eleftheriades "Growing evanescent waves in negative-refractive-index transmission-line media," *Appl. Phys. Lett*. 82, pp. 1815-1817, 2003.
[124] D. R. Smith, D. Schurig, M. Rosenbluth, S. Schultz, S. A. Ramakrishna and J. B. Pendry, "Limitations on subdiffraction imaging with a negative refractive index slab," *Appl. Phys. Lett*. 82, pp. 1506-1508, 2003.
[125] K. Aydin, Bulu I and E. Ozbay, "Focusing of electromagnetic waves by a left-handed metamaterial flat lens," *Opt. Express* 13, pp. 8753-8759, 2005.

[126] A. K. Iyer and G. V. Eleftheriades, "Negative refractive index metamaterials supporting 2-D waves," *IEEE MTT-S International Microwave Symposium Digest, Seattle, WA* (IEEE, New York, 2002), pp. 1067-1070, 2002.

[127] A. K. Iyer, P. C. Kremer and G. V. Eleftheriades, "Experimental and theoretical verification of focusing in a large, periodically loaded transmission line negative refractive index metamaterial," *Opt. Express* 11, pp. 696-708, 2003.

[128] G. V. Eleftheriades, O. Siddiqui and A. K. Iyer, "Transmission line models for negative refractive index media and associated implementations without excess resonators," *IEEE Microw. Wirel. Compon. Lett*. 13, pp. 51-53, 2003.

[129] A. A. Grbic and G. V. Eleftheriades, "Experimental verification of backward-wave radiation from a negative refractive index metamaterial," *J. Appl. Phys*. 92, pp. 5930-5935, 2002.

[130] J. Huangfu, L. Ran, H. Chen, X. Zhang, K. Chen, T. M. Grzegorczyk and J. A. Kong, "Experimental confirmation of negative refractive index of a metamaterial composed of Ω-like metallic patterns," *Appl. Phys. Lett.* 84, pp. 1537-1539, 2004.

[131] K. Aydin, K. Guven, C. M. Soukoulis and E. Ozbay, "Observation of negative refraction and negative phase velocity in left-handed metamaterials," *Appl. Phys. Lett*. 86, pp. 124102 (3 pages), 2005.

[132] J. Zhou, T. Koschnyh, M .Kafesaki, E. Economou N, J. B. Pendry and C. M. Soukoulis, "Saturation of the magnetic response of split-ring resonators at optical frequencies," *Phys. Rev. Lett*. 95, pp. 223902 (4 pages), 2005.

[133] S. Zhang, W. Fan, N. C. Panoiu, K. J. Malloy, R. M. Osgood and S. R. J. Brueck, "Experimental Demonstration of Near-Infrared Negative-Index Metamaterials," *Phys. Rev. Lett*. 95, pp. 137404 (4 pages), 2005.

[134] V. M. Shalaev, W. Cai, U. K. Chettiar, H. Yuan, A. K. Sarychev, V. P. Drachev and A. V. Kildishev, "Negative index of refraction in optical metamaterials," *Opt. Lett*. 30, pp. 3356-3358, 2005.

[135] J. Zhou, L. Zhang, G. Tuttle, T. Koschnyh and C. M. Soukoulis, "Negative index materials using simple short wire pairs," *Phys. Rev. B* 73, pp. 041101 (4 pages), 2006.

[136] K. Guven, A. O. Cakmak, M. D. Caliskan, T. F. Gundogdu, M .Kafesaki, C. M. Soukoulis and E. Ozbay, "Bilayer metamaterial: analysis of left-handed transmission and retrieval of effective medium parameters," *J. Opt. A: Pure Appl. Opt*. 9, pp. 361-365, 2007.

[137] G. Dolling, C. Enkrich, M. Wegener, C. M. Soukoulis and S. Linden, "Simultaneous negative phase and group velocity of light in a metamaterial," *Science* 312, pp. 892-894, 2006.

[138] G. Dolling, M. Wegener, C. M. Soukoulis and S. Linden, "Negative-index metamaterial at 780 nm Wavelength," *Opt. Lett*. 32, pp. 53-55, 2007.
[139] M .Kafesaki, I. Tsiapa, N. Katsarakis, T. Koschnyh, C. M. Soukoulis and E. N. Economou, "Left-handed metamaterials: The fishnet structure and its variations," *Phys. Rev. B* 75, pp. 235114 (9 pages), 2007.
[140] K. B. Alici and E. Ozbay, "A planar metamaterial: Polarization independent fishnet structure," *Photon. Nano. Fund. Appl.* 6, pp. 102-107, 2008.
[141] K. Aydin, Z. Li, L. Sahin L and E. Ozbay, "Negative phase advance in polarization independent, multi-layer negative-index metamaterials," *Opt. Express* 16, pp. 8835-8844, 2008.
[142] N. Shen, G. Kenanakis, M .Kafesaki, N. Katsarakis, E. N. Economou and C. M. Soukoulis, "Parametricinvestigation and analysis of fishnet metamaterials in the microwave regime," *J. Opt. Soc. Am. B* 26, pp. B61-B67, 2009.
[143] J. Valentine, S. Zhang, T. Zentgraf, E. U. Avila, D. A. Genov, G. Bartal and X. Zhang, "Three-dimensional optical metamaterial with a negative refractive index," *Nature* 455, pp. 376-379, 2008.
[144] C. García-Meca, R. Ortuño, Rodríguez-Fortuño F, J. Martí and A. Martínez, "Double-negative polarization-independent fishnet metamaterial in the visible spectrum," *Opt. Lett*. 34, pp. 1603-1605, 2009.
[145] A. A. Houck, J. B. Brock and I. L. Chuang, "Experimental observations of a left-handed material that obeys Snell's," law *Phys. Rev. Lett*. 90, pp. 137401 (4 pages), 2003.
[146] C. G. Parazzoli, R. B. Greegor, K. Li, B. E. C Koltenbah and M. Tanielian, " Experimental verification and simulation of negative index of refraction using Snell's law," *Phys. Rev. Lett*. 90, pp. 107401 (4 pages), 2003.
[147] M. Navarro-Cía, M. Beruete, M. Sorolla and I. Campillo, "Negative refraction in a prism made of stacked subwavelength hole arrays," *Opt. Express* 16, pp. 560-566, 2008.
[148] R. W. Ziolkowski and E. Heyman, "Wave propagation in media having negative permittivity and Permeability," *Phys. Rev. E* 64, pp. 056625 (15 pages), 2001.
[149] P. F. Loschialpo, D. L. Smith, D. W. Forester, F. J. Rachford and J. Schelleng, "Electromagnetic waves focused by a negative-index planar lens," *Phys. Rev. E* 67, pp. 025602 (4 pages), 2003.
[150] L. Fu, H. Schweizer, H. Guo, N. Liu and H. Giessen, "Synthesis of transmission line models for metamaterial slabs at optical frequencies," *Phys. Rev. B* 78, pp. 115110 (9 pages), 2008.
[151] K. B. Alici and E. Ozbay, "Characterization and tilted response of a fishnet metamaterial operating at 100GHz," *J. Phys. D: Appl. Phys.* 41, pp. 135011 (5 pages), 2008.

[152] M. Beruete, M. Navarro-Cía, M. Sorolla and I. Campillo, "Negative refraction through an extraordinary transmission left-handed metamaterial slab," *Phys. Rev B* 79, pp. 195107 (6 pages), 2009.
[153] M. Beruete, M. Navarro-Cía and M. Sorolla, "Strong lateral displacement in polarization anisotropic extraordinary transmission metamaterial," *New J. Phys.* 12, pp. 063037 (15 pages), 2010.
[154] L. Zhaofeng, K. Aydin and E. Ozbay, "Determination of the effective constitutive parameters of bianisotropic metamaterials from reflection and transmission coefficients," *Phys. Rev. E* 79, pp. 026610 (7 pages), 2009.
[155] D. R. Smith, D. C. Vier, T. Koschnyh and C. M. Soukoulis, "Electromagnetic parameter retrieval from inhomogeneous metamaterials," *Phys. Rev. E* 71, pp. 036617 (11 pages), 2005.
[156] K. Aydin, I. Bulu and E. Ozbay, "Verification of impedance matching at the surface of left-handed materials," *Microwave and Optical Technology Letters* 48, pp. 2548-2552, 2006.
[157] N. Katsarakis, T. Koschny, M .Kafesaki, E. Economou, E. Ozbay and C. M. Soukoulis, "Left- and right-handed transmission peaks near the magnetic resonance frequency in composite metamaterials," *Phys. Rev. B* 70, 201101 (4 pages), 2004.
[158] C. Menzel,T. Paul, C. Rockstuhl, T. Pertsch, S. Tretyakov and F. Lederer, "Validity of effective material parameters for optical fishnet metamaterials," *Phys. Rev. B* 81, pp. 035320 (5 pages), 2010.
[159] R. Marqués, L. Jelinek, F. Mesa and F. Medina, "Analytical theory of wave propagation through stacked fishnet metamaterials," *Opt. Express* 17, pp. 11582-11593, 2009.
[160] L. Jelinek, R. Marqués and J. Machac, "Fishnet Metamaterials - Rules for refraction and limits of homogenization," *Opt. Express* 18, pp. 17940-17949, 2010.
[161] A. Mary, S. G. Rodrigo, F. J. Garcia-Vidal and L. Martin-Moreno, "Theory of Negative-Refractive-Index Response of Double-Fishnet Structures," *Phys. Rev. Lett*. 101, 103902 (4 pages), 2008.
[162] J. B. Pendry, L. Martin-Moreno and F. J. García-Vidal, "Mimicking surface plasmons with structured surfaces," *Science* 305, pp. 847-848, 2004.
[163] B. A. Munk, *Frequency Selective Surfaces: Theory and Design*. The USA: John Wiley & Sons, Inc. 2000.
[164] T. W. Ebbesen, H. J. Lezec, H. F. Ghaemi, T. Thio and P. A. Wolff, "Extraordinary optical transmission through sub-wavelength hole arrays," *Nature* 391, pp. 667-669, 1998.
[165] M. Beruete, M. Sorolla, I. Campillo and J. S. Dolado, "Increase of the transmission in cut-off metallic hole arrays," *Microwave and Wireless Components Letters IEEE* 15, pp. 116-118, 2005.

[166] M. Beruete, M. Sorolla, I. Campillo, J. S. Dolado, L. Martín-Moreno, J. Bravo-Abad and F. J. García-Vida, "Enhanced millimeter-wave transmission through subwavelength hole arrays," *Opt. Lett*. 29, pp. 2500-2502, 2004.

[167] M. Beruete, M. Navarro-Cía, F. Falcone, I. Campillo and M. Sorolla, "Connection between extraordinary transmission and negative refraction in a prism of stacked sub-wavelength hole arrays," *J. Phys. D: Appl. Phys.* 42, pp. 165504 (4 pages) , 2009.

[168] C. García-Meca, R. Ortuño, F. J. Rodríguez-Fortuño, J. Martí and A. Martínez, "Negative refractive index metamaterials aided by extraordinary optical transmission," *Opt. Express* 17, pp. 6026-6031, 2009.

[169] M. Beruete, M. Sorolla, I. Campillo, J. S. Dolado, L. Martin-Moreno, J. Bravo-Abad and F. J. Garcia-Vidal, "Enhanced millimeter wave transmission through quasioptical subwavelength perforated plates," *Antennas and Propagation, IEEE Transactions on* 53, pp. 1897-1903, 2005.

[170] M. Beruete, M. Sorolla and I. Campillo, "Left-handed extraordinary optical transmission through photonic crystal subwavelength hole arrays," *Opt. Express* 14, pp. 5445-5455, 2006.

[171] M. Beruete, I. Campillo, M. Navarro-Cía, F. Falcone and M. S. Ayza, "Molding Left- or Right-Handed Metamaterials by Stacked Cutoff Metallic Hole Arrays," *Antennas and Propagation, IEEE Transactions on* 55, pp. 1514-1521, 2007.

[172] M. Beruete, M. Sorolla and I. Campillo, "Inhibiting Left-Handed Wave Propagation by a Band Gap of Stacked Cut-Off Metallic Hole Arrays," *Microwave and Wireless Components Letters, IEEE* 17, pp. 16-18, 2007.

[173] M. Beruete, M. Sorolla, M. Navarro-Cía, F. Falcone, I. Campillo and V. Lomakin, "Extraordinary transmission and left-handed propagation in miniaturized stacks of doubly periodic subwavelength hole arrays," *Opt. Express* 15, pp. 1107-1114, 2007.

[174] M. Beruete, M. Navarro-Cía, I. Campillo, F. Falcone, I. Arnedo and M. Sorolla, "Parametrical study of lefthanded or right-handed propagation by stacking hole arrays," *Opt. Quant Electron* 39, pp. 285-293, 2007.

[175] M. Beruete, M. Navarro-Cía and M. Sorolla Ayza, "Understanding Anomalous Extraordinary Transmission From Equivalent Circuit and Grounded Slab Concepts," *Microwave Theory and Techniques, IEEE Transactions on* 59, pp. 2180-2188, 2011.

[176] F. Medina, J. A. Ruiz-Cruz, F. Mesa, J. M. Rebollar, J. R. Montejo-Garai and R. Marque, "Experimentalverification of extraordinary transmission without surface plasmons," *Appl. Phys. Lett.* 95, pp. 071102 (3 pages), 2009.

[177] M. Beruete, M. Navarro-Cía, S. A. Kuznetsov and M. Sorolla, "Circuit approach to the minimal configuration of terahertz anomalous

extraordinary transmission," *Appl. Phys. Lett*. 98, pp. 014106 (3 pages), 2011.

[178] F. Medina, F. Mesa and R. Marqués, "Extraordinary Transmission Through Arrays of Electrically Small Holes From a Circuit Theory Perspective," *Microwave Theory and Techniques, IEEE Transactions on* 56, pp. 3108-3120, 2008.

[179] V. Delgado, R. Marqués and L. Jelinek, "Analytical theory of extraordinary optical transmission through realistic metallic screens," *Opt. Express* 18, pp. 6506-6515, 2010.

[180] R. Marquès , F. Mesa, L. Jelinek and F. Medina, "Analytical theory of extraordinary transmission through metallic diffraction screens perforated by small holes," *Opt. Express* 17, pp. 5571-5579, 2009.

[181] M. Navarro-Cia, M. Beruete and M. Sorolla, "Numerical and experimental parametric analysis of anomalous enhanced transmission through subwavelength apertures," *Metamaterials* 5, pp. 125-134, 2011.

[182] V. Lomakin and E. Michielssen, "Enhanced transmission through metallic plates perforated by arrays of subwavelength holes and sandwiched between dielectric slabs," *Phys. Rev. B* 71, pp. 235117 (10 pages), 2005.

[183] J. Zhou, Th Koschny, M. Kafesaki and C. M. Soukoulis, "Size dependence and convergence of the retrieval parameters of metamaterials," *Photonics Nanostruct.: Fundam. Appl.* 6, pp. 96-101, 2008.

[184] T. Koschny, P. Markoš, E. N. Economou, D. R. Smith, D. C. Vier and C. M. Soukoulis, "Impact of inherent periodic structure on effective medium description of left-handed and related metamaterials," Phys. Rev. B 71, 245105 (22 pages), 2005.

[185] J. Zhou, L. Zhang, G. Tuttle, Th. Koschny and C. M. Soukoulis, "Negative index materials using simple short wire pairs," *Phys. Rev. B* 73, 041101 (4 pages), 2006.

[186] R.A. Depine and A. Lakhtakia, "A new condition to identify isotropic dielectric-magnetic materials displaying negative phase velocity," *Microwave Opt Technol Lett* 41pp. 315-316, 2004.

[187] M. Navarro-Cia, M. Beruete, I. Campillo and M. Sorolla, "Millimeter-Wave Left-Handed ExtraordinaryTransmission Metamaterial Demultiplexer," *Antennas Wireless Propag. Lett., IEEE* 8, pp. 212-215, 2009.

[188] M Navarro-Cia, M. Beruete, F. J. Falcone, M. Sorolla Ayza and I. Campillo, "Polarization-tunablenegative or positive refraction in self-complementariness-based extraordinary transmission prism," *Progress In Electromagnetics Research* 103, pp. 101-114, 2010.

[189] M. Sanz, A. C. Papageorgopoulos,W. F. Egelhoff Jr, M. Nieto-Vesperinas and N. Garcia, "Transmission measurements in wedge-shaped absorbing

samples: An experiment for observing negative refraction," *Phys. Rev. E* 67, pp. 067601 (4 pages), 2003.

[190] B. A. Munk, *Metamaterials: Critique and Alternatives.* The USA: John Wiley & Sons, Inc. 2009.

[191] R. C. Hansen, "Negative refraction without negative index," *IEEE Trans. Antennas Propag*. 56, pp. 402-404, 2008.

[192] S. Enoch, G. Tayeb, P. Sabouroux, N. Guèrin and P. Vincent, "A Metamaterial for Directive Emission," *Phys. Rev. Lett.* 89, pp. 213902 (4 pages), 2002.

[193] M .Navarro-Cia, M. Beruete, F. Falcone, J. M. Illescas, I. Campillo and M. Sorolla Ayza, "Mastering the Propagation Through Stacked Perforated Plates: Subwavelength Holes vs. Propagating Holes," *Antennas and Propagation, IEEE Transactions on* 59, pp. 2980-2988, 2011.

[194] T. Gu, N. Petrone, J. F. McMillan, A. van der Zande, M. Yu, G. Q. Lo, D. L. Kwong, J. Hone, and C. W. Wong, "Regenerative oscillation and four-wave mixing in graphene optoelectronics," *Nature Photonics* 6, 554, 2012.

[195] Y. X. Yeng, M. Ghebrebrhan, P. Bermel, W. R. Chan, J. D. Joannopoulos, M. Soljacic, and I. Celanovic, "Enabling high-temperature nanophotonics for energy applications," *Proc. Nat. Acad. Sci. USA* 109, 2280, 2012.

[196] E. C. Nelson, N. L. Dias, K. P. Bassett, S. N. Dunham, V. Verma, M. Miyake, P. Wiltzius, J. A. Rogers, J. J. Coleman, X. Li, and P. V. Braun, "Epitaxial growth of three-dimensionally architectured optoelectronic devices," *Nature Materials* 10, 676–681, 2011.

[197] C. Garcia-Meca, J. Hurtado, J. Martí, A. Martínez, W. Dickson and A. V. Zayats, "Low-loss multilayered metamaterial exhibiting a negative index of visible of refraction at visible wavelengths," *Phys. Rev. Lett.* 106, 067402 (4 pages), 2011.

[198] J. Fischer, G. von Freymann, M. Wegener, "The materials challenge in diffraction-unlimited direct laser writing optical lithography," *Adv. Mater.* 22, 3578–3582, 2010.

[199] D. B. Burckel, J. R. Wendt, G. A. Ten Eyck, J. C. Ginn, A. R. Ellis, I. B., M. B. Sinclair, "Micrometer-scale cubic unit cell 3D metamaterial layers," *Adv. Mater.* 22, 5053–5057, 2010.

[200] L. Peng, H. Chen, H. Zhang, J. A. Kong, and T. M. Grzegorczyk, "Experimental observation of left-handed behavior in an array of standard dielectric resonators," *Phys. Rev. Lett.* 98, 157403 (4 pages), 2007.

[201] X. Cai, R. Zhu, and G. Hu, "Experimental study of metamaterials based on dielectric resonators and wire frame," *Metamaterials* 2, 220–226, 2008.

[202] Q. Zhao, L. Kang, B. Du, H. Zhao, Q. Xie, X. Huang, B. Li, J. Zhou, L. Li, "Experimental demonstration of isotropic negative permeability in a

three-dimensional dielectric composite," *Phys. Rev. Lett.* 101, 027402 (4 pages), 2008.
[203] M. S. Wheeler, J. S. Aitchison, M. Mojahedi, "Coated nonmagnetic spheres with a negative index of refraction at infrared frequencies," *Phys. Rev. B* 73, 045105 (7 pages), 2006.
[204] V. Yannopapas, "Negative refraction in random photonic alloys of polaritonic and plasmonic microspheres," *Phys. Rev. B* 75, 035112, 2007.
[205] S. Xiao, V. P. Drachev, A. V. Kildishev, X. Ni, U. K. Chettiar, H. K. Yuan, and V. M. Shalaev, "Loss-free and active optical negative-index metamaterials," *Nature* 466, 735–738, 2010.
[206] E. Plum, V. A. Fedotov, P. Kuo, ,D. P. Tsai, and N. I. Zheludev, "Towards the lasing spaser: Controlling metamaterial optical response with semiconductor quantum dots," *Opt. Express* 17, 8548–8551, 2009.
[207] C. M. Soukoulis, M. Wegener, "Past achievements and future challenges in the development of three-dimensional photonic metamaterials," Nature Photonics 5, 523–530, 2011.
[208] X. Liu, T. Starr, A. F.Starr, and W. J. Padilla, "Infrared spatial and frequency selective metamaterial with near-unity absorbance," *Phys. Rev. Lett.* 104, 207403 (4 pages), 2010.
[209] N. Liu, M. Mesch, T. Weiss, M. Hentschel, and H. Giessen, "Infrared perfect absorber and its application as plasmonic sensor," *Nano Lett.* 10, 2342–2348, 2010.
[210] R. B. Wehrspohn and J. Üpping, "3D photonic crystals for photon management in solar cells," J. Opt. 14 024003 (9 pages), 2012.

Appendix

Publications in SCI Journals

[1] Z. Li, H. Caglayan, E. Colak and E. Ozbay, "Enhanced transmission and directivity from metallic subwavelength apertures with nonuniform and nonperiodic grooves," Appl. Phys. Lett., Vol: 92, pp. 011128 (3 pages), 2008.

[2] H. Kurt, E. Colak, A. O. Cakmak, H. Caglayan and E. Ozbay, "The focusing effect of graded index photonic crystals," Appl. Phys. Lett., Vol: 93, pp. 171108 (3 pages), 2008.

[3] E. Colak, H. Caglayan, A. O. Cakmak, A. D. Villa, F. Capolino and E. Ozbay, "Frequency dependent steering with Backward Leaky Waves Via Photonic Crystal Interface Layer," *Opt. Express*, Vol: 17, No: 12, pp: 9879-9890, 2009.

[4] A. O. Cakmak, E. Colak, H. Caglayan, H. Kurt and E. Ozbay, "High efficiency of graded index photonic crystal as an input coupler," J. Appl. Phys., Vol: 105, pp. 103708 (5 pages), 2009.

[5] A. O. Cakmak, K. Aydin, E. Colak, Z. Li, F. Bilotti, L. Vegni and E. Ozbay, "Enhanced transmission through a subwavelength aperture using metamaterials," Appl. Phys. Lett, Vol: 95, pp: 52103-52103, 2009.

[6] D. Ates, A. O. Cakmak, E. Colak, R. Zhao, C. M. Soukoulis and E. Ozbay, "Transmission Enhancement Through Deep Subwavelength Apertures Using Connected Split Ring Resonators," *Opt. Express*, Vol: 18, No: 4, pp: 3952-3966, 2010.

[7] Z. Li, H. Caglayan, E. Colak, J. Zhou, C. M. Soukoulis and E. Ozbay, "Coupling effect between two adjacent chiral structure layers," Opt. Express, Vol: 18, No: 6, pp: 5375-5383, 2010.

[8] Z. Li, R. Zhao, Th. Koschny, M. Kafesaki, K. B. Alici, E. Colak, H. Caglayan, E. Ozbay and C. M. Soukoulis, "Chiral metamaterials with negative refractive index based on four "U" split ring resonators," Appl. Phys. Lett., Vol: 97, No: 8, pp. 081901 (3 pages), 2010.

[9] E. Colak, A. O. Cakmak, A. E. Serebryannikov and E. Ozbay, "Spatial filtering using dielectric photonic crystals at beam-type excitation," J. Appl. Phys., Vol: 108, No: 11, pp. 113106 (8 pages), 2010.

[10] A. O. Cakmak, E. Colak, A. E. Serebryannikov and E. Ozbay, "Unidirectional transmission in photonic-crystal gratings at beam-type illumination," *Opt. Express*,, Vol: 18, No: 21, pp: 22283-22298, 2010.

[11] Z. Li, K. B. Alici, E. Colak and E. Ozbay, "Complementary chiral metamaterials with giant optical activity and negative refractive index," Appl. Phys. Lett., Vol: 98, No: 16, pp. 161907 (3 pages), 2011.

[12] E. Colak, A. O. Cakmak, Koray Aydin and E. Ozbay, "Observation of negative refraction with fishnet structure: Wedge Experiments," Submitted in 2012, under review.

[13] A. O. Cakmak, E. Colak and E. Ozbay, "Simultaneously opening transmission channels with left- and right-handed behavior for the stacked subwavelength apertures in fishnet metamaterials with hybrid unit lattices ," Submitted in 2012, under review.

Copyright and Permissions

Section 2.2

Part of the section 2.2 is published as

H. Kurt, E. Colak, O. Cakmak, H. Caglayan and E. Ozbay, "The focusing effect of graded index photonic crystals," *Appl. Phys. Lett*. 93, pp. 171108 (3 pages), 2008.

Section 2.2 is reproduced from the publication above with permission whose related copyright documents are attached at the end of the thesis.

Section 2.3

Part of the section 2.3 is published as

A. O. Cakmak, E. Colak, H. Caglayan, H. Kurt and E. Ozbay, "High efficiency of graded index photonic crystal as an input coupler," J. Appl. Phys., Vol: 105, pp. 103708 (5 pages), 2009.

Section 2.3 is reproduced from the publication above with permission whose related copyright documents are attached at the end of the thesis.

Section 2.4

Part of the section 2.4 is published as

E. Colak, A. O. Cakmak, A. E. Serebryannikov and E. Ozbay, “Spatial filtering using dielectric photonic crystals at beam-type excitation,” J. Appl. Phys., Vol: 108, No: 11, pp. 113106 (8 pages), 2010.

Section 2.4 is reproduced from the publication above with permission whose related copyright documents are attached at the end of the thesis.

Section 2.5

Part of the section 2.4 is published as

E. Colak, H. Caglayan, A. O. Cakmak, A. D. Villa, F. Capolino and E. Ozbay, "Frequency dependent steering with Backward Leaky Waves Via Photonic Crystal Interface Layer," *Opt. Express*, Vol: 17, No: 12, pp: 9879-9890, 2009.